Low-profile, Ultra-wideband, Cavity-backed Spiral Antennas

A dissertation
submitted by

Nahid Rahman

in partial fulfillment of the requirements
for the degree of

Doctor of Philosophy
in
Electrical Engineering

TUFTS UNIVERSITY

May 2012

Certified by . . . .
Mohammed N Afsar
Professor, Thesis Supervisor

Accepted by . . . .
Joseph Noonan
Professor, Committee Member

Accepted by . . . .
Sameer Sonkusale
Professor, Committee Member

Accepted by . . . .
Robert J Mailloux
Professor, Committee Member

Accepted by . . . .
Jeffrey Hopwood
Chairman, Department Committee on Graduate Students

Abstract

Spiral antennas are a popular class of antennas that demonstrate exceptionally large bandwidths, uniform input impedance, stable gains and the ability to radiate circularly polarized waves over their entire frequency coverage. Circularly polarized radiators are integral components of all space-based communication, SATNAV and SATCOM services, microwave direction finding systems, GPS applications, in-flight connectivity etc. As a result, spiral and helical elements have become a distinctive branch in the field of antenna engineering.

Spiral antennas are often configured with a metallic cavity that restricts the radiation to one hemisphere for unidirectional operation. With ever-decreasing dimensions of communication devices and to focus on issues concerning space constraints arising from installation of numerous antenna elements, low-profile geometries have drawn considerable research interest over the years. In this dissertation, we have addressed the problem of designing low-profile, ultra-wideband (UWB), 2-18 GHz cavity-backed spiral antennas.

First, we discuss the development of UWB shallow, absorptive cavities from a microwave material characterization standpoint. We then proceed onto geometrically modifying regular spirals to obtain more compact structures that incorporate certain radiation properties. Axial ratio is one the most important bandwidth factors in measuring the performance of a circularly polarized radiator. In developing low-profile geometries, one most often encounters the problem of deterioration of the axial ratio. This is particularly evident in rectangular spiral antennas, where the purity of the circularly polarized waves is highly compromised as a tradeoff with available aperture. It therefore becomes essential to design spiral geometry in such a way so as to preserve the lowest possible antenna aperture with the best possible axial ratio performance.

In our work, we have presented a detailed study of slow wave spirals, elliptical spirals and modified Archimedean polygonal spiral antenna designs that address the problem of maintaining high axial ratio performance with low-profile planar geometries. The designed antenna systems have been fabricated and tested for performance validation, and they demonstrate excellent axial ratio characteristics across their bandwidth.

Acknowledgments

All praise belongs to God Almighty for His assistance in every aspect of life. I am extremely thankful for all the avenues He has created for me to learn new things and develop as a human being while working on this dissertation.

First and foremost, I would like to thank by beloved parents Mustafizur Rahman and Nurun Nahar Rahman, without whose continued love and support, I would not be able to complete this work. Special thanks to my sister Nushrat Rahman for having so much love and patience for me througout the years. Special thanks to Aunt Eti, Muhib, Zahed Bhaia, Niki, Zahin, Ahsan, Surayia and everyone else in my family for being so wonderfully supportive.

I am extremely grateful to my advisor Mohammed N Afsar for his brilliant guidance, advice, encouragement, ideas and intuitions essential to my PhD research and having unwavering faith in me. I am also very grateful to my committee members and mentors: Joseph Noonan, Sameer Sonkusale and Robert Mailloux. Special thanks to our department Chair Jeffrey Hopwood for his wonderful assistance with the antenna fabrications.

There are no words to express my appreciation for Kathryn Geismar and Nandini Talwar for their constant support throughout my time at Tufts.

I would like to thank the Microwave Engineering Corporation for supporting this work and performing antenna measurements. Thanks to C.J. Reddy at EMSS, USA for software assistance. Thanks to ARC Technologies and Emerson & Cumming Microwave Products for sample absorbing materials. Thanks to E-FAB for precisely machining the antenna components.

Special thanks to the Academic Resource Center and the Office of Technology Licensing at Tufts for your wonderful assistance.

Finally, I have no words for each and every one of my dearest beloved friends who have been the most blessed and the best gifts in my life. Thank you so much for being there always.

Contents

List of Figures

List of Tables

Chapter 1

Introduction

The spiral shape, with its surprising occurrences from the tiniest DNA strands to the sprawling galaxies, has captivated mathematicians, physicists, astronomers, biologists, architects, philosophers, artists and engineers alike. Found in a host of instances where nature has employed spirals in the design of the universe; i.e. magnetic fields, our fingerprints, galaxies, ocean currents, tornadoes, ram-horns, sea-shells, the face of a sunflower, spider webs, ferns, microscopic algae to name only a few, the simple, attractive, yet mysterious pattern has left a deep impact on human consciousness and touched every aspect of our culture. Antenna system designers are no exception and have developed a flourishing technical area investigating the fascinating properties of spiral and helical antenna elements. The pattern has its distinctive signature in the field of antenna engineering due to its unique collection of electrical properties that is rarely observed in other geometries.

Spirals are one of the most useful and popular class of antennas that exhibit exceptionally large bandwidths, can be easily be spatially deployed and has the ability to maintain near-circular polarization, consistent gain and input impedance over their ultra-wide bandwidths [21].

1.1 General Features

1.1.1 Wide Bandwidth

Spiral antennas are often theoretically classified as frequency-independent antennas. This is because these antennas are entirely specified by their angles as opposed their physical lengths, which forms the basis for their frequency-independent nature (in practice, ultra-wide bandwidths).

The antenna is continuously self-scaling or frequency self-selecting, as it radiates from a region where the length of the arm is approximately equal to one or any integer multiples of the wavelength. Hence, as long as the antenna arms are long enough to support propagation of the travelling wave for at least one wavelength, the operational frequency still remains within the frequency capability of the antenna.

Here, we should note that in order to be truly frequency independent, the spiral arms should be of infinite length. But in practice, the antenna has to be truncated according to realizability constraints. Therefore, it is not a truly self-scaling antenna since the spiral cannot be truncated without affecting the pattern response. However, very large bandwidths can still be realized by loading the ends of the spirals that prevent reflections from their ends [24]. The bandwidth of spiral antennas is hence determined by the fine precision of the feeding region (high frequencies) and overall spiral aperture size (low frequencies) [10].

1.1.2 Circular Polarization

The geometry of the structure and the relationship of the spiral dipoles give rise to a 90° phase shift of the E vector with time. This yields a circular polarization response characteristic. For every differential group of elements that have shifted 180° in phase at the diameter of radiation, there is another group that is in time and space quadrature since the phase of the groups is varying as a function of the spiral growth rate. The result is a 90° phase shift causing the spiral antenna to radiate circularly polarized waves [46].

Antenna polarization is an important consideration when selecting and installing antennas. In a circularly polarized antenna, the plane of polarization rotates in a corkscrew pattern making one complete revolution during each wavelength. As the signal leaves the antenna, it is spinning, and not maintaining a set angle. Such a wave radiates energy in the horizontal plane, vertical plane, and in every plane in-between as well encompassing every angle. The sinal arrives with uniform intensity at the receiver regardless of how the receiving antenna is polarized. Since the signal is sent and received in all planes, whenever it is reflected off of a surface, signal strength is not lost, but is transferred to a different plane and still utilized.

A fundamental advantage of circular polarization is that all reflections change the direction of polarization or rotation of the wave, preventing the usual addition or subtraction of main and reflected signals. Therefore there is far less fading and flutter when circular polarization is used at either or both ends of a link. These antennas are highly effective for reliable correspondence with vertical and horizontally polarized stations and reducing signal fade when communicating with distant terminals, regardless of the bearing of the aircraft or satellites that use them [13].

High-frequency systems (i.e. 2.4 GHz and higher) that use linear polarization typically require a clear line-of-sight path between the two points in order to operate effectively. Such systems have difficulty penetrating obstructions due to reflected signals. This is because the reflected linear signals return to the propagating antenna in the opposite phase, and weakens the propagating signal. In contrast, since in circularly-polarized systems, the reflected signal is returned in the opposite orientation, conflict with the propagating signal is largely avoided. The result is that circularly-polarized signals are more efficient at penetrating and bending around obstructions. These waves are far more resistant to signal degradation due to inclement weather conditions as well [13].

1.1.3 Uniform Input Impedance

Spiral antenna arms are usually constructed as pairs of metallic radiators or pairs of slots that are self-complementary, that is, the width of the spiral arms are equal to the spacing between them. According to Babinet's optical principle, if light were diffracted by a screen resulting in light patterns that are complement of the screen pattern, then the sum of the screen and the complement would be the pattern without the screen. In antenna theory, if a radiating conductor is the complement of a conducting sheet that has a slot removed which is exactly equal to the shape of the conductor, the antenna structure is considered self-complementary [46]. In other words, the self-complementary structure is a structure that is complementary to the original structure itself [26].

It has been shown using Booker's principle (which is an extension of Babinet's principle which includes the polarization of the field) that for complementary structures, if a screen and its complement (the metallic arm and air in the case of spirals) are immersed in a medium with intrinsic impedance η and have terminal impedances of Z_s and Z_c respectively, then if the magnetic field present in the conductor is compared with the electric field in the slot and if line integrals are performed for each to determine the impedance, the impedance relation for a two-arm structure is given by 1.1 [6].

$$Z_c Z_s = \frac{\eta_0^2}{4} \tag{1.1}$$

where, η_0 is the impedance of free space, with $\eta_0 = 377\Omega$. Now, for planar spirals, an exchange of spaces and conductors leaves the structure unchanged except for rotation. Then for the self-complementary case, the input impedance of the planar spiral is given by 1.2.

$$\begin{aligned} &Z_c = Z_s = Z_{spiral} \\ &\Longrightarrow \; Z_{spiral} = \sqrt{\frac{\eta_0^2}{4}} = \frac{\eta_0}{2} \simeq 188\Omega \end{aligned} \tag{1.2}$$

The above impedance equation is frequency-independent and demonstrates the constant-impedance characteristic of self-complementary planar spirals even when they are operating at broadband frequencies. This property is yet the most attractive feature of spiral antennas. This is because all practical antennas are connected to transmission lines as transducers of the electric power between the electric circuits and the propagated electromagnetic waves. For ultra-wideband radiators, ultra-wideband matching networks are required for efficient radiation. Spiral antennas, due to their unique constant impedance property, resolve the issue of impedance matching to transmission lines at extremely broad frequencies while at the same time efficiently radiating high quality circularly polarized waves across their entire bandwidth of operation.

1.2 Spiral Antenna Applications

An increasing demand for available radio spectrum, space constraints arising from a lack of suitable installation platforms for too many antennas, the need for improvement in radar resolution and the demand for data rate communication systems have prompted the development of wideband antennas which operate at microwave frequencies. A wide range of commercial, military and private applications exist for spiral antennas, especially where bandwidths of as much as 100:1 are desired: consolidation of multiple low-gain communication antennas on moving vehicles, military surveillance and microwave direction finding, ECM (electronic countermeasures), ECCM (electronic counter-counter measures) to name a few [46].

The WAAS (Wide Area Augmentation System), a precision approach that enables aircrafts to depend on GPS (Global Positioning Systems) for all phases of flight, uses circularly polarized L band and S band antennas. For GPS systems, spiral antennas are very commonly used because of their ability to produce a very wideband (covering L band and S band), and an almost perfect circularly polarized radiation over their full operational bandwidth.

With the recent development of commercial satellites, it is often desirable to communicate directly between an aircraft regardless of its bearing and a tracking satellite located above the flight path of the aircraft. All space-based communication has employed the use of circularly polarized waves to ensure successful links with spacecrafts and orbiting satellites at all points in time.

1.3 Cavity-Backed Spiral Antennas

The spiral antenna has front-to-back symmetry and has two broad lobes whose directions are perpendicular to the plane of the antenna [46]. In most cases, a unidirectional pattern is preferred in order to detect reflections from or transmit towards one direction only and to minimize the influence of either the measurement system [45] or the interference arising from an aircraft or a satellite structure. Therefore, often a metallic cavity is added to absorb the backlobe completely. However, the downside of this arrangement is that only half the input power is transformed into radiated power. The following configurations of cavities are used in general:

1. A cavity with no absorbing materials. This works well for narrowband applications. For proper operation, the cavity depth is equal to odd multiples of $\left(\frac{\lambda}{4}\right)$ so that the back-lobe is absorbed by destructive interference. Here, λ is the wavelength corresponding to the center frequency of operation. This configuration can also enhance the co-pole or vertical intended polarization in the spiral plane.

2. For ultrawideband (UWB) applications, anechoic absorbing materials is used in a backing cavity to absorb the back-lobe.

3. An absorbing cavity restricts the radiation to one hemisphere at the expense of a 3dB reduction in the antenna gain. One possibility to counteract this problem is to use electromagnetic band-gap (EBG) materials in the cavity. This technology, however, is still relatively bandwidth limited and has not yet been able efficiently address the needs of microwave applications where bandwidths of more than 10:1 are required.

1.4 Design of Low-Profile Geometries

1.4.1 Shallow Absorptive Cavities

When a spiral antenna is operating at UWB frequencies, its cavity needs to be configured with microwave materials that can effectively absorb the EM energy over a broad spectrum of frequencies. Designing an appropriate broadband absorbing material poses a challenge when the frequency-dependent complex permittivity and permeability of a material comes into play. Most single-layer, homogeneous linear absorbing materials are effective only at narrowband frequencies; in this case the best possible solution in order to obtain a broadband response is to stack multiple absorbing layers into a composite structure and tune the thickness of each layer so that an overall broadband response is obtained [43].

To obtain the maximum bandwidth using multi-layer absorbing strutures, usually computer simulation or universal design charts are used, where the complex permittivity and complex permeability of the constituent materials theoretically satisfy the Kramers-Kronig relationship [43, 47, 25]. However, the problem with this approach is that materials with theoretically-computed permittivity and permeability values may not exist in practice or may be deemed non-manufacturable due to physical constraints. A realistic approach is to use precision measurement techniques to characterize the electromagnetic properties of existing narrowband materials from a broad coverage of frequencies, and then to select appropriate components so as to realize absorbers of intended bandwidth [43].

Once a suitable combination of materials for the antenna cavity has been selected and a composite structure designed, optimization algorithms can then be used to determine the optimum cavity dimensions which give the best radiation performance. But even though there are numerous high performance commercial EM software currently available for simulation, designing optimized geometry using experimentally-obtained material characterization data still remains contingent upon the availability of precise and sophisticated microwave measurement instrumentation. In our work, we have addressed the general problem of the design and optimization of low-profile, wideband systems from a microwave material characterization standpoint. We have first outlined the procedure for accurately designing and optimizing the dimensions of any broadband, cavity-backed spiral antenna. A precision microwave measurement technique was used to address the needs of lightweight and broadband absorptive cavities. We have then proceeded to geometrically modify simple spirals to obtain more compact antennas or to incorporate desired radiation characteristics in the cavity-backed elements.

1.4.2 Preserving the Purity of Circular Polarization

In developing low-profile geometries for spiral antennas, one often encounters the problem of deterioration of the axial ratio. This is particularly evident in rectangular spirals where the purity of the circularly polarized waves is higly compromised as a tradeoff with available antenna aperture. It therefore becomes essential to design spiral geometry in such a way so that the lowest possible antenna aperture provides the best axial ratio performance possible. In this work, we present a detailed study of slow wave spirals and novel polygonal spiral antenna designs that address the problem of maintaining high axial ratio performance.

1.5 Previous Work

When a spiral antenna is backed with an absorbing cavity, theres is a 3dB reduction in the antenna gain. To address the matter, $\left(\frac{\lambda}{4}\right)$ reflecting cavities, cavities with special materials and parabolic reflectors are currently under investigation. Recent developments on 10-14 GHz EBG ground plane backed Archimedean spirals, 6-12 GHz meta-material inspired spirals, 3-10 GHz disk attached shallow cavities, and 0.36-6.83 GHz spirals with parabolic reflectors have demonstrated reasonably low-profile geometries [7, 27, 29, 17]. Most efforts, however, are relatively bandwidth limited and have not been able to address the needs of applications where bandwidths $\geq 10:1$ are required with good circular polarization performance. Absorptive cavity-backed spiral radiators provide an effective solution for multiple SATCOM and SatNav services requiring consistent gain, uniformly-matched input impedances and $\leq$ 3dB axial ratios across an extremely wide range of frequencies.

2-18 GHz spiral antennas operating at UWB frequencies are difficult to reduce to profiles lower than 1 inch in thick-ness [20, 16]. This is due to the fact that the materials used in the cavities are predominantly dielectric in nature ($\simeq 1$), and are relatively thicker than their magnetic counterparts. Magnetic absorbers on the other hand, attenuate EM waves through magnetic hysteresis loss and can be designed to be very thin microwave absorbers. Also, these materials can be produced as non-conductive absorbents since they are most often constructed from ferrites, and can be effectively used without creating a short circuit in the metallic cavity. Hence, magnetic materials offer an attractive choice for the design of shallow cavities. However, ferrite-based absorbers work best at frequencies below 2 GHz. Their resonant properties tend to roll off after that. And to create dielectric loss at a lower frequency requires adding more metallic materials in the absorbent, which may create problems such as increased surface impedance in real time applications.

Keeping these factors in mind, we proceeded to develop an effective way to construct low profile cavities by using a hybrid composite of magnetic and dielectric absorbing materials arranged in an appropriate order and optimized for maximum radiation performance. The magnetic materials are tailored to provide absorption at frequencies in the vicinity of 1-2 GHz significantly reduce the cavity depth. The dielectric absorbers on the other hand are suitable for higher frequencies and allow for a gradual impedance taper in a multi-layer cavity arrangement.

Successful design, optimization and performance verification of UWB antennas having frequency-dependent electromagnetic materials inserted into their cavities, however, can only be possible if the complete frequency response of each of these materials are available with significant accuracy. Even though many wideband microwave measurement techniques have been developed for precision characterization of linear, dielectric materials, traditional methods often pose a challenge for magnetic materials, materials having both dielectric and magnetic characteristics, or non-reciprocal resonant materials such as meta-materialized structures. Developing low-profile, absorptive, cavity-backed spiral antennas becomes contingent upon the availability of appropriate material characterization instrumentation and methodology that is capable of producing precise complex permittivity and permeability data, so that these material properties can be accurately replicated in simulation tools to ensure the closest antenna pattern approximations prior to fabrication.

In most microwave measurement techniques reported to date, sample preparation can be tedious whenever a free space method or resonant cavity based technique is used. Only a waveguide based method provides the most accurate broadband response and it's relatively simple to prepare a specimen under test to be fitted to a waveguide. One of the most conventional techniques in measuring the complex permittivity and permeability of materials is the transmission and reflection (T/R) method proposed by Nicolson-Ross and Weir [32, 48]. This technique has been in practice for over forty years to successfully characterize regular well-behaved, linear materials. The method, using a Vector Network Analyzer, incorporates the S-parameters measured inside a waveguide, and uses two out of four S parameters for permittivity and permeability calculations. The method posed major challenges, such as significantly deviating measurements at the start and stop frequencies of each waveguide band. To overcome the challenges in this T/R technique, Baker-Jarvis [5] proposed a numerical iteration method to remove the divergences in the waveguide measurements. Their modification required appropriate initial guess parameters and all four S-parameters were needed in the calculations. Further improvements on the stability of this technique have been made by scientists over the years [3]. But all the improvements suggested either a need for an initial guess parameter or appropriate integer values for the phases, since the phases were multi-valued in the phase wrapping procedure. As a result, these improvements left the technique open to errors in real time measurements. In order to develop low-profile, hybrid absorbing cavities for spiral antennas, we have used accurate simultaneous equations for permittivity and permeability determination from T/R measurements. Our precision measurement techniques allows us to effectively design absorbing cavities and optimize antenna geometry for maximum performance.

For the optimization of antenna geometry which incorporates absorbing or other special materials, it is necessary that the frequency-dependent permittivity and permeability behavior is accurately replicated in the EM simulation software. It is possible to optimize an antenna geometry at discrete frequency points or narrowband frequencies for desired radiation performance using highly efficient optimization algorithms. However, for broad spectrum optimization of antennas that use microwave materials in their structure, since one of the variable parameters along with physical antenna dimensions is frequency, the material properties need to be appropriately updated during the course of the simulation due to their variable frequency-dependent values. This can only be possible if the material properties such as permittivity, permeability, dielectric and magnetic loss tangent are described in terms of equations which relate these properties to frequency in the EM solver and then the optimization algorithms are used for broad-spectrum performance. In this way, when the optimization goal is to achieve optimal antenna dimensions which give the best radiation performance over a broad spectrum, as the simulator iterates over the algorithm by varying the antenna dimensions and also the frequencies within the given spectrum, the correct material values associated with the run-time frequency of concern are used in the optimization procedure.

An important issue we have addressed in this work is the high axial ratios generally demonstrated by cavity-backed spiral antennas with a rectangular footprint. Although square spirals allow for compact packaging, they often demonstrate irregular performance across the band and commonly have poor axial ratio performance compared to their circular Archimedean counterparts. In recent work, modified logarithmic and modified hybrid rectangular geometries have been proposed to improve the performance of conventional square Archimedean spirals [41]. These approaches, however, have shown to have axial ratios ≥ 4 dB over a significant portion of their operational bandwidths. In other work, the use of high-contrast dielectric materials in slot spirals have shown to improve the axial ratio to some extent at UHF frequencies

(0.5-2 GHz) [19]. However, the deterioration of axial ratios for square spirals operating at UWB frequencies, i.e. 2-18 GHz is yet to be effectively addressed. In this study, we have presented 2-18 GHz polygonal modified Archimedean spiral antennas that maintain $\leq 3dB$ axial ratio from 93.75%-98% of their operational bandwidths. Our work is a novel approach to counteract the axial ratio deterioration in square spiral antennas.

1.6 Organization of Thesis

Chapter 2 summarizes some theoretical background on spiral antennas. Here, we have attempted to shed light on the principles of spiral radiation, antenna parameters analyzed in our studies and the method of analysis we have used.

Chapter 3 describes the theoretical concepts behind the characterization, design and optimization of shallow, absorptive cavity-backed spiral antennas. We first introduce a precision transmission-reflection (T/R) based automated waveguide measurement technique for microwave frequencies. Using this technique, a set of commercially available absorbers in the broad frequency range from 2 to 40 GHz were accurately characterized. From the complex permittivity and complex permeability thus measured, we have analyzed their characteristic impedance and specular reflection properties to design 2-18 GHz lightweight multi-layer composite absorber. In EM simulation software FEKO, we modeled a two-arm, 2-18 GHz, Archimedean spiral antenna with the multi-layer absorber inserted in the cavity. The frequency dependent permittivity and permeability equations obtained from our measurements have been used to accurately replicate the behavior of the absorbing layers in the cavity. We then show that with an EM simulation software with an optimizer feature available, it is possible to determine the optimal thickness of the cavity such that the absorption properties are sufficiently maintained, and radiation performance is maximized over the entire bandwidth of any cavity-backed spiral antenna in general.

In chapter 4, we have designed, optimized and analyzed a cavity-backed modified Archimedean spiral antenna using a zigzag shape to increase the length of the spiral arms to be packaged in a compact form. The reduced-size spiral slows the wave on the spiral arms and improves low-frequency performance of the antenna. Here we have focused on the structural modification of the antenna, as well as developing an optimized cavity backing with accurately characterized absorbing materials that enhances the antenna performance. The radiation performance of the zigzag Archimedean spiral antenna is presented and analyzed in this chapter.

In chapter 5, we have investigated the beam-width control properties of cavity-backed, elliptical spiral antennas. We varied the ratio of the major axis to the minor axis of a simple circular spiral to create an elliptical structure and observed changes in the radiation pattern. By using an elliptical spiral antenna, we have been able to regulate the beam-width in two orthogonal planes, $\theta = 0^\circ$ and $\theta = 90^\circ$. Using an elliptical structure compromises the purity of circular polarization to some extent in the lower frequencies. However, the ability to control the beam-width in orthogonal planes can be useful in many ways. Focusing the beam-width in certain directions distributes more power to those directions and allows for efficient power distribution depending on desired areas or angles of coverage. Furthermore, the beam-width is one of the most important factors to decide the degree of interference to the signal received during a solar outrage. Narrower beam-widths with high directivity offer higher signal-to-noise ratios and minimize signal outage during solar outrage. This chapter discusses beam-width control properties and key antenna performance parameters of a single elliptical cavity-backed Archimedean spiral antenna.

In chapter 5, we also investigate cavity-backed square spirals that can allow for closer packaging in array environment and, due to their longer circumference than round spirals, are able to provide some inherent miniaturization factor for improved low-frequency operation. We have studied their axial ratio properties and tried to improve upon axial ratio performance by making geometrical changes. However, our results show that purely square spiral antennas, while having comparable gain performance with their circular counterparts, commonly suffer from high axial ratios well above 4 dB across their bandwidths.

The primary advantage of using spiral antenna systems is the radiation of circularly polarized waves over ultra-wide bandwidths. Although square spirals allow for compact packaging, they often demonstrate irregular performance across the band and commonly have poor axial ratio performance compared to their circular Archimedean counterparts. In chapter 6, we present a novel 2-18 GHz polygonal modified Archimedean spiral antenna that approximates a circular Archimedean spiral in its high frequency operating region and a square spiral in its low-frequency zone. The polygonal antenna is backed with a shallow, hybrid, absorptive cavity described in chapter 3. The design has maintained $\leq$ 3 dB axial ratio for 93.75%-98% of its bandwidth while preserving the advantages of a square spiral antenna. 3 modifications to the original polygonal antenna are also presented here. The radiation patterns obtained from the proposed polygonal geometries are compared to that obtained from purely circular and square patterns having the same diameter and the significant improvement in axial ratio is demonstrated in the results.

Chapter 7 concludes the dissertation with discussions on scope for further improvement and future research goals towards which the work can be extended.

Chapter 2

Theoretical Principles

In this dissertation, we have designed and investigated the radiation properties of cavity-backed 2-18 GHz spiral antennas of different configurations. Before proceeding onto the next chapters, it may be useful to provide some insights into the nature of wave polarization, the theoretical principles associated with spiral antenna radiation, the antenna parameters of interest and the method of analysis used in this work.

2.1 Circularly Polarized Waves

Electromagnetic waves are primarily charaterized by the frequency of oscillation, the direction of propagation, the strength (or intensity) and the polarization of the wave. Polarization is the description of the motion of the tip of the instantaneous electric field vector varying with time at a fixed point in space [44]. Electromagnetic waves can be randomly polarized (solar emissions), completely polarized, or partially polarized (containing both randomly polarized components and a completely polarized component). The polarization of an antenna is the polarization of the wave radiated by the antenna in the transmission mode [44].

When electromagnetic waves are propagating in free space or where no materials are in the vicinity of the propagation path, the waves are transverse, where the electric and magnetic fields are perpendicular to the direction of propagation. In this case the wave motion is determined by the form of the source [44]. At long distances from the source, the phase-front or surface of constant phase becomes so large that over small regions, the phase front is approximately planar and is referred to as a plane wave. A commonly used practice in antenna engineering is to use the far-field distance associated with an antenna diameter D and wavelength λ as 2.1.

$$Far field\ distance\ d = \frac{2D^2}{\lambda} \tag{2.1}$$

At a far-field distance away from the antenna, the wave from a transmitter is considered a plane wave and plane wave mathematics, which follow directly from the solution to Maxwell's equations, can be applied in the analysis of antenna radiation characteristics [44].

Plane waves are polarized. The polarization of a wave is determined from the motion of a fixed vector with time in a fixed plane (the stationary plane of obeservation). The wave passes through this plane in a direction perpendicular to it as shown in Figure 2-1. In general, the electric field vector in the plane of polarization at every instant of time can be described by two orthogonal linear polarizations. The relative amplitude and phases of these components determine the polarization of the wave. If the two components are in phase, the wave is linearly polarized. However, when the two orthogonal linear polarization components are out of phase, the resultant locus of points of the electric field vector tip is an ellipse, and the wave is said to be elliptically polarized. If the two orthogonal linearly polarized components are equal in magnitude, but in phase-quadrature(one component leads/lags the other by $\delta = 90°$), or in other words, the electric field vector crosses the x-axis a quarter cycle before(or after) it crosses the y axis, then the wave is a circularly polarized wave. Therefore, a wave can be circularly polarized when three conditions are met on the linear orthogonal components: spatial othogonality, time quadrature and equal amplitude. The polarization plane and the wave propagation is shown in Figure 2-1 [44].

Specification of polarization includes the sense of rotation as well. The IEEE convention is that when viewing the polarization plane with the wave direction ap-

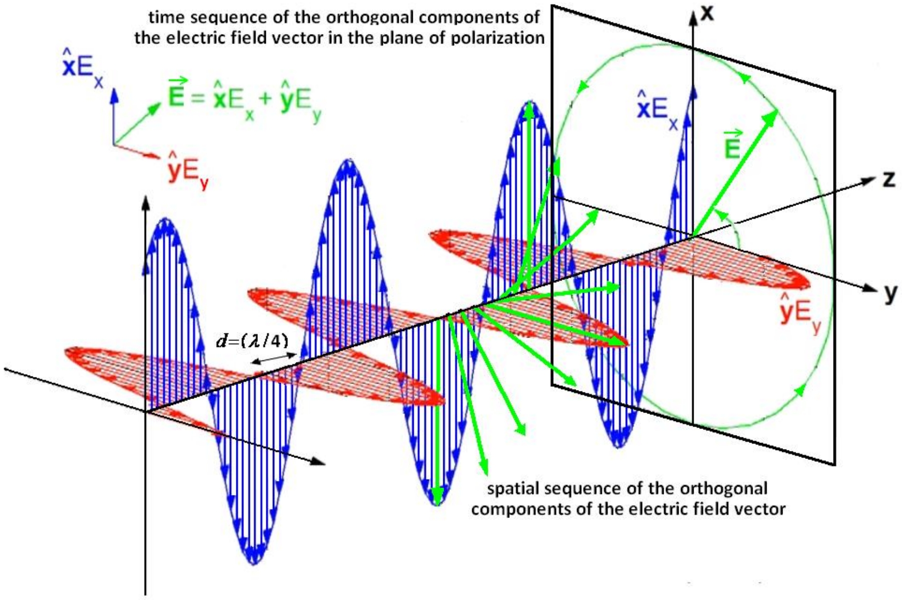

Figure 2-1: The polarization plane and propagation of a left-hand circularly polarized wave

proaching the oberver, if the thumb of the right hand is pointed in the direction of propagation, and the fingers curl in the direction of rotation of the electric field around the polarization ellipse in a counterclockwise manner, the sense is right hand. Similarly, a wave is left hand sensed if the thumb of the left hand is pointed in the direction of propagation and the fingers curl clockwise when the wave approaches the observer [44].

An efficient way to realize wideband, circularly polarized radiation is to use a spiral or helical antenna system. In the following chapters, design and optimization of low-profile spiral antenna cavities and novel spiral antenna structures are discussed. The basic theoretical priciples of spiral operation are included here.

2.2 Theory of Spiral Operation

The performance of a spiral antenna is best understood from the distribution of current produced by applying a source of radio frequency power to its terminals. Although powerful computer methods are available and have been used to find the current distributions on spiral antennas with spiral arms, the computed results serve primarily to reinforce intuitive concepts and measurements that were used in the original development of spiral antennas [23]. The most widely accepted heuristic explanation for the radiation mechanism of two-wire spiral antennas was proposed in the 'band theory' developed by B.H. Burdine and is included here for theoretical completeness [18, 9].

Spiral antennas follow the principles of a slow-wave or periodic type structure. The design can be visualized as an antenna containing within its design structure, consecutive radiating dipole pairs that are frequency self-selecting by the application of an exciting signal within its operational frequency. This can best be understood by imagining sets of dipole antennas of specific lengths connected in series, starting with the highest resonant frequency dipole and ending with the lowest. For a planar spiral, they are fed at the high-frequency end, at feed points A and B as shown in Figure 2-2(a) [21].

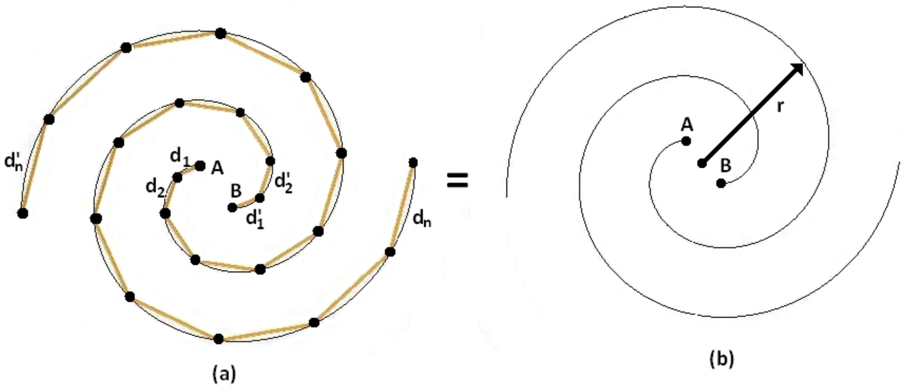

Figure 2-2: Evolution of series connected dipoles into the Archimedean spiral antenna (a) Dipole pairs (b) Evolution into spirals with no angles

Generally, a signal with a 180 degree out-of-phase current is applied at the input port of the antenna. The propagating current seeks out the dipole pair antenna that resonates, or brings the currents in phase, at the signal frequency passing from the highest frequency antenna pair $d_1 - d'_1$ toward the lowest frequency antenna pair $d_n - d'_n$. At the resonating point, the original out-of-phase current flows in phase as a result of the phase change caused by propagation over the differential distance between the dipole pair and the feed point. This differential distance assumes that one arm of the pair excites an adjacent arm, which when compared to the first arm can be evolved into a circular spiral by bending the finite dipoles, eliminating the d chords, and replacing them with an arithmetic spiral with an increasing radius r as shown in Figure 2-2 (b) [21].

A two-arm spiral antenna can be thought of as a two-wire transmission line which has gradually been transformed into a radiating structure [18]. Allowable radiation bands exist for all circles whose circumference is an integer number of wavelengths. In our work, we have studied the radiation properties of planar circular and rectangular spiral antennas and the radiation mechanism for both forms is presented here.

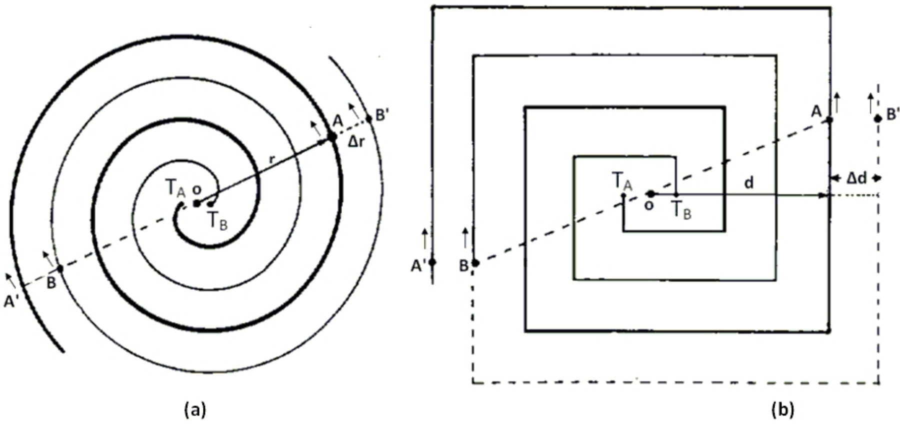

Figure 2-3: Band theory for (a) circular Archimedean spiral and (b) square spiral antenna

In Figure 2-3(a) we consider an isolated, closely wound, dual-arm circular spiral element in which the two arms are excited by currents of equal amplitude and 180 degrees out of phase [21]. Close to but some distance away from the origin, the currents in adjacent conductors are out-of-phase so that little or no radiation occurs. As we proceed further away from the origin along the curves, the phase relationship between the currents in adjacent conductors becomes random so that the net radiated energy in this region is small [21]. This situation persists until a diameter corresponding to a circle of circumference equal to one wavelength is approached. When this happens, the current in adjacent arms are in phase and the condition for effective radiation exists.

Let A be a point on one wire of the transmission line at a distance measured along the wire from the input terminal T_A. Then the point B on the other wire at the same distance from the input terminal T_B is situated diametrically opposite the point A with respect to the center O, and both A and B lie on the same circle centered at O [21]. The point A and its neighboring point B' (on the wire adjacent to A) lie at such arc distances from T_A and T_B respectively, that the difference of these distances is the arc length BB' along the spiral. If Δr, the spacing between wires is much smaller than r, then arc length BB' is approximately equal to πr. This difference in wire lengths does not depend on the number of turns within r if the spacing between wires is uniform [35].

A square spiral configuration shown in Fig. 2-3(b) radiates in a similar fashion. Here, for a cross-sectional point AB' on the two-wire line, the path difference in the two wire lengths is given approximately by $4d$, where d is the perpendicular distance from the center O to the side of the square spiral turn on which AB' lies. Also, the circumference of the turn on which AB' lies is approximately $8d$. This difference of $4d$ in wire lengths of the transmission line is independent of the number of turns appearing on the spiral, provided only that the spacing Δd between elements on the spiral is constant and small compared to d [18].

When $d = \frac{\lambda_e}{8}$, where λ_e is the current wavelength on the spiral, the phase change or total difference in wire length is $d = \frac{\lambda_e}{2}$, while the total circumferential path length is λ_e, or a quarter-wavelength on each side of the square. Phasing of the radiated field from opposite sides of the square is such as to add in a direction normal to the plane containing the spiral. Moreover, radiation from two adjacent sides is equal in intensity but with a relative phase difference of 90 electrical degrees, so that the radiated field normal to the plane of the spiral is circularly-polarized.

For the circular spiral, where again the wires are equally-spaced, at a point whose radial distance from the spiral center is r, we have difference in line lengths $= \pi r$ and circumference $= 2\pi r$. When r is $\frac{\lambda_e}{2\pi}$, the phase change is $d = \frac{\lambda_e}{2}$ and the circumference is λ_e. Assuming that each wire supports a progressive wave of current and that these current waves are anti-phase at the input terminals T_A and T_B, it is clear that the difference in phase of the two current elements at any point AB' on the two-wire line, measured in radians, is π (the input phase difference) + $\left(\frac{2\pi}{\lambda_e \pi r}\right)$. Thus neighboring current elements start anti-phase at the feed points T_A and T_B, and gradually come into phase as one proceeds outward along the spiral two-wire line. When $r = \frac{\lambda_e}{2\pi}$, these currents are precisely in phase and radiation is a maximum [18].

The direction of the arrow at B is opposite to that of the arm growth, and the two arrows at A and B are in the same direction. The current at A and the current at its neighboring point B' on arm B are in phase. Similarly, the current at B and the current at its neighboring point A' on arm A are in phase. Figure 2-2(a) illustrates these four currents at points A, B', B, and A', where each pair of currents forms a band of current. The condition for precisely in-phase currents occurs at two points diametrically opposite each other relative to the center O. The two current bands in Figure 2-2 (a) rotate around the center-point O with time. This means that the electric field radiated from each current band also rotates. In other words, the radiation field is circularly polarized. The two circularly polarized waves radiated from the two current bands are in phase on the z axis, resulting in maximum radiation on the z axis. This radiation is called 'first-mode radiation' [15]. Radiation from the spiral then is centered in an annular ring of turns of one wavelength mean circumference. This property makes the spiral antenna an inherently broadband device, the basic requirement being only that the radius be large enough to allow a half wavelength of phase-shift [18].

For every differential group of elements that have shifted 180 degrees in phase at the diameter of radiation, there is another group that is in both time and space quadrature since the phase of the groups is varying as a function of the spiral growth rate. This causes a 90 degree phase shift making the spiral response circular [21]. The circularity of the response is excellent at bands within the outer or largest ring degrading to linear polarization near the low-frequency or outer band edge and at the high-frequency end if radiation takes place at the connection of the feed line to the antenna structure [21].

2.3 Antenna Parameters

The performance of practical antenna systems is generally measured in terms of various parameters: parameters which describe spatial characteristics such as gain patterns and polarization, as well as quantities which describe terminal interfaces with the system, such as input impedance, S11, VSWR etc. are important factors in determining the performance of the antenna [11]. Throughout this work, we have used the following parameters to evaluate the radiation characteristics of cavity-backed spiral antennas.

2.3.1 Gain

The term antenna gain refers to the spatial gain of an antenna. Antenna gain is generally defined as the ratio of the power gain in a given direction to the power gain of a reference antenna in its reference direction. The input power is the same for both antennas and in most cases the reference antenna is a lossless isotropic source. When the direction is not explicitly stated, the power gain is assumed ot be in the direction of maximum radiation. Antenna gain takes into account the antenna radiation efficiency e_{cd}, where the input power to the antenna P_{in} is related to the radiated power P_{rad} by: $P_{rad} = e_{cd} \times P_{in}$.

The gain is then defined as 2.2, where $U(\theta, \phi)$ is the radiation intensity in (θ, ϕ) direction [6].

$$Gain(\theta, \phi) = e_{cd} \times 4\pi \times \left[\frac{U(\theta, \phi)}{P_{rad}} \right] \tag{2.2}$$

Spiral antennas radiate bidirectionally and have two major radiation lobes of different rotational sense. In our work, we have absorbed the back-lobe in the cavity and reduction of the gain of back-lobe to $\leq -10dB$ is considered a good design.

2.3.2 Axial Ratio

Axial ratio is one of the most important measure of performance for any circularly polarized antenna. The axial ratio is the ratio of orthogonal components of the electric field. Ideally, because the orthogonal components are equal in magnitude for a circularly polarized wave, the axial ratio is 1 (or 0 dB). The axial ratio for an ellipse is larger than 1 (≥ 0 dB). The axial ratio for a purely linearly polarized wave is infinite, because the orthogonal components of the field is zero.

In a practical antenna, the axial ratio tends to degrade away from the mainbeam of an antenna. Also, it is not possible to obtain purely circular polarization for ultra wideband systems. However, a commonly used figure of merit for axial ratio is $\leq 3dB$, which indicates a fairly good axial ratio performance. The axial ratio may be indicated in a manufacturer's data sheet for an antenna as $\leq 3dB$ for $\pm\delta$ degrees from mainbeam. This indicates that the deviation from circular polarization is $\leq 3dB$ over the specified angular range [4].

A point to to note here is that any polarization state can be represented as a linear combination of orthogonal states. An important special case is that a polarization state can be decomposed into orthogonal LHCP and RHCP states. In this case if E_{R0} and E_{L0} are the magnitudes of the LHCP and RHCP states respectively, then axial ratio is found from 2.3.

$$Axial\ Ratio = \frac{E_{R0} + E_{L0}}{E_{R0} - E_{L0}} \tag{2.3}$$

2.3.3 Beamwidth

The beamwidth or half-power beamwidth is defined as: "in a plane containing the direction of the maximum of a beam, the angle between the two directions in which the radiation intensity is one-half the maximum value of the beam." [6]

2.3.4 Input Impedance, VSWR and Reflection Coefficient

The interface between the antenna and the system electronics is an imporatant factor in antenna engineering. Maximum power transfer requires matched impedance characteristics, and deviations from ideal match result in reduced power transfer and are referred to as mismatch losses [11] Self-complementary antennas theoretically demonstrate constant input impedance over their operational bandwidth as mentioned in the previous chapter. In our simulations, we have assumed reference impedance 188Ω at the input port of all cavity-backed antenna models.

Voltage standing wave ratio and reflection coefficient (dB) quantities are also extracted as merits of system performance. These quantities are usually measured using a network analyzer, and the measurements are expressed in scattering matrix parameters. The reflected component reflection coefficient is denoted by $S11$. The mismatch loss equals $1 - |S11|^2$. Antenna impedance values are commonly specified by the voltage reflection coefficient S11, the return loss RL or the voltage standing wave ratio VSWR and are expressed as 2.4 [11].

$$\begin{aligned} &RL = 20 \times log(|S11|) \\ &and, \\ &VSWR = \frac{(1 + |S11|)}{(1 - |S11|)} \end{aligned} \tag{2.4}$$

Having both VSWR ≤ 2 and a reflection coefficient $S_{11} \leq -7dB$ is considered a fairly good design.

2.4 Analytical Methods/Numerical techniques

Electromagnetic problems are usually solved using advanced numerical techniques. Some solution methods are applicable in the frequency domain while others are more suited to the time domain. For design, simulation and analysis of results, common methods are the Method-of-Moments (MoM), Finite Element Analysis (FEM), Finite Difference Time Domain (FDTD) analysis, Transmission Line (TL) analysis or alternative formulations of these methods such as the recent revolution of Multi Level Fast Multi-pole Method (MLFMM) etc. These methods or hybrid techniques formulated from them are implemented in different suites of commercially developed software that has greatly facilitated antenna engineers. In addition to design and simulation of preliminary systems, it is also possible to optimize their physical dimensions and radiation characteristics by using built-in optimizers included in the software packages. This is an extremely attractive feature, because the genetic algorithm and the particle swarm algorithm which are used in these packages are very efficient optimization procedures for antenna development.

2.4.1 Method-of-Moments based Analysis

In time-domain-based methods, the problem space is discretized into volume-based unit cells that rapidly increase computation time and memory. In situations where primarily perfect electrical conductors are involved, the solution process becomes much simpler if surface meshes are used and then currents on these elements are solved using numerical techniques such as Method-of-Moments (MoM). This is particularly useful for electrically small problems and we have successfully used MoM based software FEKO, distributed by EMSS, USA, for all designs, simulation and extraction of necessary antenna parameters in this dissertation.

Chapter 3

Characterization, Design and Optimization of Low-Profile Absorptive Cavity

In this chapter, we discuss the methodology for the design and optimization of low-profile, absorptive spiral cavities from a microwave material characterization standpoint. First, we describe a high-precision measurement technique that accurately characterizes the complex permittivity and complex permeability at microwave frequencies. With this measurement method, we were able to experimentally obtain the accurate frequency dependent behavior of a set of commercially available dielectric and magnetic absorbers from 2-40 GHz [43].

From the complex permittivity and complex permeability thus measured, we analyzed the characteristic impedance and front-end reflection properties of these materials and designed a multi-layer cavity to operate from 2 to 18 GHz.

In EM simulation software FEKO, we modeled a 2-18 GHz Archimedean spiral antenna cavity. The frequency dependent permittivity and permeability equations obtained from our measurements were used to accurately model the behavior of the absorbing layers in the simulations. With the material properties thus appropriately defined in FEKO, we were also in a position to optimize the antenna dimensions such that the best radiation performance can be achieved with minimal antenna size.

Our results show that we have been able to obtain an efficient spiral antenna design taking into account the frequency-dependent properties of the materials incorporated into the antenna structure. The procedure can be successfully employed to design and optimize the dimensions of any broadband, cavity-backed, spiral antenna system in general.

3.1 Material Measurement and Characterization

The formulations used for material charaterization are included in this section for theoretical completeness.

3.1.1 Measurement Method

Absorbing materials were characterized using a transmission-reflection (T/R) based automated rectangular waveguide technique developed at the Microwaves, Millimeter Waves and THz Laboratory at Tufts University, Medford, Massachusetts. In this method, an Agilent Vector Network Analyzer was used to measure the S_{11} and S_{21} parameters when a sample of material was inserted inside a waveguide to form a two-port network. The method is based on the (T/R) technique introduced by Nicolson-Ross [32] and Weir [48], and the widely acclaimed formulations for transmission and reflection coefficients proposed by Baker-Jarvis [5].

In the measurement formulations, an improved methodology was used for the determination of electromagnetic properties of linear materials of reasonable thickness when placed inside a rectangular waveguide. The loaded material's magnetic and dielectric effects was taken into account in the calculation of cutoff wavelength of the propagation constant. Using the procedure, it is possible to simultaneously determine the complex permittivity and complex permeability values for two-dimensional samples of reasonable thickness without requiring any guess parameter or having any phase ambiguity in the material characterization process [3]. For our purposes, in the case of linear absorbing microwave materials, the methodology offered high precision in determining the complex permittivity and permeability of 19 absorbing samples that were initially used in the study of designing broadband absorbers [43].

3.1.2 Formulations for Determination of Complex Permittivity and Complex Permeability

Linear Microwave Materials

The methodology begins with formulations based on the work of Nicolson, Weir [32, 48] for the determination of complex permittivity and permeability of linear microwave materials. A function K is defined which is dependent on measured S_{11} and S_{21} parameters from in-waveguide measurements of a device under test as 3.1.

$$K = \frac{\tilde{S}_{11}^2 - \tilde{S}_{21}^2 + 1}{2\tilde{S}_{11}} \tag{3.1}$$

Then the reflection coefficient Γ and transmission coefficient T are derived according to 3.2 and 3.3 [32, 48].

$$\Gamma = K \pm \sqrt{K^2 - 1} \tag{3.2}$$

$$T = \frac{\tilde{S}_{11} + \tilde{S}_{21} - \Gamma}{1 - (\tilde{S}_{11} + S_{21})\Gamma} \tag{3.3}$$

After the reflection and transmission coefficients have been calculated from experimentally obtained S parameters, the propagation constant inside the waveguide can be calculated from 3.4, where γ_{TE10} is propagation constant for the TE_{10} mode with the material inserted in the waveguide, Φ_t is the phase of transmission coefficient and d is the material thickness [5, 8].

$$\gamma_{TE10} = \frac{ln\frac{1}{|T|}}{d} + j(\frac{2\pi n - \Phi_t}{d}) \tag{3.4}$$

Prior experimental results have demonstrated that the material under test affects the cutoff wavelength of the propagation constant. Taking into account the loaded material's magnetic and dielectric effects in the calculation of the cutoff wavelength of the propagation constant, and it is possible to write γ_{TE10} as 3.5. Here, the term γ^0_{TE10} is defined to simplify the equations [33].

$$\begin{aligned} \gamma_{TE10} &= j2\pi\sqrt{(\frac{1}{\lambda_0})^2 - (\frac{1}{2a})^2} \times \sqrt{\mu\epsilon} = \gamma^0_{TE10}(\frac{\mu}{\eta}) \\ \gamma^0_{TE10} &= 2\pi\sqrt{(\frac{1}{\lambda_0})^2 - (\frac{1}{2a})^2} \end{aligned} \tag{3.5}$$

This formulation allows one to write symmetrical and simultaneous permittivity and permeability equations for waveguide-based techniques. The final equations for simultaneous calculation of the complex permeability and permittivity are given in 3.6 and 3.7 [3, 33].

$$\mu = \frac{\eta \times \gamma_{TE10}}{j \times \gamma^0_{TE10}} = -j(\frac{1+\Gamma}{1-\Gamma})(\frac{1}{2\pi d})(\frac{ln\frac{1}{|T|} + j(2\pi n - \Phi_t)}{\sqrt{(\frac{1}{\lambda_0})^2 - (\frac{1}{2a})^2}}) \tag{3.6}$$

$$\epsilon = -j(\frac{c}{f})^2(\frac{1+\Gamma}{1-\Gamma})(\frac{1}{2\pi d})(ln\frac{1}{|T|} + j(2\pi n - \Phi_t))(\sqrt{(\frac{1}{\lambda_0})^2 - (\frac{1}{2a})^2}) \tag{3.7}$$

Symmetrical Relationships and Formulations for Non-reciprocal Circuits

In free-space measurement methods and coaxial cable-based techniques, the equivalent impedance and the refractive index do not have to take into account any geometrical context. Only the medium's impedance and the medium's refractive index is of primary importance. But a waveguide has a cutoff frequency and a certain geometry, and when these factors were taken into account, one can only be able to formulate simultaneous equations for permittivity ϵ and permeability μ as mentioned in 3.6 and

3.7, but also able to express ϵ and μ in terms of equivalent impedance Z_{eq} and equivalent refractive index n_{eq}. The equivalent impedance Z_{eq} and equivalent refractive index n_{eq} are defined in terms of wave impedance η and refractive index of the media $\tilde{n}$ is defined by 3.8, 3.9, 3.10 and 3.11 [12, 33].

$$Z_{eq} = \eta(1 - \frac{\lambda_0}{2a}^2)^{\dfrac{-1}{2}} \tag{3.8}$$

$$n_{eq} = \frac{\gamma_{TE10}}{\gamma_0} = (\frac{2\pi}{\lambda_0})\gamma_{TE10} = \tilde{n}(1 - \frac{\lambda_0}{2a}^2)^{\dfrac{-1}{2}} \tag{3.9}$$

$$\eta = \frac{1+\Gamma}{1-\Gamma},\ and\ \tilde{n} = \kappa + jn \tag{3.10}$$

$$\gamma_{TE10} = \frac{ln\dfrac{1}{|T|}}{d} + j(\frac{2\pi n - \Phi_t}{d}) \tag{3.11}$$

Using 3.8 to 3.11, the effective permittivity and permeability equations become 3.12 and (3.13, which resembles closely symmetrical relationships derived from previous methods [36, 33].

$$\mu = -jZ_{eq}n_{eq} \tag{3.12}$$

$$\epsilon = -j\frac{n_{eq}}{Z_{eq}} \tag{3.13}$$

The method has been validated for waveguide-based formulations and also for non-reciprocal circuits. This is because initial methods depended on all four S parameters and assumed reciprocity by requiring that $S_{11} = S_{22}$ and $S_{21} = S_{12}$. It is possible to calculate permittivity and permeability from S_{11} and S_{21} parameters only and the network does not need to be in a reciprocal state.

Formulations for Thick Samples

In the case of specimens that are relatively thick, the wave partially penetrates the sample and gets partially reflected from somewhere inside the specimen and the S_{11} recording cannot be used as reliably to calculate the impedance and refractive index of these materials. However, the transmission S_{21} is unaffected and an additional set of equations are derived for calculating the refractive index in terms of S_{21} only [34]. For the method to be valid in the case of thick samples, the samples have to be fully loaded inside the shim with no air gaps present. Cauchy-Riemann equations are used to extrapolate the refractive index due to slope differentiation with formulations from 3.14 to 3.16 [34, 36].

$$\Psi = \gamma_{TE10}^{0}\tilde{n} = j\gamma_{TE10}^{0}(n - jk)l = \phi_0 k + j\phi_0 n = \phi_L + j\phi_P \tag{3.14}$$

The Cauchy-Riemann equations are used in the following manner according to 3.15 and 3.16 [34].

$$\begin{gathered} \frac{\partial \phi_L}{\partial k} = \frac{\partial \phi_P}{\partial n} \\ \frac{\partial \phi_P}{\partial k} = -\frac{\partial \phi_L}{\partial n} \end{gathered} \tag{3.15}$$

$$n = k\frac{\partial \phi_P}{\partial \omega}\left(\frac{\partial \phi_L}{\partial \omega}\right)^{-1} \tag{3.16}$$

From 3.16, it was observed that since it is a differential equation, only the slope at a limited number of frequencies are required instead of the entire spectra, as in the case of linear equation formulations, which simplifies the calculations to a great extent. The medium impedance is derived with 3.17 [34].

$$\eta = \frac{2\sinh(\gamma_{TE10})d}{\frac{(1 - S_{11})^2}{S_{21}} - S_{21}} \tag{3.17}$$

Finally, the relative permittivity of the microwave material is calculated from 3.18, where, $f_c^{air} = \frac{c}{2a}$, c is the speed of light, and a is the longer axis of rectangular waveguide [33].

$$\epsilon_r = \epsilon + \left(\frac{f_c^{air}}{f}\right)^2 \tag{3.18}$$

It was observed that the effective permeability from the rectangular waveguide and relative permeability of microwave materials are equal [33].

Formulations for Resonant Materials

For accurate characterization of resonant microwave systems, the spatial dependence of the return loss of microwave materials is taken into account. The terms Γ, T, S_{11}, and S_{21} is redefined using 3.19 to 3.21 [5, 33].

$$\Gamma = \frac{\eta - 1}{\eta + 1}, and\ \eta = \sqrt{\frac{\mu}{\epsilon}} \tag{3.19}$$

$$T = e^{-\gamma d} = e^{-(\frac{\omega}{c})d.\tilde{n}(1-(\frac{f_c}{f})^2)^{\frac{1}{2}}} \tag{3.20}$$

$$\begin{aligned} S_{11}(\omega) &= \frac{(1-\Gamma^2)T}{1-T^2\Gamma^2} \\ S_{21}(\omega) &= \frac{(1-T^2)\Gamma}{1-T^2\Gamma^2} \end{aligned} \tag{3.21}$$

In light of equations 3.19 to 3.21, if T is equal to ±1, then $(\frac{\omega}{c})d\sqrt{\mu_r\epsilon_r} = \pi$, which is the condition required to satisfy the mathematical requirements set forth in equation 3.19, and this leads to an absorption peak in the S_{11} spectrum. An accurate return loss elimination procedure allows one to further extend this concept to determine very accurately the permeability and permittivity of microwave resonant systems using 3.19 to 3.21 [36].

3.1.3 Accuracy of the Measurement Technique

The high precision of the measurement method has been demonstrated from measurement results of materials that are difficult to characterize. For instance, Aerogel materials have permeability and permittivity values very near to air. Using this method, it is possible to differentiate the material properties from air. The precision in waveguide technique can be attributed to the elimination of phase ambiguities and of the requirement for any guess parameters during the determination process. The proposed method works very well to determine the permittivity and permeability of microwave materials at their resonant frequency [34, 36].

The formulations described here are mathematically consistent with all prior formulations and measured data with this methodology has been experimentally verified to show precise and accurate results. The methodology has gradually progressed from linear materials to non-reciprocal resonant systems with no conflict with any other established method. In related work, it was shown that this work can be extended to the characterization of meta-materialized structures and similar precision and accuracy can be obtained in determining the negative refractive index spectra [36].

3.1.4 Characterization of Linear Microwave Absorbing Materials

As indicated in the manufacturer's data sheets, the prospective materials for an absorbing cavity have been tested for their attenuation and typical reflectivity based on normal incident wave as an indicator of their absorption capabilities. No information, however, was available as to how their material constitutive properties change with frequency. We have derived their precise frequency dependent material properties from 2-40 GHz using our measurement method [43].

Complex Permittivity and Permeability

For the design of multi-layer absorbers to be constructed as hybrid composites of both magnetic and dielectric absorbing materials, we characterized a set of 19 commercially available dielectric and magnetic absorbers useful in different bands of the microwave spectrum. We used this data to design a hybrid broadband absorber composed of three layers of absorbing materials which provides absorption from 2-18 GHz.

The front layer (of AN series, Emerson and Cumming) is a carbon-loaded polyurethane foam absorber which typically provides -20 dB insertion loss in frequencies above 3.5 GHz but gave the closest impedance match to free-space. The middle layer (LS-

10055, ARC technologies) is a flexible, low-density and high loss carbon loaded foam. The metal-backed 3rd layer is an iron-loaded, magnetic thermoplastic elastomer (WT-BPJA-010, ARC technologies) typically designed for attenuation in the +1 GHz range. In order for the waveguide-based characterization process to work accurately, the samples were carefully sized to fit in 8 different waveguide bands and their surfaces were kept as planar and normal to the incident wave as mechanically possible during the measurements.

The resultant material properties for the three final absorbing layers eventually selected for the composite structure, are shown in Figures 3-1, 3-2 and 3-2 [43].

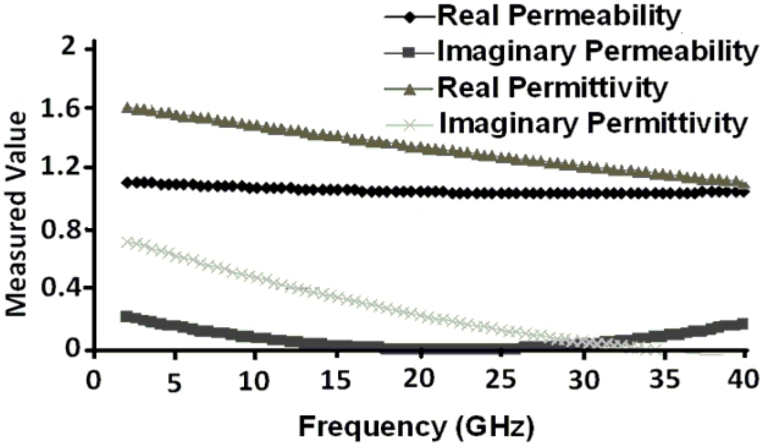

Figure 3-1: Measured constitutive parameters for the first layer (AN-74)

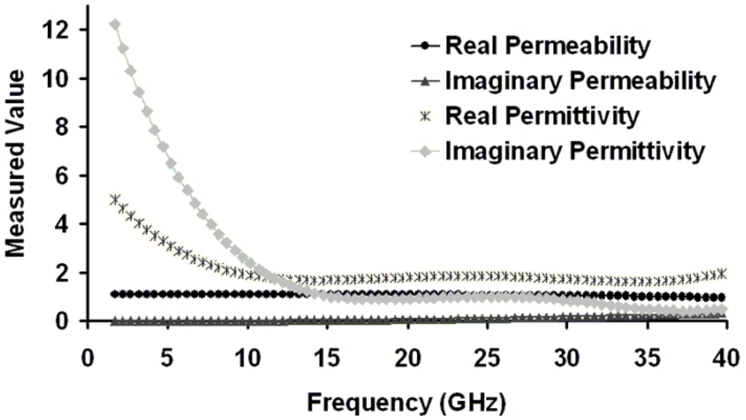

Figure 3-2: Measured constitutive parameters for the middle layer (LS-10055)

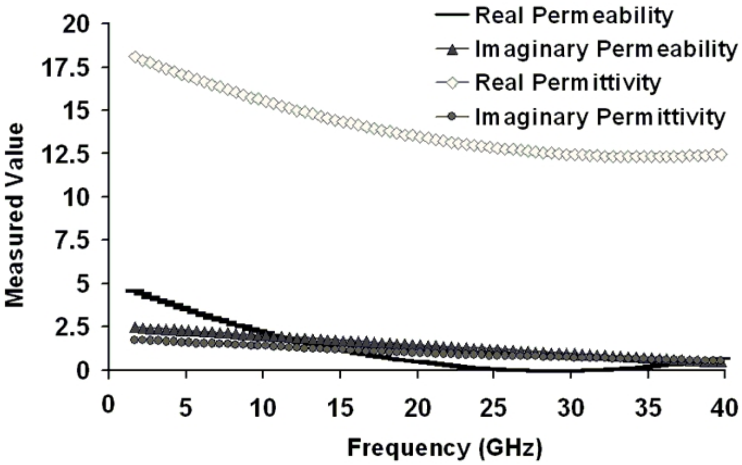

Figure 3-3: Measured constitutive parameters for the third metal-backed layer (WT-BPJA-010)

Relating Material Properties to Frequency

From the experimentally obtained data, we used curve-fitting methods to obtain mathematical relations between material constitutive parameters and frequency. The equations for the real part of permittivity, permeability and the loss tangent (defined as imaginary part over real part) of the materials enabled us to replicate the behavior of the absorbing materials in FEKO with their frequency dependent characteristic equations incorporated in the CADFEKO modeler. The derived equations for the three layers are given from 3.22 through 3.24, where f is the frequency in GHz [43].

First Layer at the Air-Absorber Interface

$$\begin{gathered}\textit{permittivity}, \epsilon = 0.0036f^2 - 0.0872f + 1.659 \\ \textit{dielectric loss tangent}, \tan\delta_\epsilon = 0.0027f^2 - 0.0763f + 0.5838\end{gathered} \tag{3.22}$$

Middle Layer

$$\begin{gathered}\textit{permittivity}, \epsilon = 0.006f^2 - 0.2885f + 4.7022 \\ \textit{dielectric loss tangent}, \tan\delta_\epsilon = 0.0031f^2 - 0.1785f + 2.8427 \\ \textit{permeability}, \mu = -0.0002f^2 + 0.0035f + 1.0939 \\ \textit{magetic loss tangent}, \tan\delta_\mu = 0.0002f^2 - 0.0012f + 0.0028\end{gathered} \tag{3.23}$$

Metal-Backed Third Layer

$$\begin{aligned}
&\textit{permittivity}, \epsilon = 0.0052f^2 - 0.3645f + 18.685 \\
&\textit{dielectric loss tangent}, \tan\delta_\epsilon = -5 \times 10^{-05} f^2 - 0.0003f + 0.0914 \\
&\textit{permeability}, \mu = 0.0062f^2 - 0.3585f + 5.1446 \\
&\textit{magetic loss tangent}, \tan\delta_\mu = -0.0067f^2 + 0.2039f + 0.0232
\end{aligned} \tag{3.24}$$

3.2 Design of Broadband Multi-Layer Absorbers for Shallow Cavities

3.2.1 Reflectivity Analysis

To determine the thickness of an absorbing layer at the frequency of maximum attenuation, the reflection spectrum of each sample was analyzed from 2 to 40 GHz. The position of the reflection minima as a function of thickness for each metal-backed absorber indicated the approximate frequency range and thickness for maximum absorption inside the absorber [42].

For instance, Figure 3-4 shows the reflection coefficient of sample WT-BPJA-010 as a function of frequency. It is a narrowband absorber and exhibits strong absorption at 5 GHz when the thickness is 0.18 cm.

3.2.2 Design Algorithm for Shallow Composite

With the goal of designing a sufficiently low profile spiral cavity, we populated our database with the most accurate and precise complex permittivity and permeability information and thickness of maximum attenuation from 2-40 GHz for all dielectric and magnetic absorbers in our sample space. The materials were then categorized in frequency subdivisions according to their reflection minima. If a sample showed different absorption peaks for different thicknesses, it was repeated and included in all frequency subdivisions.

A computer code requested user input for operational bandwidth and maximum allowable cavity depth of the spiral antenna. The program generates a list of suitable

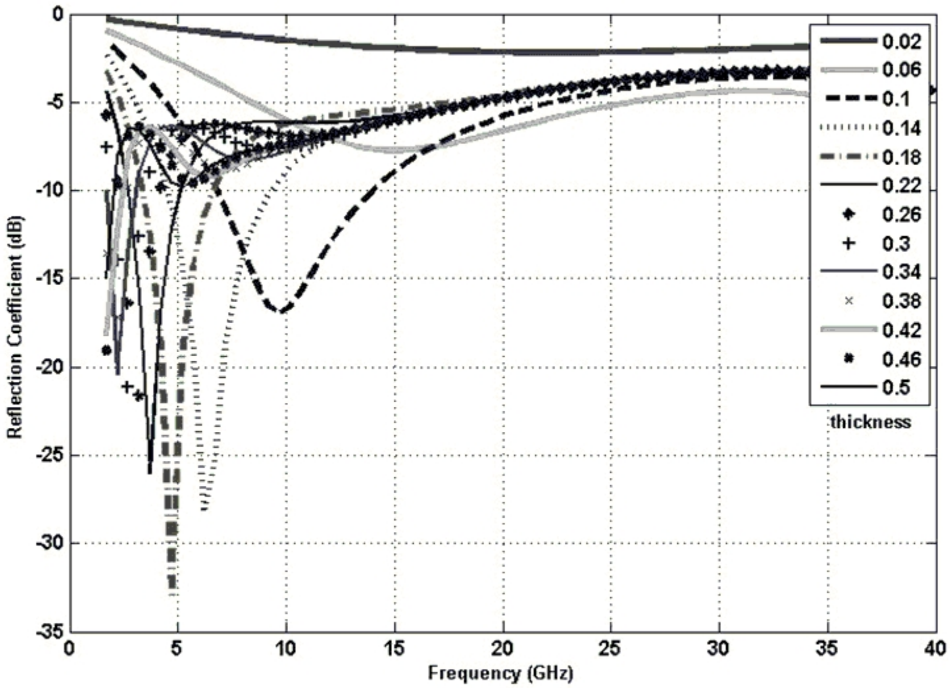

Figure 3-4: Reflection Coefficient of BPJA010 as a function of frequency. It is a narrowband absorber and exhibits strong absorption at 5 GHz

materials for the hybrid composite and the corresponding thickness values for each material determined from the reflectivity analysis that would provide absorption in the requested frequency range. The code also ensured that if a lower frequency in the vicinity of 2 GHz is requested, then at least one layer of magnetic absorber is selected within the specified bandwidth and that the total thickness does not exceed the specified the cavity depth.

For all possible arrangements of placing M layers of materials in the composite [with M factorial (M!) possible arrangements], the equivalent impedance and reflection coefficient at the front surface is calculated from the material data. The arrangement that results in the shallowest possible cavity, reflection coefficient ≤ -10 dB throughout the operational bandwidth and front-end input impedance $\simeq 377\Omega$ is selected as an approximate cavity dimension. For a 2-18 GHz, 2-arm Archimedean spiral antenna, the initial dimensions and the order of arrangement we obtained are composite absorber thickness of 0.541 inches (metal backed MAGRAM absorber: 0.102 inches, middle layer LS-10055: 0.189 inches and AN-74 front interface layer: 0.25 inches).

In our theoretical analysis, we have assumed plane wave propagation and designed for minimum specular reflections in thin composites for low-profile antennas. The design serves to provide a good approximation for the dimensions of a sufficiently shallow cavity with a maximum allowable depth. The initial approximation sufficed for an ultra-wideband spiral operating at 2-18 GHz. This is because the frequency dependent active region of the spiral radiator is an annular region of current loops in the order of one wavelength. Except at the lowest frequencies, the composite could be considered located in the far field.

Furthermore, since FEKO solves the full 3D problem according to Maxwell's equations implying combined near-field and far-field behavior, when the composite is placed in a cavity of a spiral antenna, the simulation takes into account the entire volumetric space. Therefore, in the simulations, as with the physical case, the cavity absorbs energy from impressed fields regardless of whether the fields are impressed as near field sources, excited and radiating metallic structures or incident plane waves. With the precision material characterization data and an approximation for the cavity dimensions available, it was possible to accurately simulate the antenna in FEKO by incorporating the frequency dependent relative permittivity, permeability and loss behavior of the absorbing materials in the model. The behavior was replicated by defining the material properties by using equations 3.22 through 3.24 in the simulation software. Optimization algorithms were then used on the spiral antenna dimensions to further reduce the depth of the cavity and improve the radiation performance [2].

3.3 Optimization of Cavity-Backed Spiral Antenna

In our study, we used the genetic algorithm optimization approach to achieve the thinnest cavity dimensions that maintains good radiation performance. Since most optimization algorithms have the potential to converge to local optima, we chose a global optimization technique to derive the most favorable geometry of the cavity. Due to time and memory constraints, the number of iterations that the optimizer could use was limited to 80. The search process would stop either on convergence of the algorithm or upon completion of 80 solver runs, whichever occurred first. The optima obtained in those iterations were taken as the final solution. The approximate suggested dimensions obtained from our theoretical design described in the previous section were set as the initial optimization parameter values [43].

Multiple objectives were defined in this search to improve the overall performance of the shallow cavity-backed spiral antenna. Our goal was to optimize the thickness of each layer and depth of the cavity such that the RHCP gain or co-pol gain of the spiral is maximized, LHCP gain or cross-pol gain is minimized, front-end reflection from the absorbing layers minimized, and axial ratio minimized over the entire bandwidth of operation.

3.4 Results

3.4.1 Basic Spiral Geometry

In the preliminary design and optimization process of a low-profile cavity, we assumed a basic 2-arm, 27 turn, Archimedean spiral antenna with inner radius 0.015 inches, outer radius 1.2 inches and spiral proportionality constant $\Phi_s = 0.007$ inch/radian (0.18mm/radian).

3.4.2 Cavity Dimensions from the FEKO Optimizer

For a 2-18 GHz Archimedean spiral, a minimum composite absorber thickness of 0.476 inches (metal backed MAGRAM absorber 0.098 inches, middle layer LS-10055 0.125 inches and AN-74 front interface layer 0.0253 inches) and a 0.148 inch air gap between the antenna and absorbing layers gave the best broadband co-polarized gain and axial ratio performance.

This completes the final step in the design and optimization of an ultra-wideband cavity-backed spiral antenna system. With the broad spectrum permittivity and permeability data accurately obtained from a precision microwave measurement method, we have been able to achieve a fairly shallow cavity of 0.625 inches and thereby reduce the weight of the antenna by incorporating the data in the optimizer tool. Our methodology can be extended generally to the efficient development of any lightweight and ultra-wideband classical absorptive cavity-backed spiral antenna.

3.4.3 Antenna Radiation Properties

Gain

The boresight gains for both principle planes of the optimized antenna are shown in Table 3.1.

Table 3.1: CO-POL AND CROSS-POL GAIN OF OPTIMIZED ANTENNA

	Gain (dB) ($\Phi = 0°$)		Gain (dB) ($\Phi = 90°$)	
f(GHz)	RHCP	LHCP	RHCP	LHCP
2	-1.03	-23.40	-1.03	-23.40
6	6.46	-33.70	6.46	-33.70
10	5.46	-59.42	5.46	-59.42
14	5.12	-66.12	5.12	-66.12
18	5.66	-52.46	5.66	-52.46

It can be observed that throughout the operational band, co-polarized gain values were maintained above 5dB for the most part, while cross-polarized gains were reduced to as low as -66.12 dB. Thus the optimized antenna demonstrates sufficiently high gains, low side lobes and no splits in the main beam for the entire frequency range of interest. Figure 3-5 shows gain plots of the optimized cavity backed antenna at 2, 10 and 18 GHz.

Axial Ratio

Figure 3-6 shows the axial ratio on boresight. It is desired that Archimedean spiral antennas have circular polarization broadside to the antenna. The axial ratio was fairly less than 1.16 dB and most cases, close to 0 across the entire band. It is evident that the purity of circular polarization was sufficiently retained.

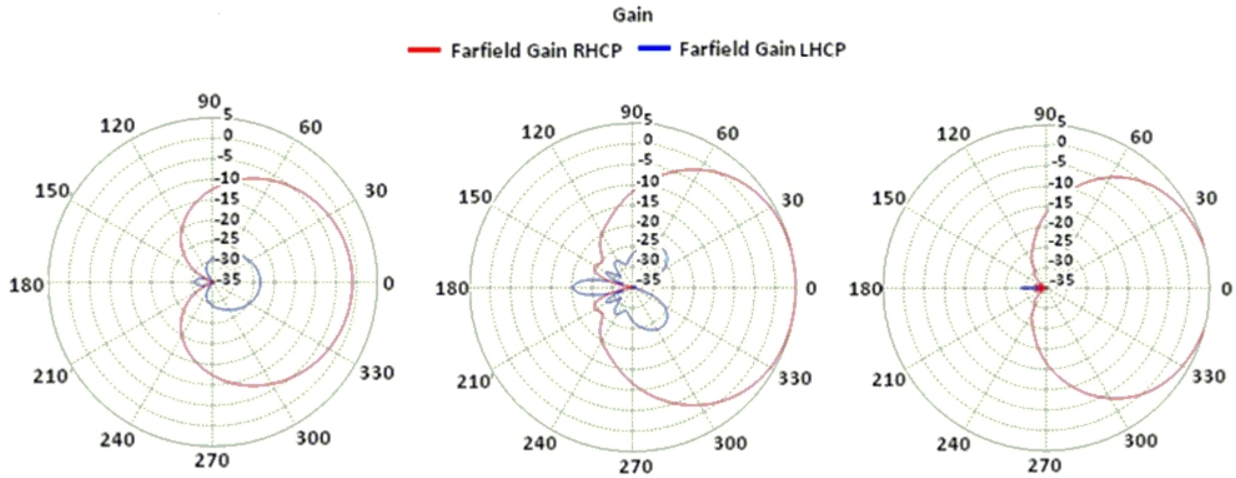

Figure 3-5: Low-band (2 GHz), mid-band (10 GHz) and high-band (18 GHz) gain plots

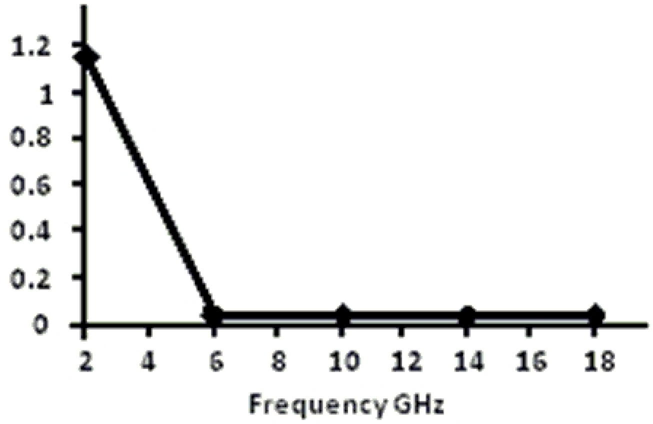

Figure 3-6: Axial ratio performance vs. frequency

Reflection Coefficient

Figure 3-7 shows the reflection coefficient at the antenna input port assuming matched conditions. Minimizing front-end reflection was one of the optimization goals in OPT-FEKO while varying the thickness of the layers. The results show that the reflection coefficient is efficiently minimized to acceptable levels across the bandwidth.

VSWR

Figure 3-8 shows the VSWR performance of the optimized cavity-backed spiral antenna. The VSWR is referenced to 188 Ohms and is less than 2:1 for the entire

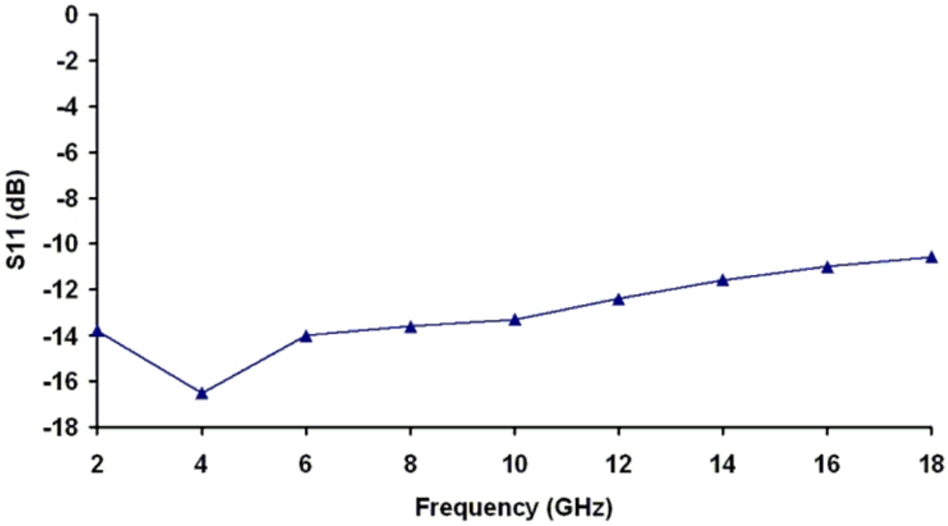

Figure 3-7: Reflection coefficient vs. frequency

bandwidth of operation.

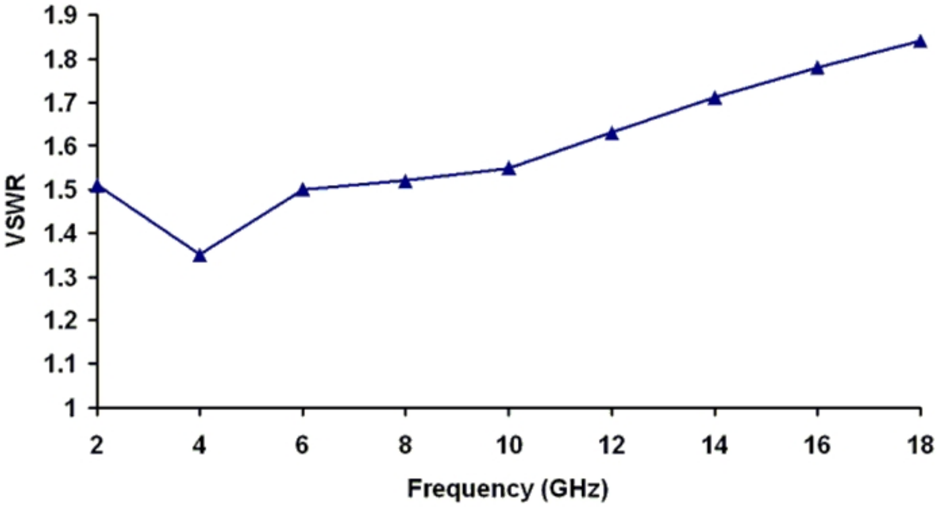

Figure 3-8: VSWR vs. frequency

Input Impedance

Figure 3-9 shows the input impedance to the cavity-backed Archimedean spiral antenna. The antenna maintains its principle of self-complementarity and realizes a near constant input impedance structure over an ultra-wide bandwidth.

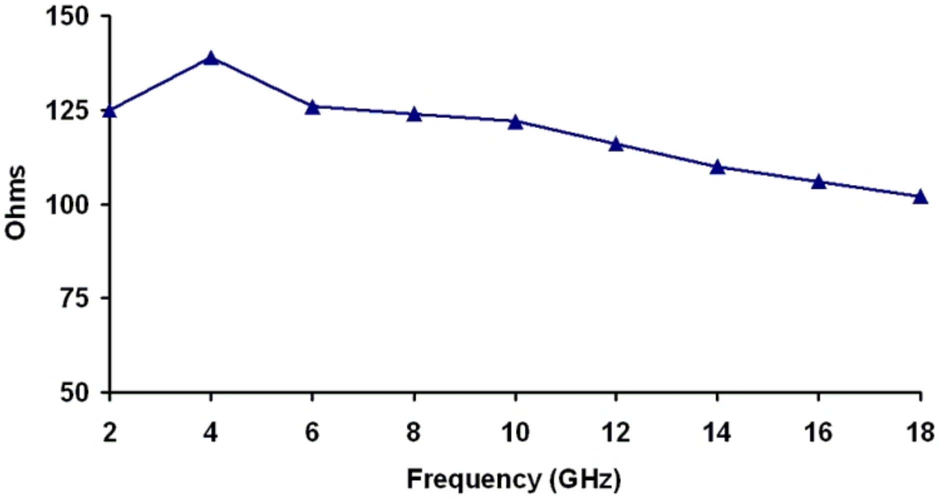

Figure 3-9: Input impedance vs. frequency

3.5 Discussion

3.5.1 Performance Comparison with Reference Spiral

To verify the performance of the newly-developed shallow cavity, the radiation properties of a spiral antenna backed with the optimized, shallow cavity was compared to that of a cavity-backed, reference Archimedean spiral antenna loaded with purely dielectric absorbing materials.

As mentioned earlier, it is very difficult to reduce the cavity depth to less than an inch using composite absorbing material of purely dielectric nature. For our purposes of comparison, we used a standard, commercially available, 3-layer composite dielectric absorber, AN 74, manufactured by Emerson and Cuming, to use in the reference absorbing cavity. Each layer of the reference composite is a carbon-loaded polyurethane foam absorber which typically provides -20 dB insertion loss at different frequency bands from 2-18 GHz. Industry specified non-optimized thicknesses for each absorbing layer was approximately 0.25 inches.

Using our previously outlined procedure, the complex dielectric permittivity ϵ_r of each layer of the AN-74 absorber was accurately characterized. Using the complex permittivity information thus obtained, the basic two-arm Archimedean spiral antenna was again simulated and optimized from 2-18 GHz. The lowest possible cavity depth we were able to obtain for satisfactory radiation performance was 0.978 inches, including the air-gap between the spiral radiator and the absorbing materials. The radiation characteristics of the 0.576 inch previously optimized, shallow, cavity-backed spiral were then compared to that of the relatively bulkier reference configuration.

Table 3.2 shows the simulated boresight gain and axial ratio performance of both configurations of cavity-backed simple circular spiral antenna.

Table 3.2: BORESIGHT RHC AND LHC GAIN AND AXIAL RATIO COMPARISON OF SPIRAL ANTENNA WITH AN-74 ABSORBER AND HYBRID ABSORBER IN CAVITY

f(GHz)	Boresight Gain (dB)				AR(dB)	
	AN-74		Hybrid			
	RHC	LHC	RHC	LHC	AN-74	Hybrid
2	2.33	-9.74	-1.03	-23.40	4.10	1.32
6	5.04	-62.19	6.46	-33.70	0.08	0.06
10	5.04	-71.20	5.46	-59.42	0.00	0.01
14	5.76	-72.46	5.12	-66.12	0.03	0.01
18	6.30	-45.25	5.66	-52.46	0.05	0.02

From the simulations we observed that the lightweight, hybrid cavity designed to operate from 2-18 GHz performs reasonably well compared to classical bulkier absorbing cavities with better axial ratio performance across the bandwidth.

From the simulations we observed that the lightweight, hybrid cavity designed to operate from 2-18 GHz performs reasonably well when compared to classical bulkier absorbing cavities, and has better axial ratio performance across the bandwidth. Thus we have been able to design and optimize a low-profile, shallow cavity from an existing database of a variety of magnetic and dielectric materials [39].

Since the near-field behavior of the basic spiral geometry has already been taken into account in the simulations, the optimized cavity configuration of the basic spiral can be effectively used to design spiral antennas with more complex geometry that would otherwise require significant computational resources to optimize. In this chapter, an effective design procedure for very low-profile, UWB, cavity-backed spiral antennas has been presented. We have approached the problem of designing and optimizing broadband, yet lightweight cavities by using microwave measurement techniques and subsequently applying the genetic algorithm optimization routine to arrive at a geometry that meets desired radiation specifications. In the following chapters, we demonstrate the efficiency of practical spiral radiators with hybrid absorptive cavities by designing, simulating and developing shallow cavity-backed, 2-arm, modified spiral antenna geometries and analyzing their radiation properties from 2-18 GHz.

Chapter 4

Low-Profile Slow-wave Spiral Antennas for Improved Axial Ratio

In the preliminary design and optimization process of a low-profile cavity, we assumed a basic 2-arm, 27 turn Archimedean spiral antenna as described in the previous chapter. The optimization of antenna cavity dimensions with absorptive materials required significant computational time and resources due to large number of iterations of the optimization algorithm. We used Method-of-Moments based FEKO for our purposes. A faster, more convenient MLFMM method was not possible to use efficiently due to the presence of the lossy materials in the cavity. However, since the multi-layer absorbing material is located well within the near field of cavity-backed antenna, an optimized shallow cavity based on the basic spiral geometry can now be successfully extended to other modified spiral geometries having equivalent antenna aperture and number of turns. In this chapter, we present the design, analysis and measurement results for a shallow cavity-backed, 2-18 GHz, slow-wave Archimedean spiral antenna with a zigzag profile.

For low profile cavity-backed spiral antennas, axial ratio is one the most important bandwidth factors. The lower limit of the bandwidth is determined by the outer antenna circumference and the upper limit is determined by the configuration near the feed points. At low frequencies, a spiral antenna tends to radiate from its outer arms. As a result, the reflected currents from the arm ends of the antenna increases [30]. The reflected currents create current standing waves on the spiral arms that disrupt the radiation pattern. The reflected currents radiate a circularly polarized wave with a rotational sense that is opposite to the circularly polarized wave generated by the outgoing current from the feedpoint. Now, the axial ratio can be expressed in terms of two orthogonal polarizations according to 4.1. From 4.1, it is evident that with the increase in reflected currents, the axial ratio performance decreases accordingly.

$$Axial\ Ratio = \frac{\mid E_R \mid + \mid E_L \mid}{\mid E_R \mid - \mid E_L \mid} \tag{4.1}$$

Reflection at the ends of the spiral can reduced by loading the arm ends with absorbing materials [28]. Another way would be to increase the number of turns sufficiently beyond the annular radiation ring in the lowest frequency of operation. These approaches can significantly increase the cost of fabrication or the antenna aperture. An efficient alternative would be to geometrically modify the spiral arms for better axial ratio performance. In this chapter, in order to improve the axial ratio performance at low frequencies, we have transformed the smooth arms of the antenna has into zigzag sections throughout its structure and created a slow wave antenna. The purpose of the modification on the basic spiral was to increase the circumference of the spiral in order to reduce the reflected currents, i. e. current standing waves at lower frequencies of operation and improve the axial ratio performance while maintaining a low-profile configuration [1]. The two arms are wound symmetrically with respect to the origin and follow the pattern of the basic spiral used of equal aperture as described previously. The antenna was then simulated and fabricated and the comparison of the radiation patterns from simulation and measurements are presented here [38].

In all simulations, we have assumed matched conditions at the antenna input port and the excitation source impedance is set to 188Ω in accordance with Babinet-Booker's principle [6].

4.1 Antenna Geometry

4.1.1 Modified Slow-wave Antenna Geometry

To study the efficiency of practical spiral radiators with hybrid absorptive cavities, we designed, simulated and developed a shallow cavity-backed, 2-arm, modified, slow-wave Archimedean spiral antenna and analyzed its radiation properties from 2-18 GHz. The actual antenna geometry with a modified zigzag-shaped spiral arms is shown in Figure 4-1.

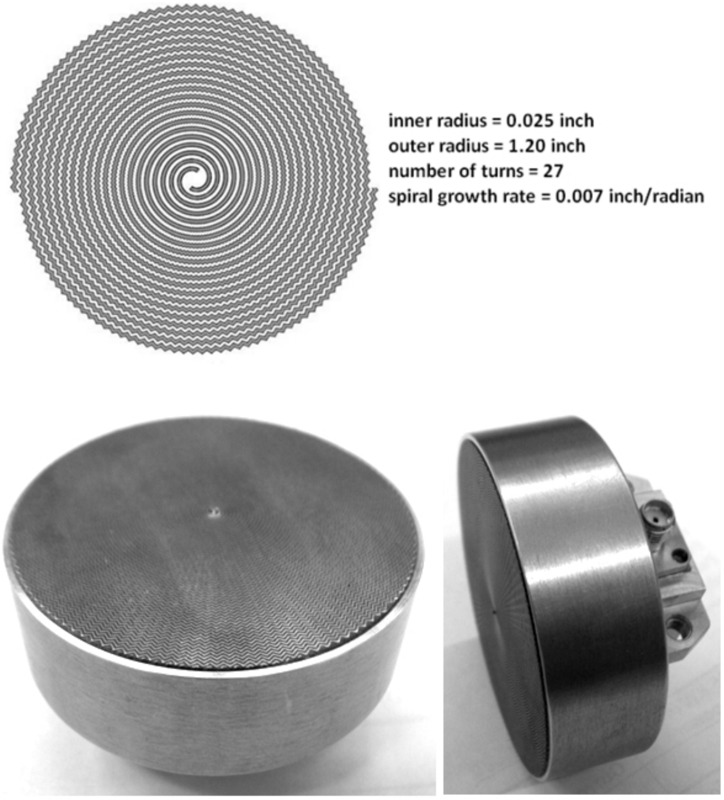

Figure 4-1: 2-arm, zigzag Archimedean spiral antenna with a shallow cavity

The antenna was simulated and fabricated with the following parameters: inner radius, $r_1 = 0.015$ inch, outer radius $r_2 = 1.2$ inch, number of turns $N = 27$ and spiral proportionality constant $\Phi_s = 0.007$ inch/radian (0.18mm/radian). The zigzag shape has been created by alternately adding and subtracting a delta radius 'dr' from the basic circular spiral. For the 27 turn spiral, the number of segments per turn was

240. The factor $'dr \times segment\ \#'$ increases from the center of the spiral creating an ever-increasing zigzag profile [40].

4.1.2 Cavity

The antenna is backed with a 2 inch diameter, shallow, multi-layer absorptive cavity developed earlier with three constituent absorbing materials. The front layer at the air-absorber interface (AN series, Emerson and Cumming) is a carbon-loaded polyurethane foam absorber. The middle layer (LS-10055, ARC technologies) is a flexible, low-density and high loss carbon loaded foam. The metal-backed 3rd layer is an iron-loaded, magnetic thermoplastic elastomer (WT-BPJA-010, ARC technologies. The cavity depth that ensures 2-18 GHz absorption for maximum gain-bandwidth performance is 0.625 inch including the air-gap between the radiator and the absorbing layers.

4.2 Results

4.2.1 Gain Simulations vs. Measurements

The full-wave analysis of the shallow cavity-backed Archimedean spiral antenna has been carried out with method-of-moments (MoM) based FEKO. The antenna was then fabricated and tested for its V-pol and H-pol gain components. Figures 4-2,4-3,4-4,4-5,4-6, compare the polar plots of the simulated gain (dBi) with the measured V-pol and H-pol gain for principal planes, $\Phi = 0°$ and $\Phi = 90°$, for 2, 6 10, 14 and 18 GHz.

4.2.2 Axial Ratio

Figure 4-7 shows the axial ratio on boresight. The antenna model demonstrates excellent polarization performance with axial ratio ≤ 2.7 dB, and in most cases, close to 0 dB, across the bandwidth. It is evident that the cavity-backed antenna has

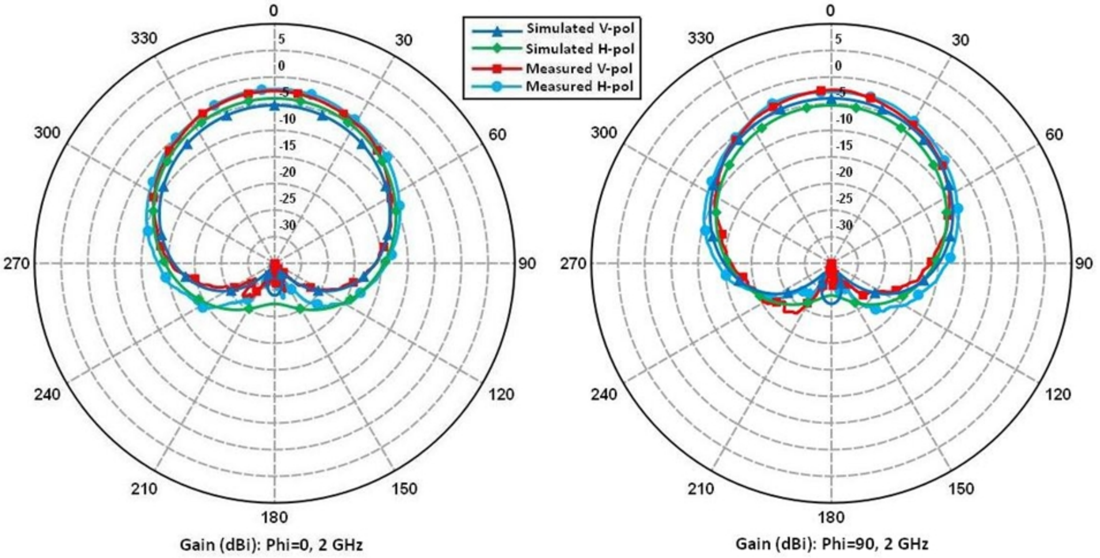

Figure 4-2: Measured vs. simulated gain (dBi) for principal planes at 2 GHz

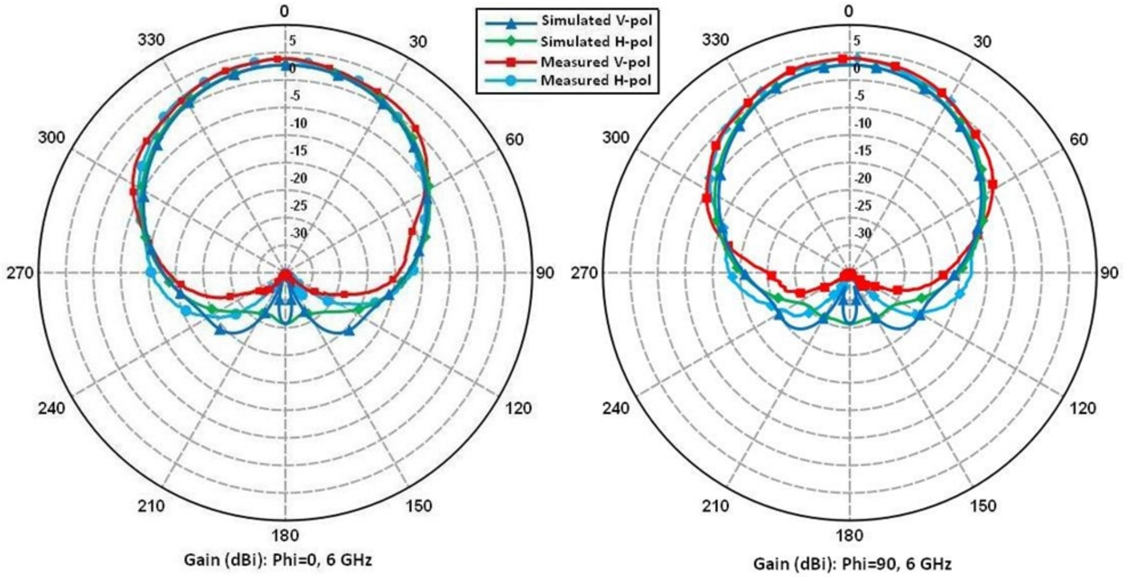

Figure 4-3: Measured vs. simulated gain (dBi) for principal planes at 6 GHz

preserved the purity of the circular polarization while maintaining a very low profile. The additional length added to the antenna using a zigzag profile has allowed for sufficient length to suppress the currents past the last radiation band.

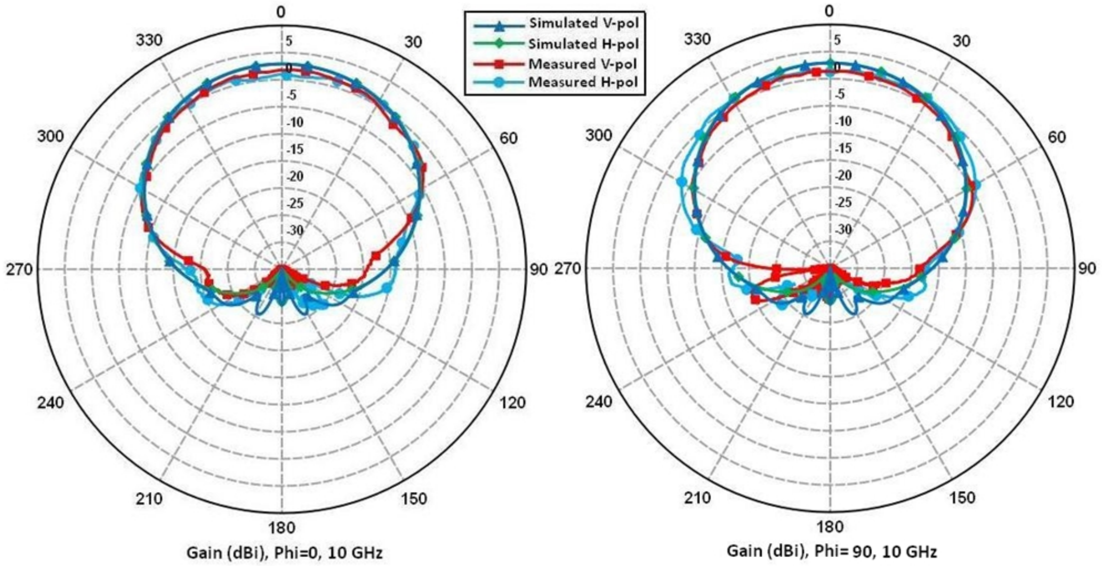

Gain (dBi), Phi=0, 10 GHz

Gain (dBi), Phi= 90, 10 GHz

Figure 4-4: Measured vs. simulated gain (dBi) for principal planes at 10 GHz

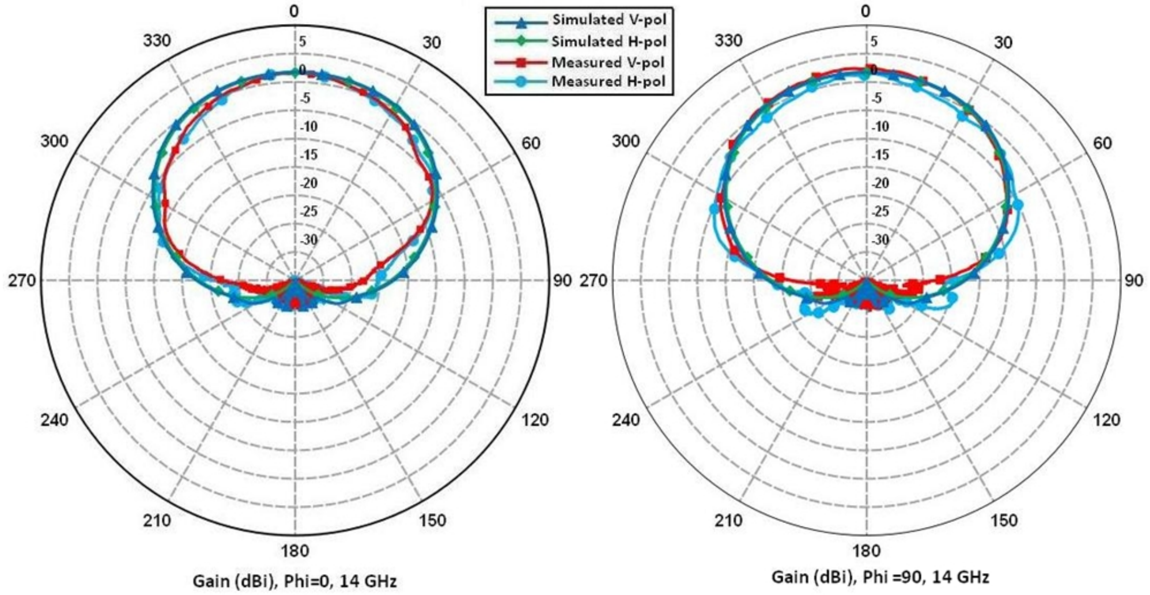

Gain (dBi), Phi=0, 14 GHz

Gain (dBi), Phi =90, 14 GHz

Figure 4-5: Measured vs. simulated gain (dBi) for principal planes at 14 GHz

4.2.3 VSWR

Figure 4-8 shows the VSWR performance of the optimized cavity-backed spiral antenna. The VSWR is referenced to 188 Ohms and is less than 2:1 for the entire bandwidth of operation, indicating a fairly good design.

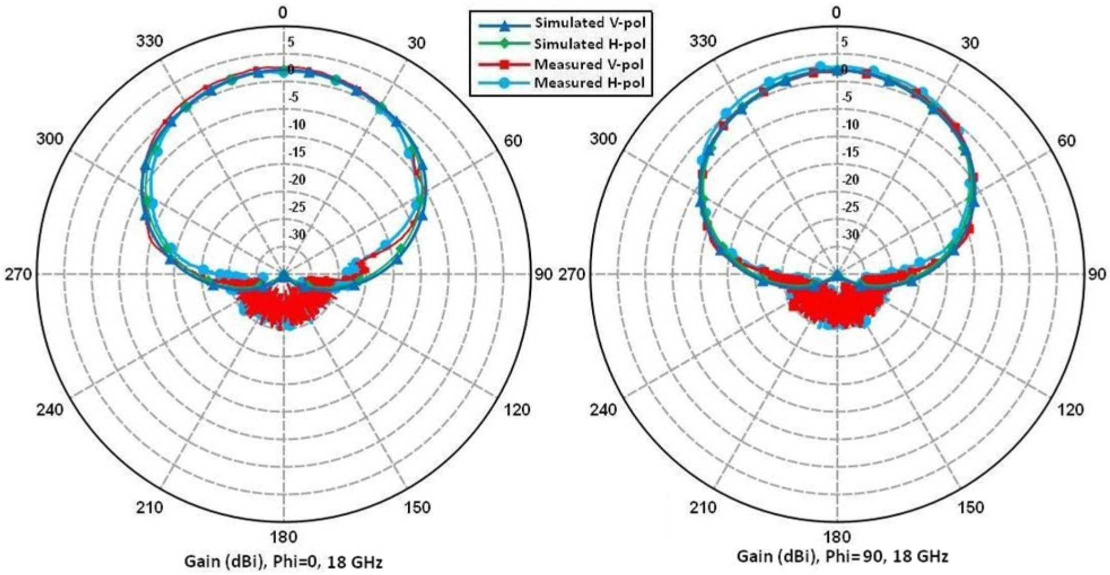

Figure 4-6: Measured vs. simulated gain (dBi) for principal planes at 18 GHz

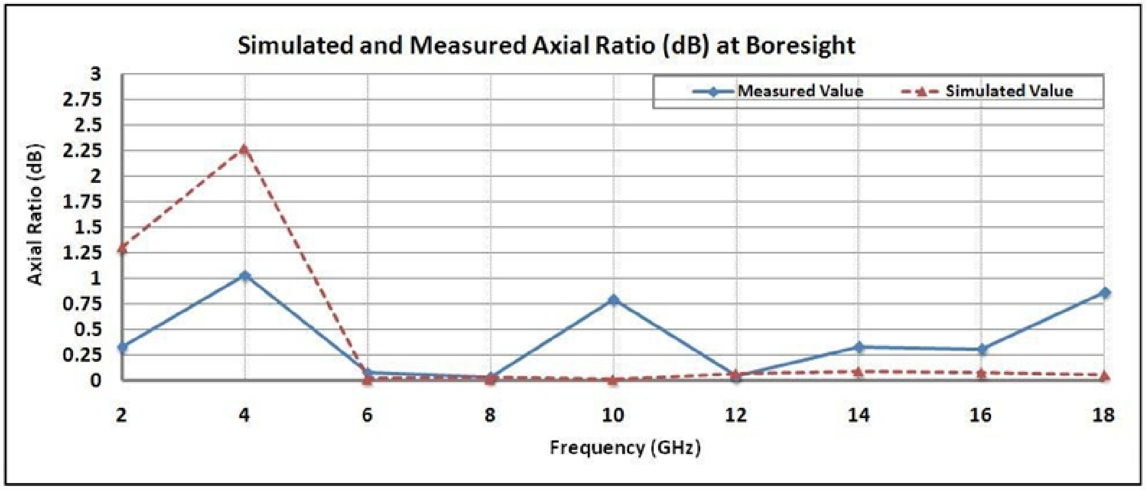

Figure 4-7: Axial ratio performance vs. frequency

4.2.4 Input Impedance

Figure 4-9 shows the input impedance to the cavity-backed Archimedean spiral antenna. The antenna realizes a near constant input impedance structure over an ultra-wide bandwidth.

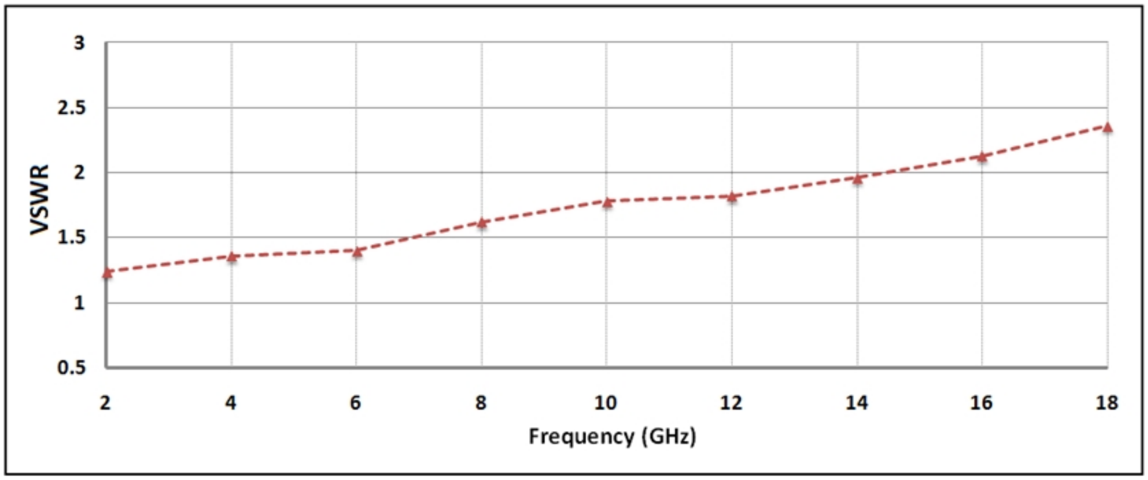

Figure 4-8: VSWR vs. Frequency (GHz)

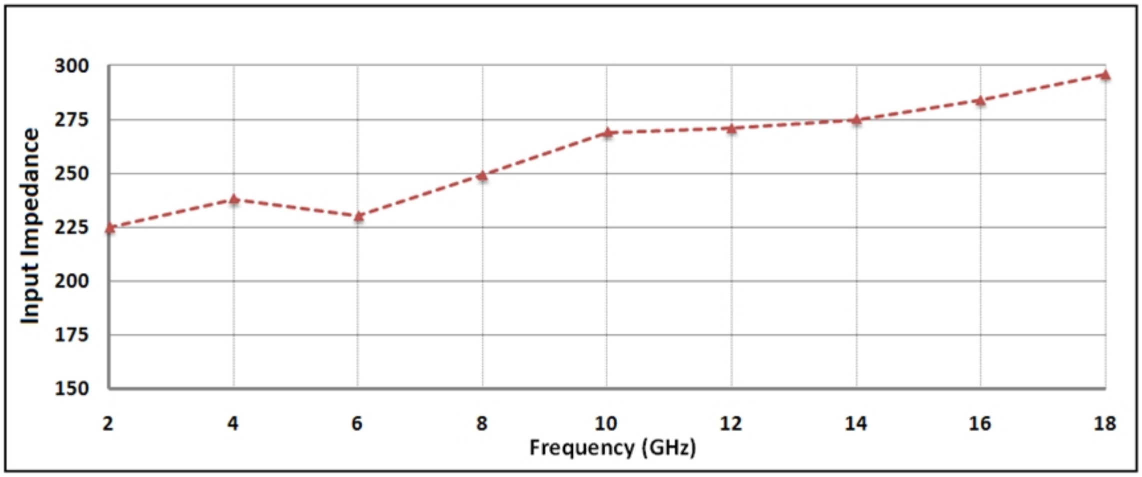

Figure 4-9: Input Impedance vs. Frequency (GHz)

4.2.5 S11

Figure 4-10 shows the reflection coefficient at the antenna input port assuming matched conditions. The results show that the reflection coefficient is efficiently minimized to ≤ 7 dB across the bandwidth.

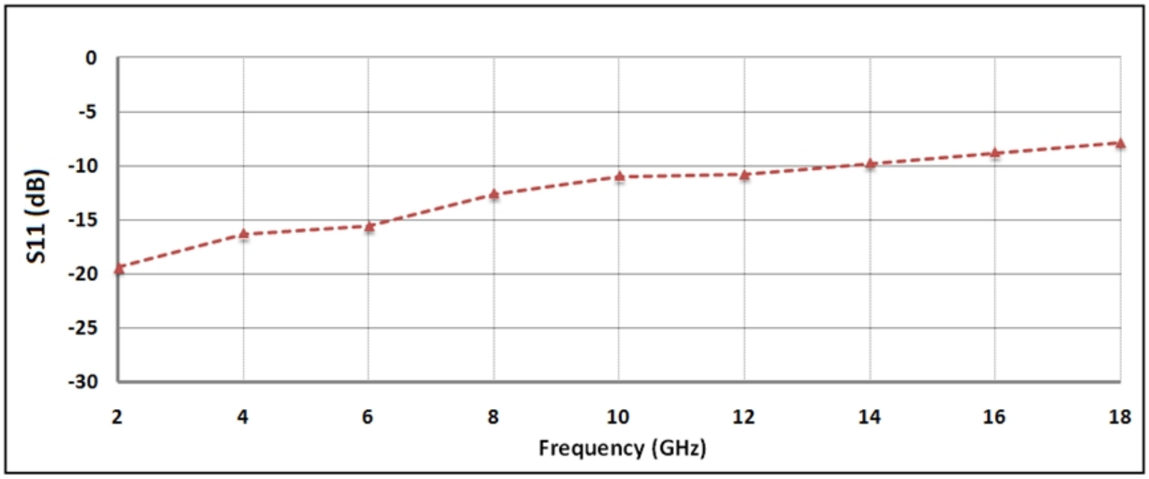

Figure 4-10: S11 (dB) vs. Frequency (GHz)

4.3 Concluding Remarks

The fabricated antenna patterns demonstrate that the simulation patterns obtained from theoretical design translate considerably well to practice. A modified slow-wave Archimedean spiral antenna demonstrates excellent axial ratio performance across the bandwidth. We were also able to maintain a uniform high gain over its frequency of operation using a shallow optimized cavity developed in our earlier work. For applications where antenna aperture size and weight are important factors, these wideband antennas can prove to be extremely useful.

Chapter 5

Cavity-backed Elliptical and Square Spiral Antennas

In our study of spiral antennas of various configurations, in this chapter, we first present two-arm elliptical spirals for beamwidth regulation. We then proceed on to analyzing the radiation properties of rectangular spirals backed with low-profile cavities.

5.1 Two-arm Elliptical Spiral Antennas

One of the spiral antenna models we have investigated is a cavity-backed two-arm elliptical spiral antenna. We varied the ratio of the major axis to the minor axis of the elliptical structure and observed changes in the radiation pattern. By using an elliptical spiral antenna, we were able to regulate the beam-width in two orthogonal planes, $\Phi = 0^\circ$ and $\Phi = 90^\circ$. Figure 5-1 shows the antenna geometry and an example of the difference in beam-widths in the principal planes when using an elliptical structure.

Using an elliptical structure compromises the purity of circular polarization to some extent in the lower frequencies. However, the configuration has the ability to control the beam-width in orthogonal planes and this attribute can be useful in many

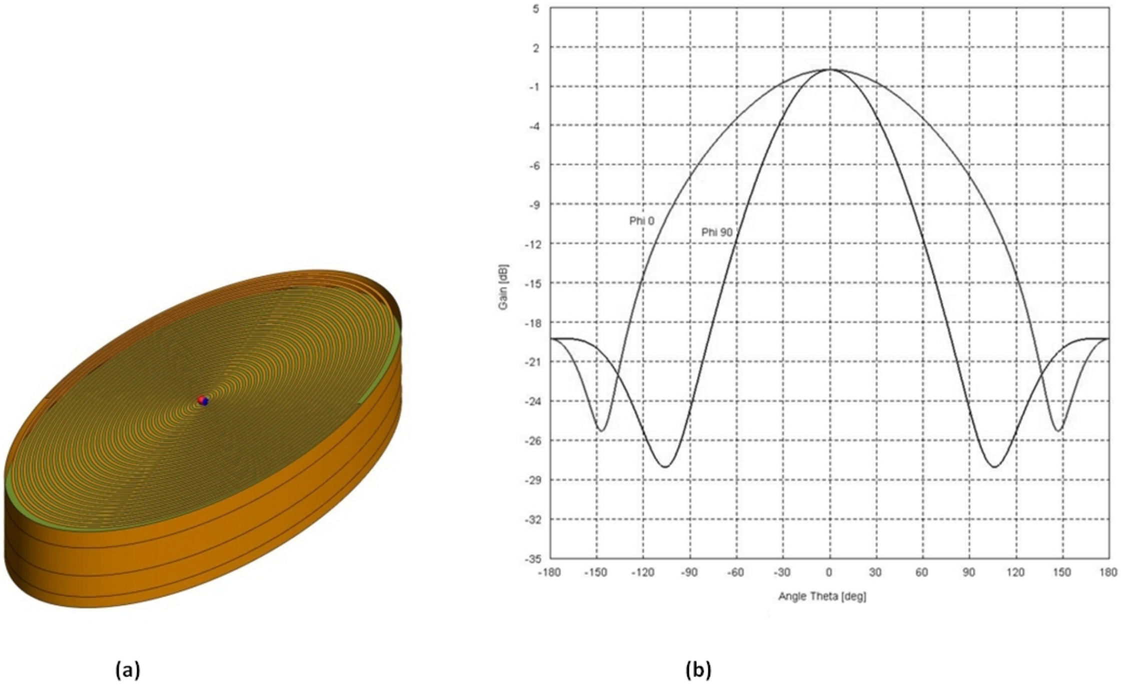

Figure 5-1: (a) 2-arm Archimedean elliptical spiral antenna (b) Sample plot of gain (db) vs. angle at 2 GHz for both $\Phi = 0^\circ$ and $\Phi = 90^\circ$ principal planes

ways. The half-power beam-width of an antenna is a measure of the angular extent of the most powerful portion of the radiated energy. Focusing the antenna beam in certain directions distributes more power towards those directions and allows for efficient power distribution depending on intended areas or angles of coverage. In high traffic areas, it is often useful to radiate stronger signals in desired directions while minimizing signal transmission towards others. This property can be achieved by designing antennas such that their beam-widths are tunable in preferred directions.

Moreover, a receiving antenna is only able to distinguish between two transmitting stations if one station's angular position is within the beam-width and the other station lies outside. This means that if the angular distance between two transmitting stations is at least equal to or greater than the beam-width, the receiving antenna is able to successfully resolve both. Therefore, as the beam-width decreases, the resolution becomes higher and a correct number of targets can be accurately resolved. The directivity of the antenna also increases with decreasing beam-width.

Narrow beams are less prone to artifact ambiguity in the main beam. However, narrower beams have greater sidelobe radiation and ambiguities may arise if artifacts are present in the side-lobe. Beam-width is also one of the most important factors that decide the degree of interference to the signal received during a solar outrage. Narrower beam-widths generally offer high signal-to-noise ratios.

5.1.1 Antenna Geometry

We have simulated three antenna models, with major axis-to-minor axis ratios of 1.5:1, 2:1 and 3:1 from 2-18 GHz and used the low-profile cavity configuration we have developed in our earlier work. The elliptical spirals were constructed by using parametric equations 5.1.

$$x = t\cos t,\ \ y = kt\sin t \tag{5.1}$$

where k is the ratio of the major axis to the minor axis of the elliptical spiral. The absorbing cavity has a similarly optimized configuration as that described in Chapter 2.

5.1.2 Results

The boresight gains for both principle planes of the antenna are shown in Table 5.1.

Table 5.1: BORESIGHT RHC AND LHC GAIN OF THREE ELLIPTICAL CONFIGURATIONS

f(GHz)	1.5:1		2:1		3:1	
	LHC	RHC	LHC	RHC	LHC	RHC
2	-8.646	1.025	-10.892	1.669	-5.38	1.91
4	-12.877	4.047	-14.96	3.703	-13.76	3.7
6	-22.065	3.322	-18.429	2.865	-18.78	-1.2
8	-18.438	4.652	-14.084	6.015	-9.69	3.22
10	-26.175	4.168	-30.5	2.937	-17.23	4.78
12	-18.196	4.773	-10.175	5.284	-17.35	2.74
14	-17.137	5.917	-10.692	5.889	-21.42	-6.1
16	-19.9	6.118	-15.199	4.421	-6.82	5.38
18	-15.598	4.846	-12.088	0.951	-12.33	-0.96

Throughout the operational band, co-polarized gain values were maintained above

3dB for the most part, while cross-polarized gains were lower than -10 dB. Table 5.2, Table 5.3 and Table 5.4 summarizes the -3dB beam-width in planes $\phi = 0°$ and $\phi = 90°$, boresight axial ratio, S_{11} and VSWR for 1.5:1, 2:1 and 3:1 configuration of the elliptical models. Our results show that while the boresight gain remains the same, the -3dB beam-width is different for principal planes. The axial ratio performance has been compromised due to the use of an elliptical structure, which is expected (and self-evident) from the antenna geometry. Higher ratios of the major axis to minor axis demonstrates lower axial ratio performance. For instance, the axial ratio is $\leq 3dB$ for the most part in a 1.5:1 configuration elliptical structure, and starts deteriorating as the ratio becomes larger in 2:1 or 3:1 configurations.

Table 5.2: 3 dB BEAM-WIDTH(DEGREES), AXIAL RATIO, S11, AND VSWR OF 1.5:1 CONFIGURATION

f(GHz)	Beamwidth		AR(dB)	S11(dB)	VSWR
	Phi=0	Phi=90			
2	98	80	1.57	-7.25	2.54
4	82	64	3.55	-13.05	1.99
6	66	84	1.1	-7.37	3.05
8	74	52	1.22	-5.25	3.6
10	72	88	0.98	-16.45	1.79
12	90	60	0.748	-4.9	3.89
14	88	56	0.512	-17.8	2.03
16	96	66	1.22	-27.06	1.28
18	74	108	0.748	-8.75	2.5

Figure 5-2, 5-3 and 5-4 shows the polar gain plots at 2 GHz, mid-band 10 GHz and 18 GHz for both $\phi = 0°$ and $\phi = 90°$ principal planes for all three configurations.

Our results show that an elliptical spiral demonstrates comparable gain performance as its circular counterpart. In addition, it allows for regulation of power distribution or 3 dB beamwidth in two orthogonal planes.

For overall gain and bandwidth characteristics, the 2:1 ratio elliptical spiral antenna demonstrated the best radiation performance in our study [37].

Table 5.3: 3 dB BEAM-WIDTH(DEGREES), AXIAL RATIO, S11, AND VSWR OF 2:1 CONFIGURATION

f(GHz)	Beamwidth		AR(dB)	S11(dB)	VSWR
	Phi=0	Phi=90			
2	101.94	74	3.538	-5.31	3.4
4	83.4	48	4.349	-12.9	1.57
6	69.32	72	2.958	-3.2	5.66
8	76.6	80	2.843	-11.11	3.22
10	92.6	56	2.495	-4.23	5.93
12	93.4	102	2.031	-12.86	1.59
14	87.4	36	1.799	-10.13	3.09
16	80.4	38	2.147	-3.61	5.29
18	77.4	114	3.306	-3.2	5.57

Table 5.4: 3 dB BEAM-WIDTH(DEGREES), AXIAL RATIO, S11, AND VSWR OF 3:1 CONFIGURATION

f(GHz)	Beamwidth		AR(dB)	S11(dB)	VSWR
	Phi=0	Phi=90			
2	104	62	8.14	-15.06	2.6
4	86	44	2.27	-4.72	3.77
6	76	104	2.15	-5.35	7.96
8	78	74	3.95	-9.72	5.6
10	82	36	1.32	-14.85	4.85
12	76	42	1.8	-1.84	10.45
14	80	134	2.75	-2.07	11.54
16	84	26	4.28	-8.78	5.53
18	74	136	4.67	-14.26	4.57

1.5:1 Configuration:

2 GHz:

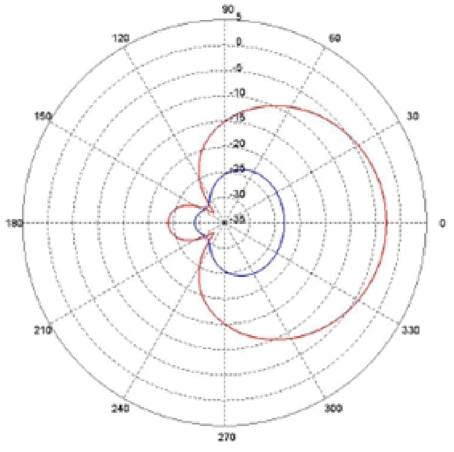

Phi = 0° **Phi = 90°**

10 GHz:

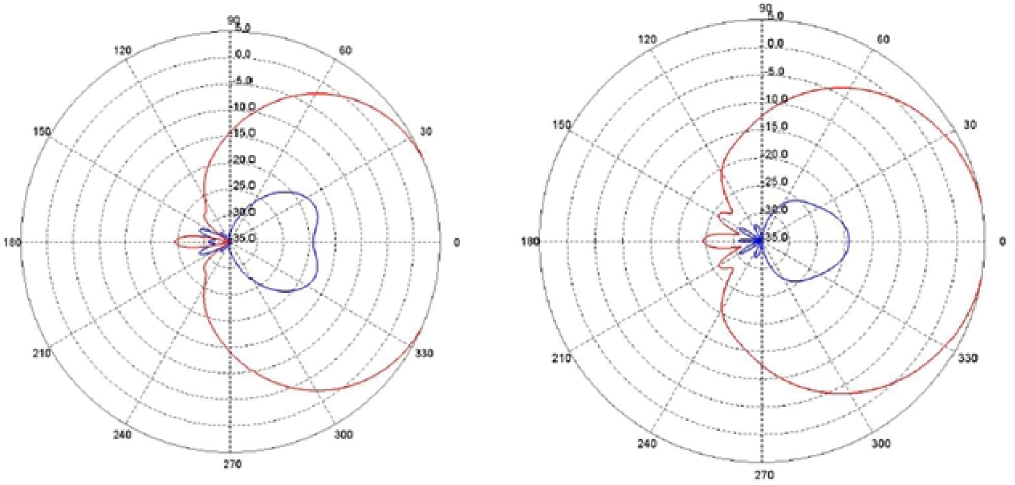

Phi = 0° **Phi = 90°**

18 GHz:

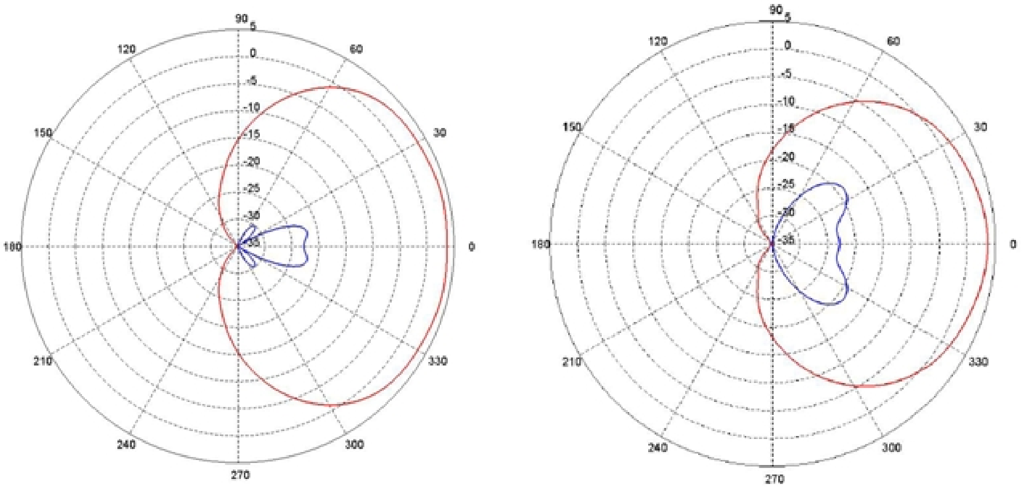

Phi = 0° **Phi = 90°**

Figure 5-2: (Gain at $\Phi = 0°$ and $\Phi = 90°$ principal planes for 1.5:1 configuration

2:1 Configuration:

2 GHz:

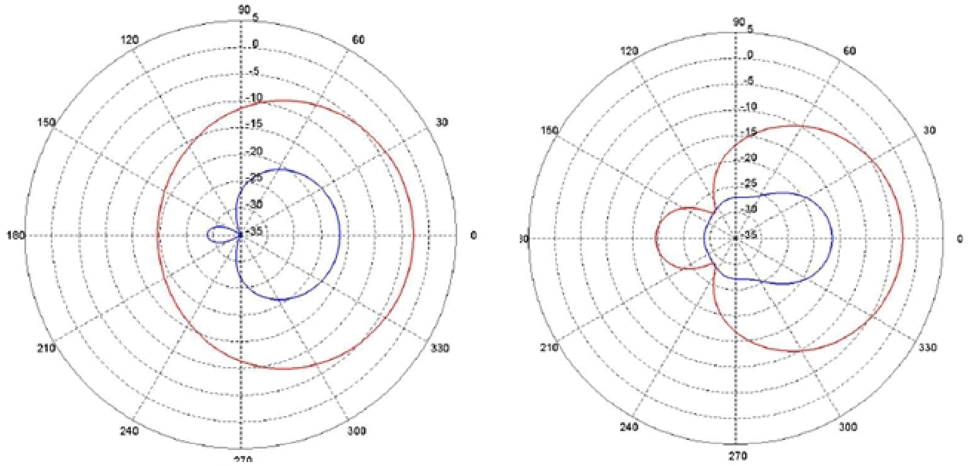

Phi = 0° **Phi = 90°**

10 GHz:

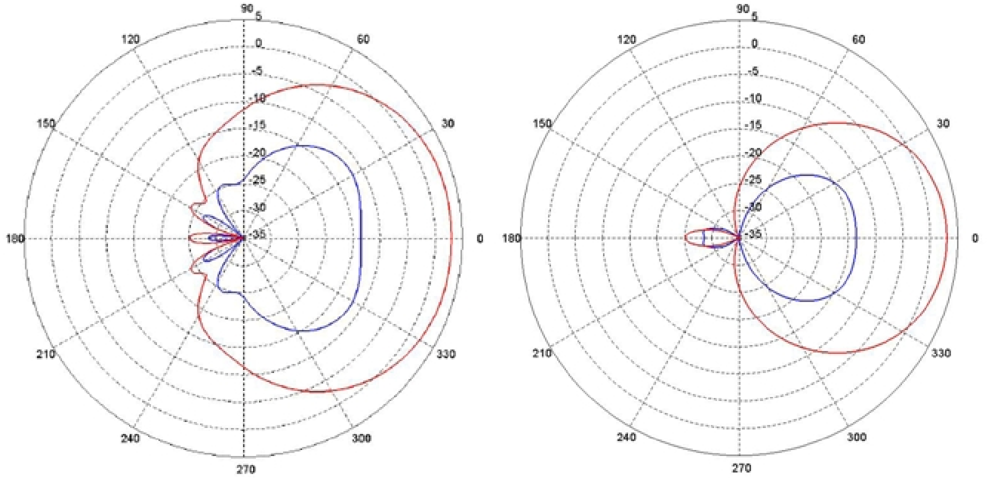

Phi = 0° **Phi = 90°**

18 GHz:

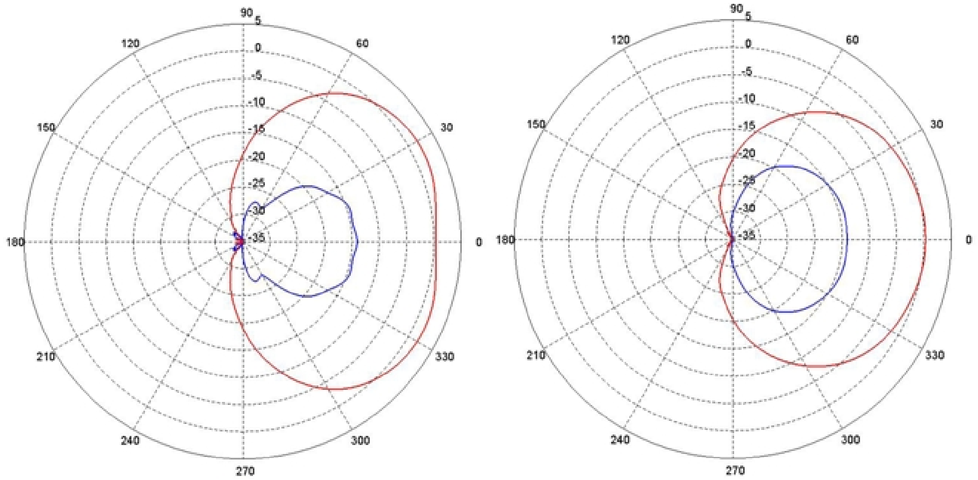

Phi = 0° **Phi = 90°**

Figure 5-3: Gain at $\Phi = 0^\circ$ and $\Phi = 90^\circ$ principal planes for 2:1 configuration

3:1 Configuration:

2 GHz:

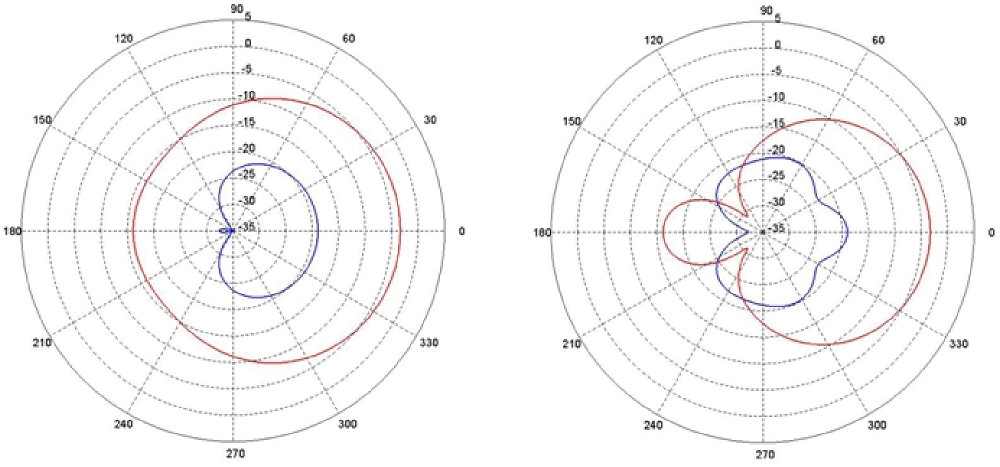

Phi = 0° **Phi = 90°**

10 GHz:

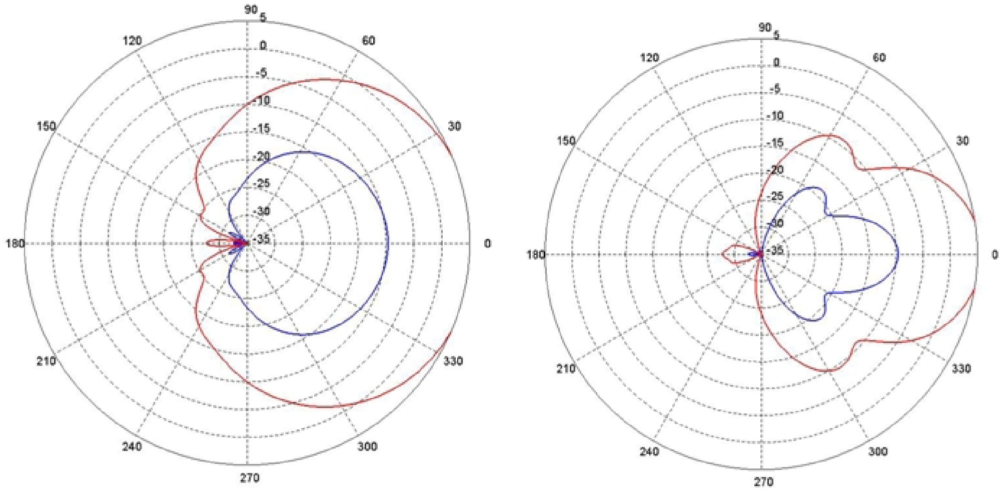

Phi = 0° **Phi = 90°**

18 GHz:

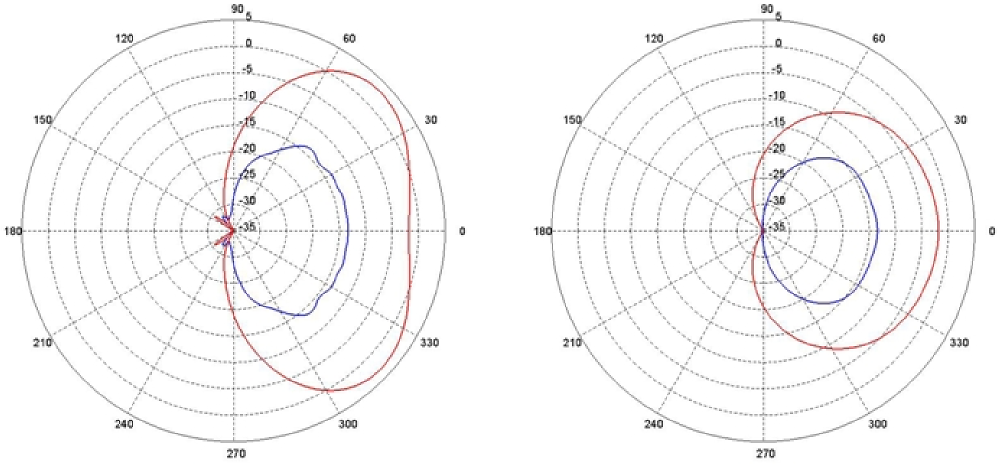

Phi = 0° **Phi = 90°**

Figure 5-4: Gain at $\Phi = 0^\circ$ and $\Phi = 90^\circ$ principal planes for 3:1 configuration

5.2 Two-arm Square Spiral Antennas

A square spiral antenna operates in a similar mechanism as its circular spiral counterpart as explained by the current band theory. However, square spirals have the advantage of operating with comparable gain-bandwidth performance at lower frequencies than corresponnding circular spirals of same diameter. This is because in accordance with the current band theory, the first radiation band of a spiral antenna occurs when the circumference of the spiral is one current-wavelength at the operating frequency [19]. One current wavelength corresponds to diameter $D = \frac{\lambda_e}{\pi}$ for the circular case and a width of $W = \frac{\lambda_e}{4}$ for the rectangular case, where λ_e is the effective wavelength or current-wavelength. Therefore, the first operating frequency is approximately 22% lower for a square spiral than that of a circular one when they both have the same diameter. The longer circumference of square spirals allow them to be packaged closer together than circular spirals in an array configuration when constrained to the same space or whenever a square mounting footprint is required [10, 31].

In this section, we consider the radiation properties of cavity-backed square spiral antennas from 2-18 GHz.

5.2.1 Antenna Geometry

We designed a two-arm square spiral antennna with 20 turns in each arm. The diamater of the cavity is 2.025 inches and the depth of the cavity is 0.691 inches with similar constituents and thickness of absorbing materials used in our previous work. The air-gap between absorbing layers and antenna is 0.178 inches, the thickness of front layer AN absorber is 0.2532 inches, the middle layer (LS-10055 absorber, ARC technology) thickness is 0.1908 inches and metal-backed third layer (WT-BPJA-010, ARC technology) is 0.09879 inches. The antenna model is shown in Figure 5-5.

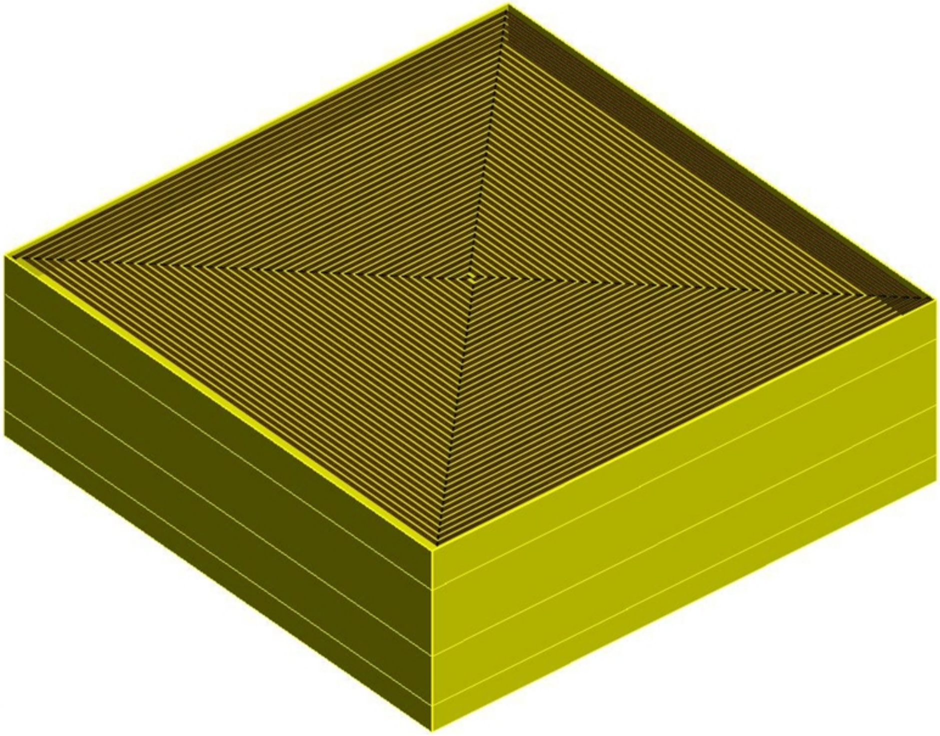

Figure 5-5: Cavity-backed, Two-arm, Square Spiral Antenna

5.2.2 Results

The full-wave analysis of a cavity-backed square spiral antenna has been carried out with method-of-moments (MoM) based FEKO. Figures 5-6, 5-7 and 5-8 shows the polar plots for co-polarized RHCP gain and the cross-polarized LHCP gain for all frequency points at 2 GHz intervals for a 2-18 GHz antenna.

Table 5.5 summarizes the gain, axial ratio, S_{11}, VSWR and input impdance performance of the square spiral antenna.

5.2.3 Discussion

The square spiral antenna demonstrates considerably comparable gain performance as circular spiral antennas. However, from the axial ratio values, we can observe that the antenna shows $\geq 3dB$ axial ratios for most of its bandwidth. This phenomenon can be atributed to the fact that sharp discontinuities exist at the corners of each turn resulting in current standing waves that significantly deteriorates the axial ratio.

Table 5.5: BORESIGHT RHC GAIN, LHC GAIN, AXIAL RATIO, S11, VSWR AND INPUT IMPEDANCE A REGULAR SQUARE SPIRAL ANTENNA WITH A SHALLOW CAVITY

f(GHz)	Gain (dB)		AR(dB)	S11(dB)	VSWR	Impedance Ω
	RHC	LHC				
2	-1.54	-18.1	2.59	-28.1	1.17	201
4	3.23	-13.3	2.6	-25.8	1.23	208
6	5.53	-8.97	3.31	-28.4	1.16	203
8	6.23	-5.11	4.83	-22.6	1.35	204
10	5.51	-5.63	4.95	-23.9	1.29	211
12	4.19	-5.36	6.01	-24.9	1.26	207
14	5.05	-4.73	5.85	-21	1.43	214
16	5.84	-3.86	5.9	-18.9	1.58	219
18	4.82	-7.04	4.53	-18	1.66	221

In order to reduce the current standing waves in the spiral arms, we designed a square spiral with rounded ends to allow for a smoother transition in the arms. The resulting 20 turn smooth square spiral model is shown in Figure 5-9 in comparison with a regular square spiral model.

Table 5.6 summarizes the gain and axial ratio performance of a regular square spiral antenna and a square spiral antenna with smooth corners.

Table 5.6: BORESIGHT RHC AND LHC GAIN AND AXIAL RATIO COMPARISON OF REGULAR SQUARE AND SMOOTH SQUARE SPIRAL ANTENNA

f(GHz)	Gain (dB)				AR(dB)	
	RHC		LHC			
	Reg.	Smooth	Reg.	Smooth	Reg.	Smooth
2	-0.664	4.55	-2.87	-17.5	18	1.38
4	3.89	5.80	-17.8	-5.43	1.43	4.9
6	4.63	5.32	-11	-5.97	2.89	4.86
8	5.14	5.63	-6.08	-7.76	4.9	3.78
10	5.03	4.67	-5.18	-7.41	5.54	4.42
12	5.72	4.70	-5.06	-9.42	5.17	3.46
14	5.02	5.31	-4.84	-3.64	5.79	6.48
16	4.21	4.29	-5.11	-3.94	6.19	7.11
18	4.67	4.36	-4.31	-4.16	6.47	6.85

Our results show that this approach, makes no significant improvement on the axial ratio of the 2-18 GHz square spiral antennas and the demonstrates similar axial ratio performance ≥ 4 dB in both cases. The radiation characteristics obtained from our investigation leads us to conclude that regular square spirals, despite having substantially comparable gain performance and compact apertures as that of their circular counterparts, generally suffer from reduced axial ratio performance.

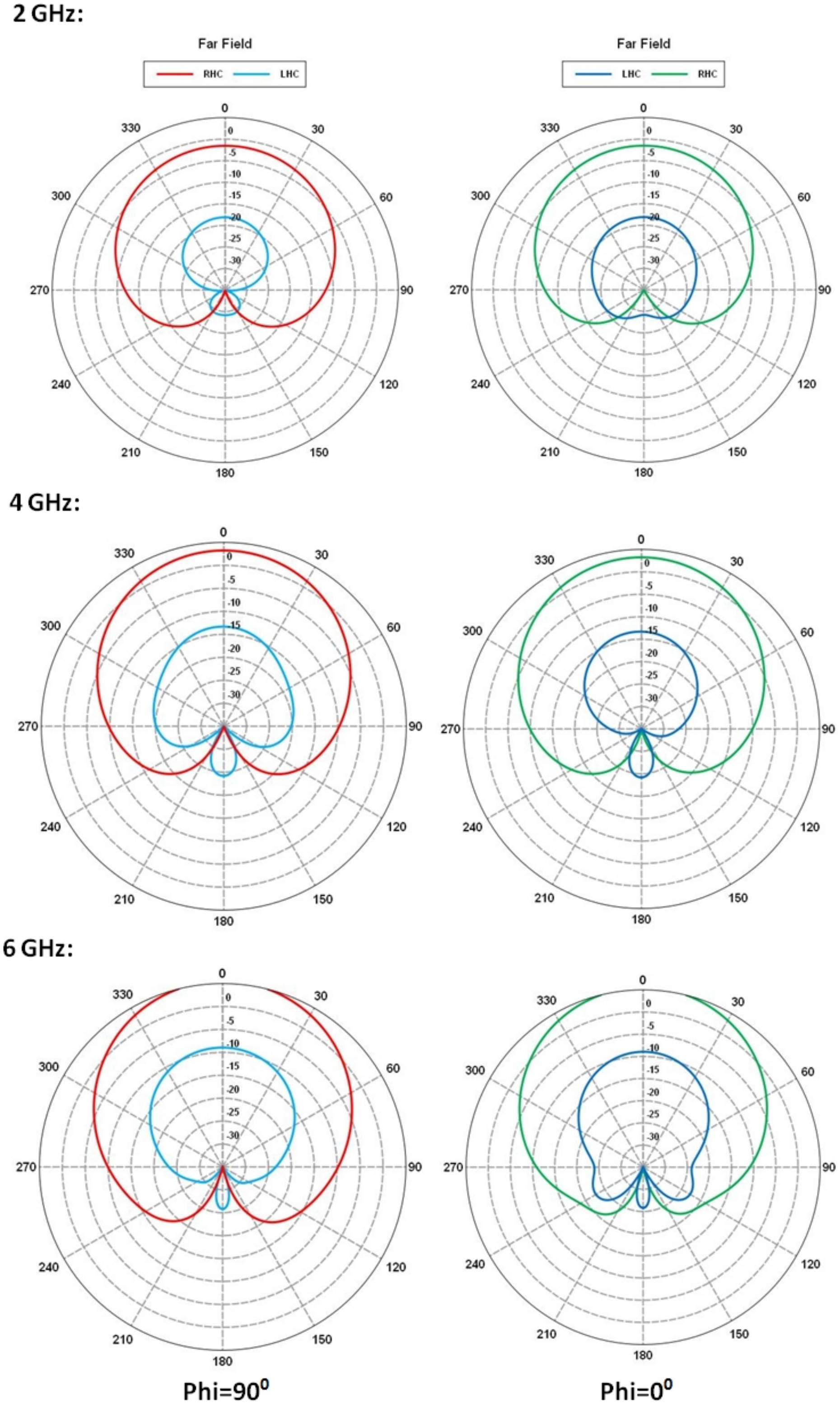

Figure 5-6: Gain at $\Phi = 0^\circ$ and $\Phi = 90^\circ$ principal planes for 2, 4 and 6 GHz

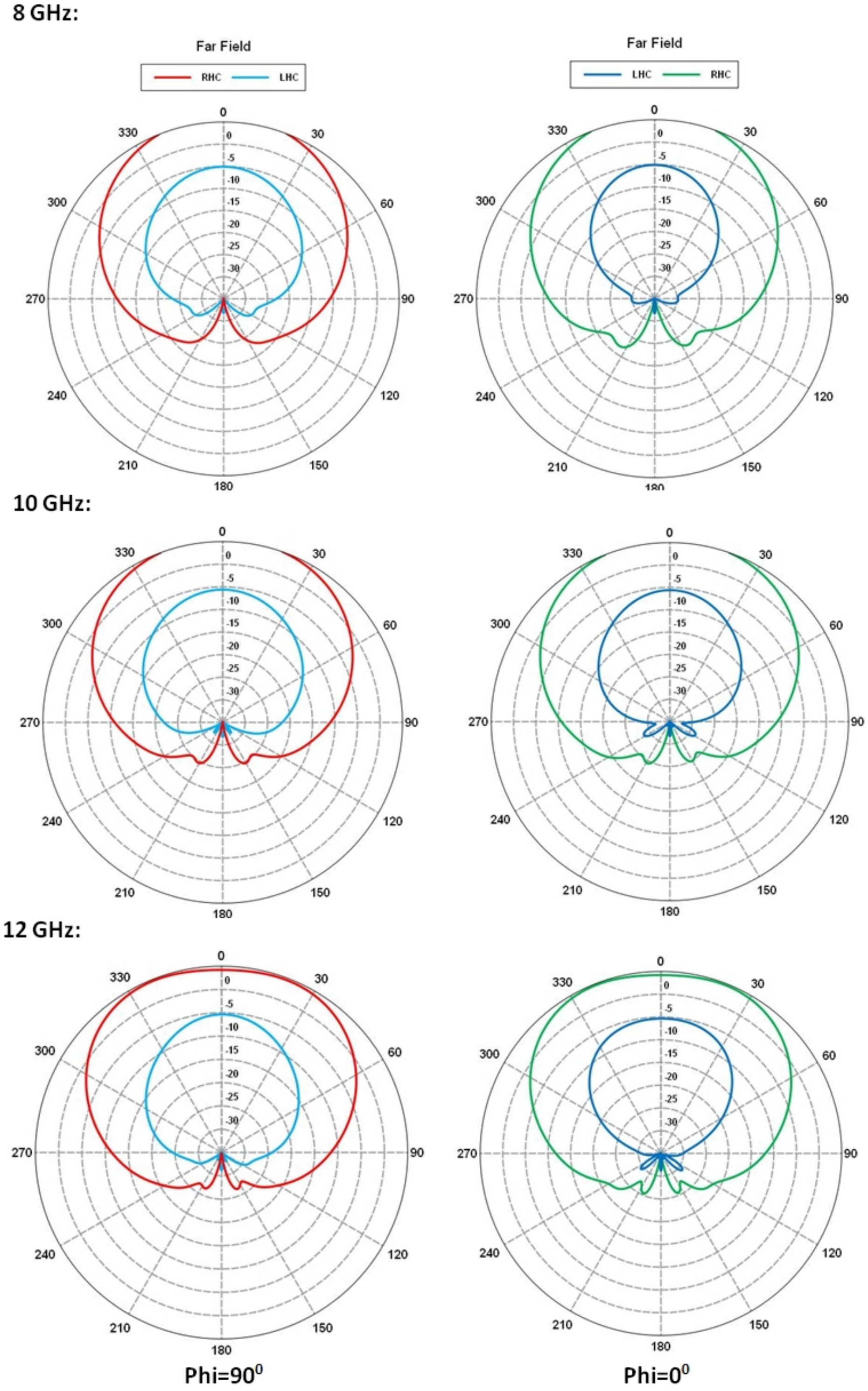

Figure 5-7: Gain at $\Phi = 0^\circ$ and $\Phi = 90^\circ$ principal planes for 8, 10 and 12 GHz

14 GHz:

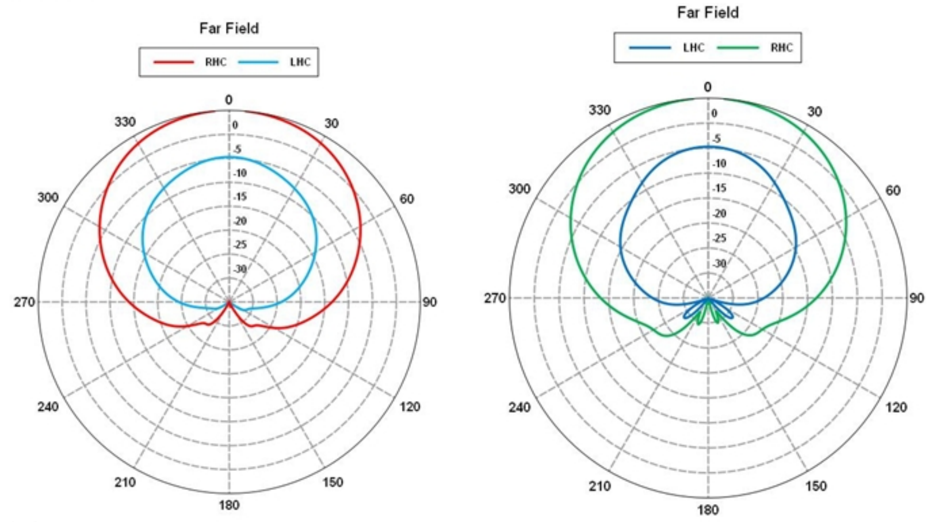

16 GHz:

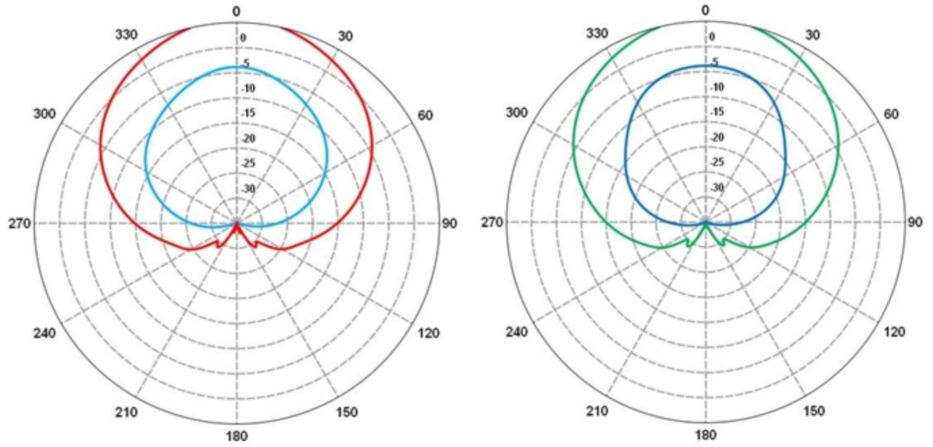

18 GHz:

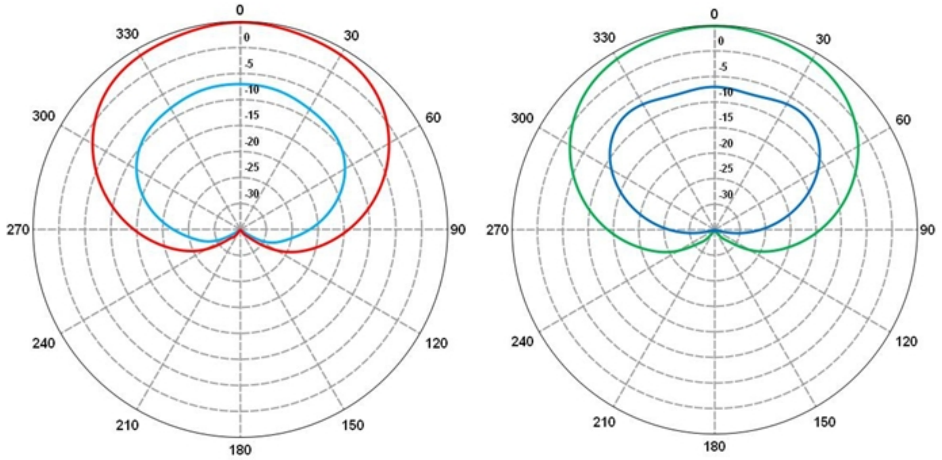

Phi=90^0 **Phi=0^0**

Figure 5-8: Gain at $\Phi = 0°$ and $\Phi = 90°$ principal planes for 14, 16 and 18 GHz

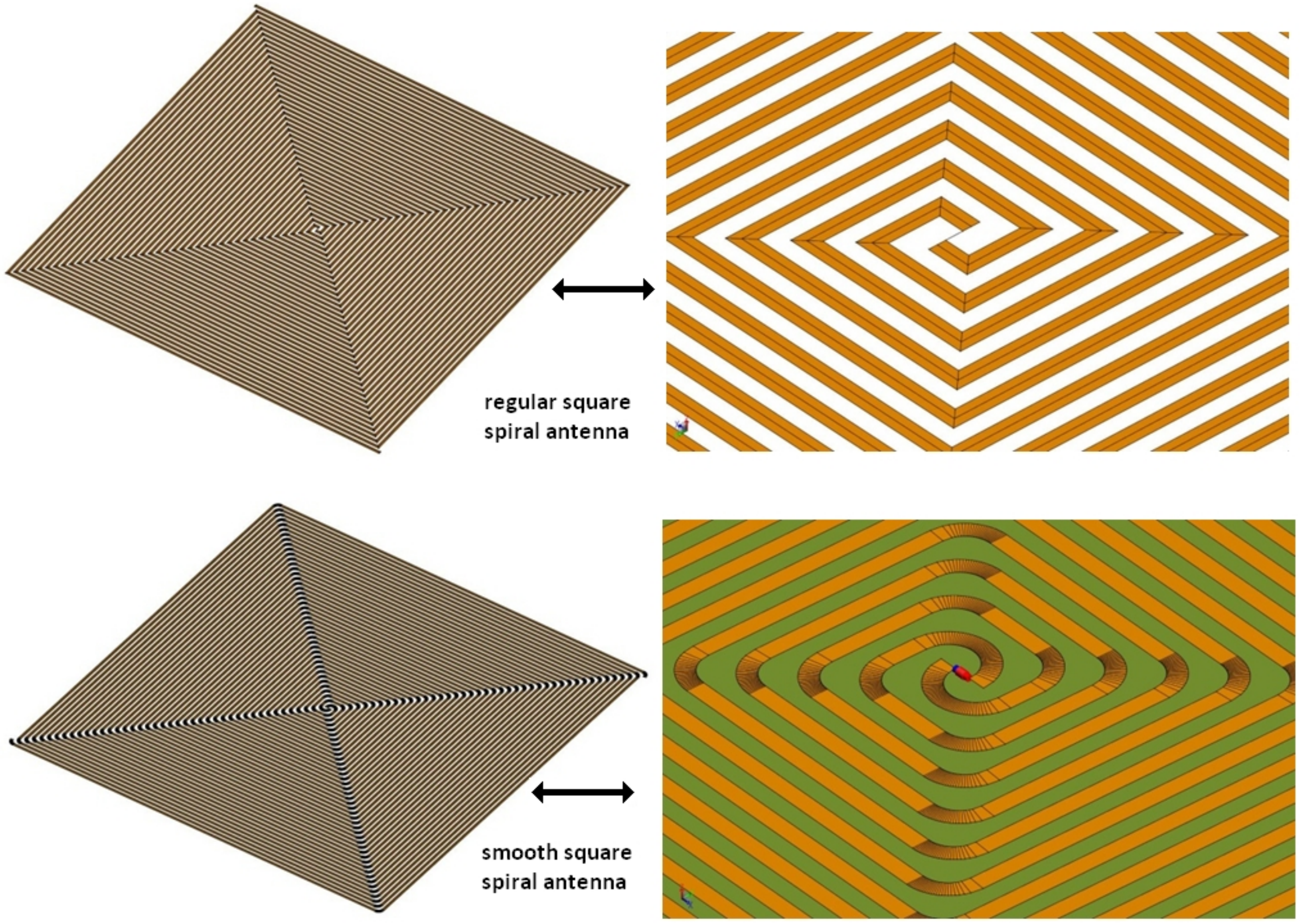

Figure 5-9: 20 turn, 2 arm, regular square and smooth square spiral antenna

Chapter 6

The Polygonal Modified Archimedean Spiral Antenna

Planar spiral antennas are most often designed to operate in primarily two configurations: the circular and the rectangular [28]. Based on the requirements of a specific application, both configurations have their advantages and disadvantages. Square spirals have the advantage of operating with the same performance at lower frequencies as that of their circular counterparts. The fundamental advantage of using spiral antenna systems, however, is the radiation of circularly polarized waves over ultra-wide bandwidths. Although square spirals allow for compact packaging, they often demonstrate irregular performance across the band and commonly have poor axial ratio performance compared to their circular Archimedean counterparts.

In this chapter, we present a novel 2-18 GHz polygonal modified Archimedean spiral antenna which approximates a circular Archimedean spiral in its high frequency operating region and a square spiral in its low-frequency zone. The polygonal antenna is backed with a shallow, hybrid, absorptive cavity described in chapter 3. The design has maintained ≤ 3 dB axial ratio for 93.75%-98% of its bandwidth while preserving the advantages of a square spiral antenna. 3 modifications to the original polygonal antenna are also presented here. The radiation patterns obtained from the proposed polygonal geometries are compared to that obtained from purely circular and square patterns having the same diameter and the significant improvement in axial ratio is demonstrated in the results. In all simulations, we have assumed matched conditions at the antenna input port and the excitation source impedance was set to 188 Ω in accordance with Babinet-Bookerś principle [6].

6.1 Polygonal Archimedean Spiral Antenna Model

In this novel design, we have demonstrated a 2-18 GHz modified polygonal Archimedean spiral antenna which approximates a circular spiral in its highest frequencies of operation and gradually transforms itself into a square spiral antenna at its lowest frequencies of operation.

6.1.1 Antenna Geometry

Number of turns and Segments

The spiral antenna is a 2-arm, 16 turn polygonal structure. The number of sides in a similar set of turns within the spiral is always kept to be a power of 2. Each spiral antenna arm consists of 4 innermost turns with 32 sides (2^5 sides), the next 4 turns with 16 sides (2^4 sides), the next 4 turns with 8 sides (2^3 sides) and the outermost 4 turns with 4 sides (2^2 sides).

The general idea is that a symmetrical polygon with 2^n sides can be created by truncating the corners and partial edges of a polygon with 2^{n-1} sides as demonstrated in Figure 6-1.

Since the number of edges is always held to be a power of 2, it becomes convenient to construct a symmetrical spiral antenna geometry with n being any positive integer depending the specific application and frequency of operation.

In order to create a particular polygonal turn, the angle of rotation to create the sides were determined from 6.1, where $d\theta$ is the angle of rotation.

$$d\theta = \frac{2 \times \pi}{\#\ of\ sides} \tag{6.1}$$

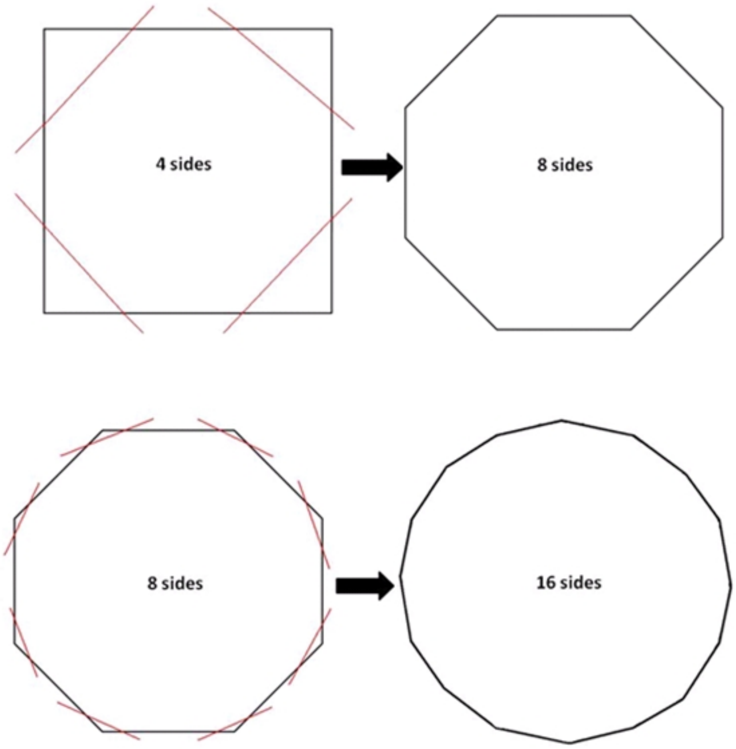

Figure 6-1: Construction of a 2^n -sided polygon from a 2^{n-1} -sided polygon

When making the transition from a 2^n side polygon to a 2^{n-1}-sided polygon, we can choose to make either the flat sides of different polygons parallel to each other or make the corners of an inner set of polygons line up with the centers of an outer set of polygons. The former reduces the irregularity in the transition from 2^n side polygon to 2^{n-1}-sided polygon and preserves best the self-complementary form of a two-arm spiral. Hence, to ensure a symmetric spiral polygonal structure, with regular transitions from 2^n to 2^{n-1}-sides, the flat sides are designed parallel and centered about the next larger set of sides. The resultant curve for one arm of the initial model of a spiral presented in this work is shown in Figure 6-2.

Modification of Archimedean Spiral

The Archimedean spiral curve is defined by the polar equation $r = a \times \theta$, where, $\theta \geq 0$. The system of parametric equations corresponding to the polar curve is: $x = a\theta \cos\theta$ and $y = a\theta \sin\theta$, where a is any real number denoting the growth rate of the spiral.

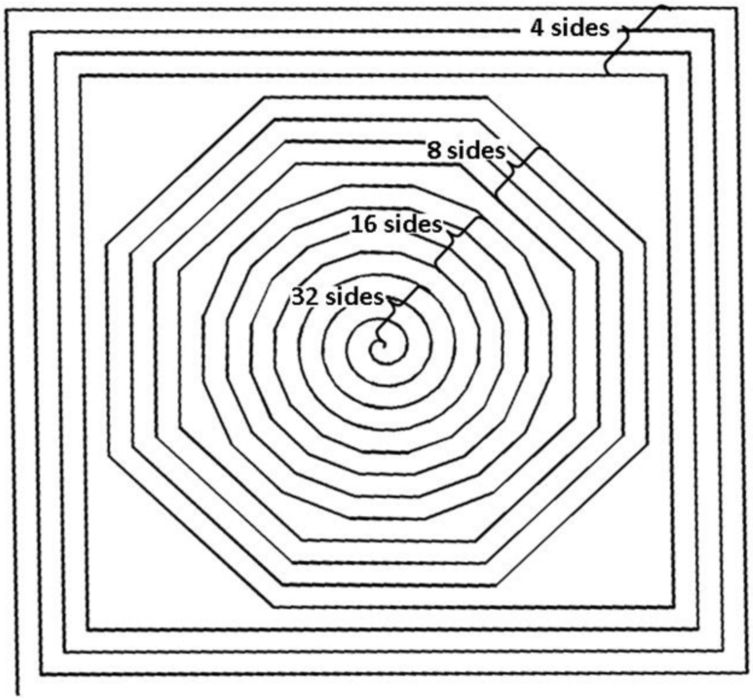

Figure 6-2: Geometry of the polygonal spiral arm

For the polygonal spiral case, when we increase the angle $d\theta$ to construct a next set of polygons with half the number of sides of the previous set, if the radius is not appropriately adjusted, the inner polygons will intersect with the outer polygons at some distance along the curve. To correct for the distance between adjacent sides and to ensure that the flat portion of the next turn of the spiral does not come any nearer than the vertex of the previous side, the parametric equations of the Archimedean spiral were modified as 6.2.

$$\begin{aligned} r' &= \frac{a \times \theta}{\cos\left(\dfrac{\theta}{2}\right)} \\ x &= r' \cos\theta \\ y &= r' \sin\theta \end{aligned} \tag{6.2}$$

In this way, since $\cos\left(\dfrac{d\theta}{2}\right) \leq 1$, the radius r' is modified to be slightly larger than the true Archimedean spiral radius r as shown in Figure 6-3. The new radius r'

intersects a line tangent to the point r on a true Archimedean spiral.

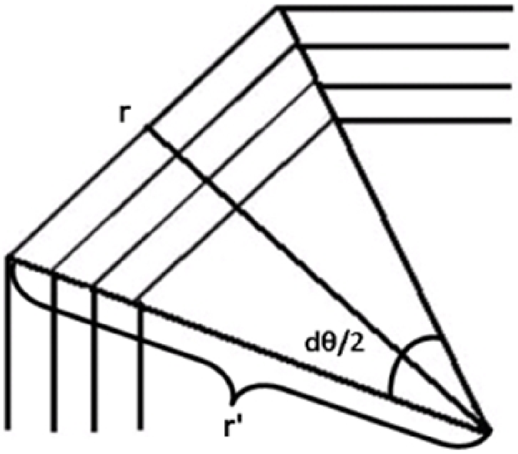

Figure 6-3: Modification of Archimedean spiral

The fabricated model of the cavity-backed initial polygonal antenna having 2 inch diameter is shown in Figure 6-4. The computer code used to generate the spiral curve is included in Appendix A.

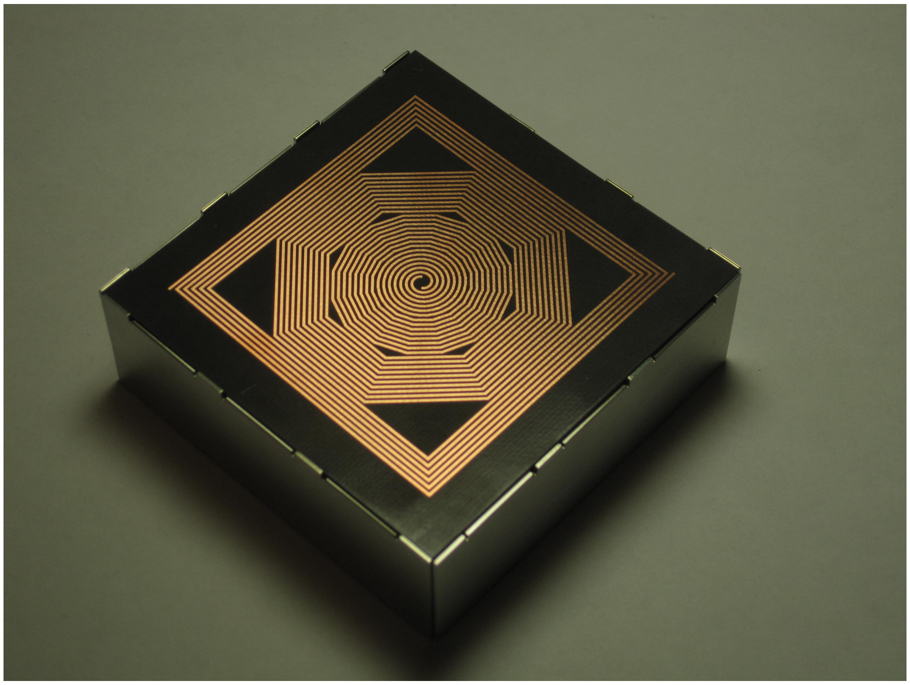

Figure 6-4: Modified polygonal Archimedean spiral antenna

6.1.2 Results

Gain

The full-wave analysis of a shallow cavity-backed modified Archimedean polygonal spiral antenna has been carried out with method-of-moments (MoM) based FEKO. Table The polar plots for gain (dB) for principal planes $\phi = 0°$ and $\phi = 90°$ and a diagonal cut $\phi = 45°$ are shown in Figures 6-5, 6-6, 6-7, 6-8, 6-9 and 6-10. The antenna demonstrates sufficiently high and stable gains, low sidelobes and no splits in the main beam across the bandwidth.

Axial Ratio

Figure 6-11 demonstrates the overall axial ratio performance for the original polygonal spiral antenna. The axial ratio remained $\leq$ 3dB for 93.75% of the 2-18 GHz bandwidth, which is a significant improvement over state-of-the-art UWB rectangular spiral antennas.

S11

Figure 6-12 shows the reflection coefficient at the antenna input port assuming matched conditions. The results show that the reflection coefficient is efficiently minimized to adequate levels across the bandwidth.

Input Impedance

Figure 6-13 shows the input impedance to the cavity-backed Archimedean spiral antenna. The antenna realizes a near constant input impedance structure over an ultra-wide bandwidth. The input impedance is sensitive to small geometrical variations and slight deviations from mean input impedance of 215Ω, which can be attributed to the polygonal structure of the antenna being not exactly self-complementary at the transition points from 2^n to 2^{n-1} sides.

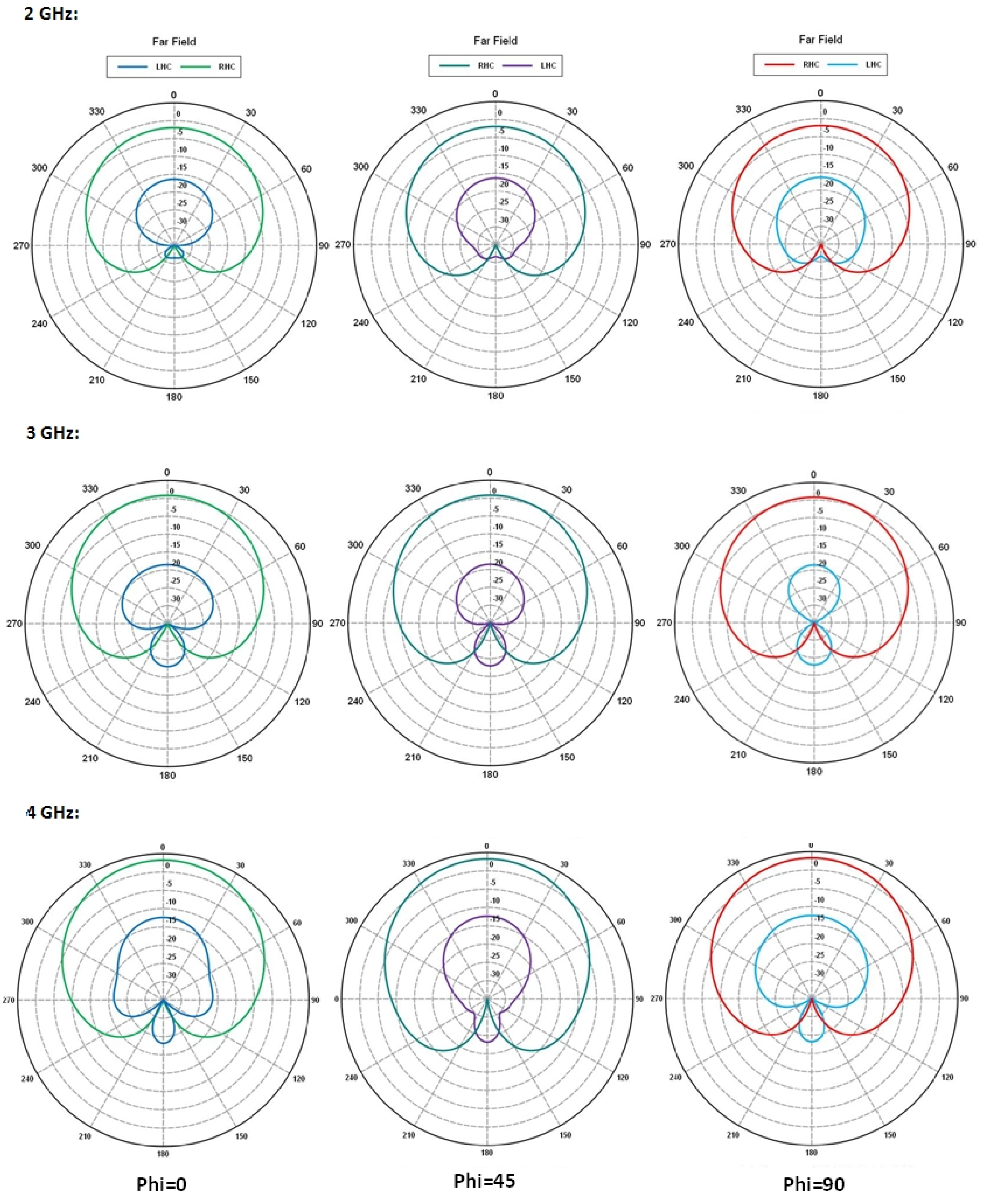

Figure 6-5: Gain (dB) for principal planes $\phi = 0°$, a diagonal cut $\phi = 45°$ and $\phi = 90°$ at 2, 3 and 4 GHz

5 GHz:

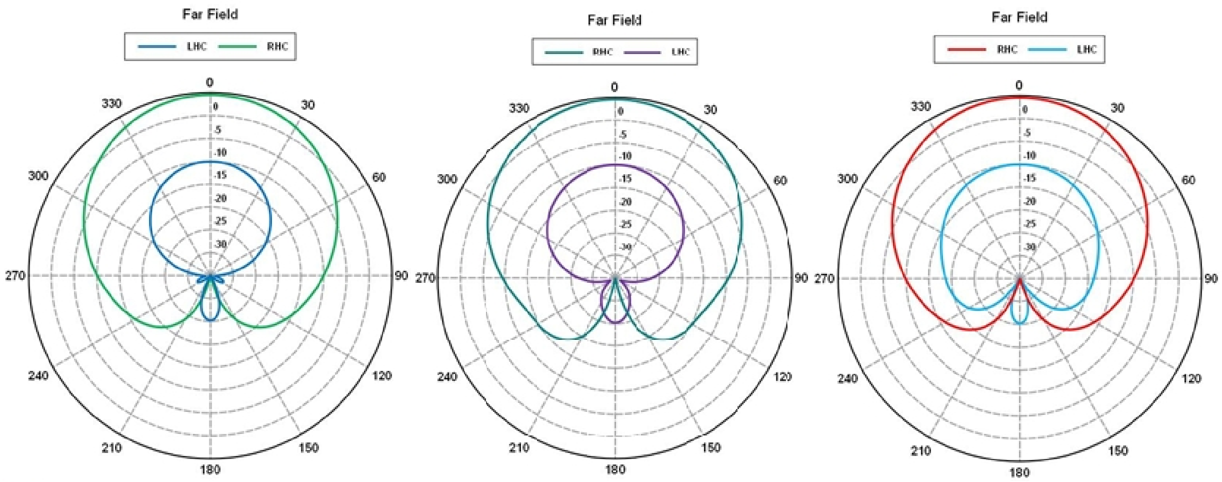

6 GHz:

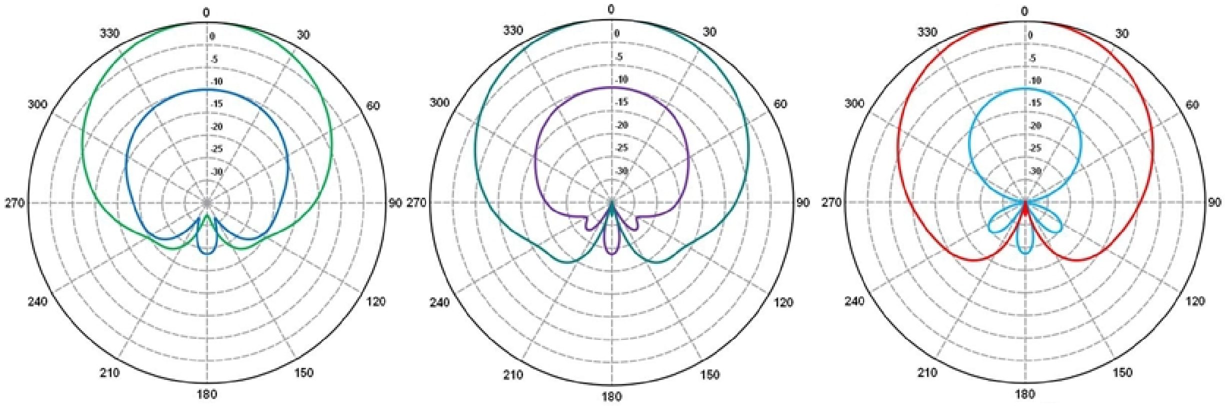

7 GHz:

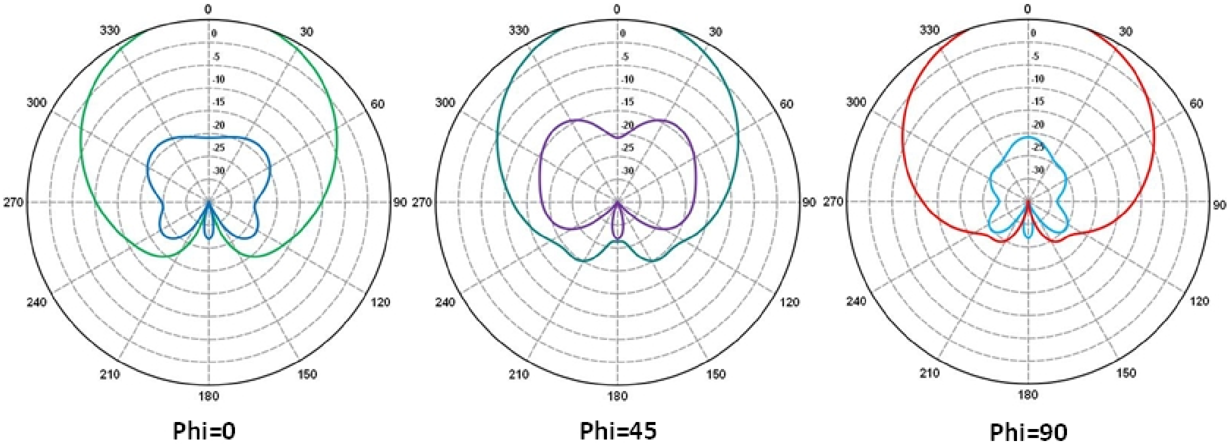

Figure 6-6: Gain (dB) for principal planes $\phi = 0°$, a diagonal cut $\phi = 45°$ and $\phi = 90°$ at 5, 6 and 7 GHz

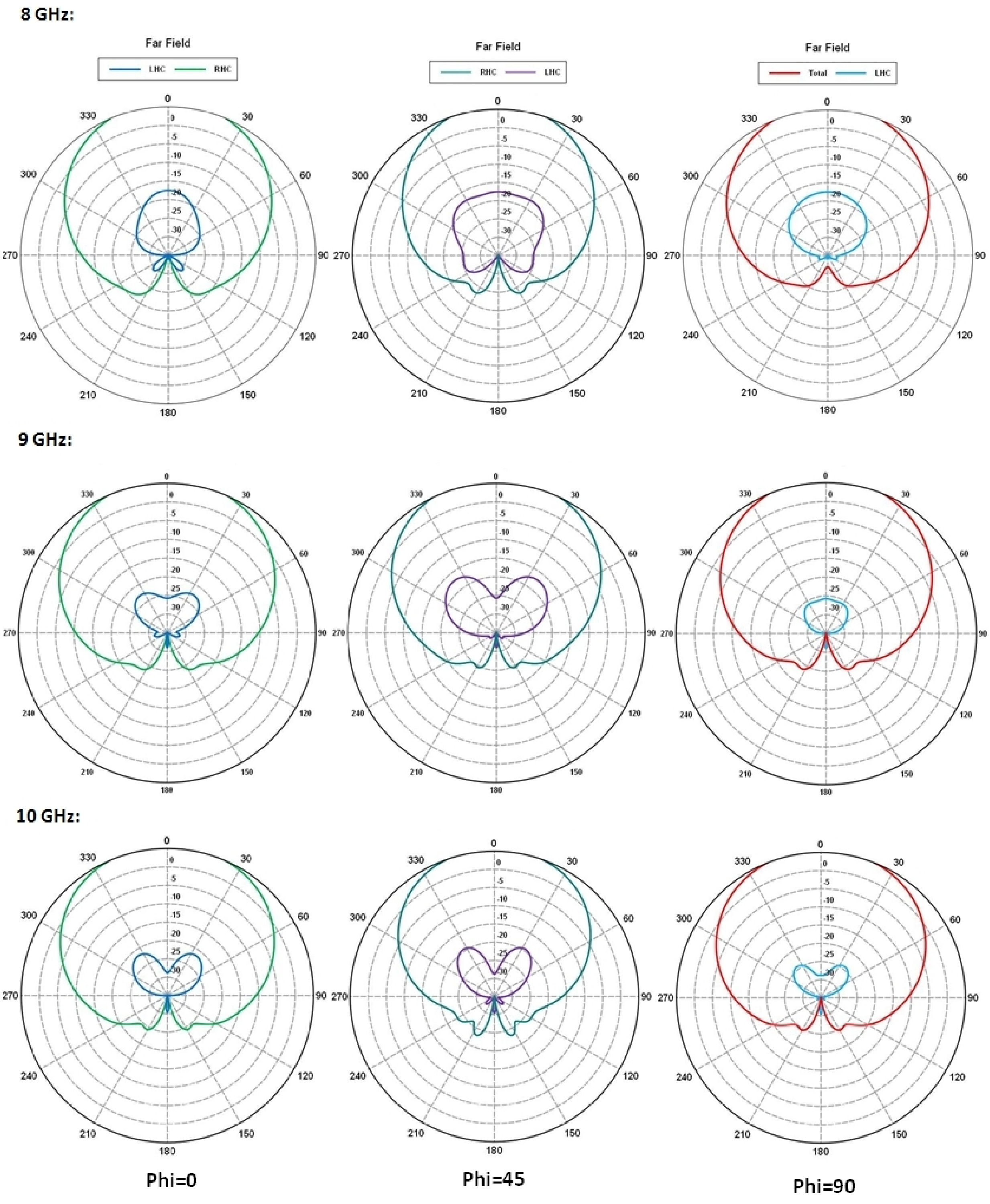

Figure 6-7: Gain (dB) for principal planes $\phi = 0°$, a diagonal cut $\phi = 45°$ and $\phi = 90°$ at 8, 9 and 10 GHz

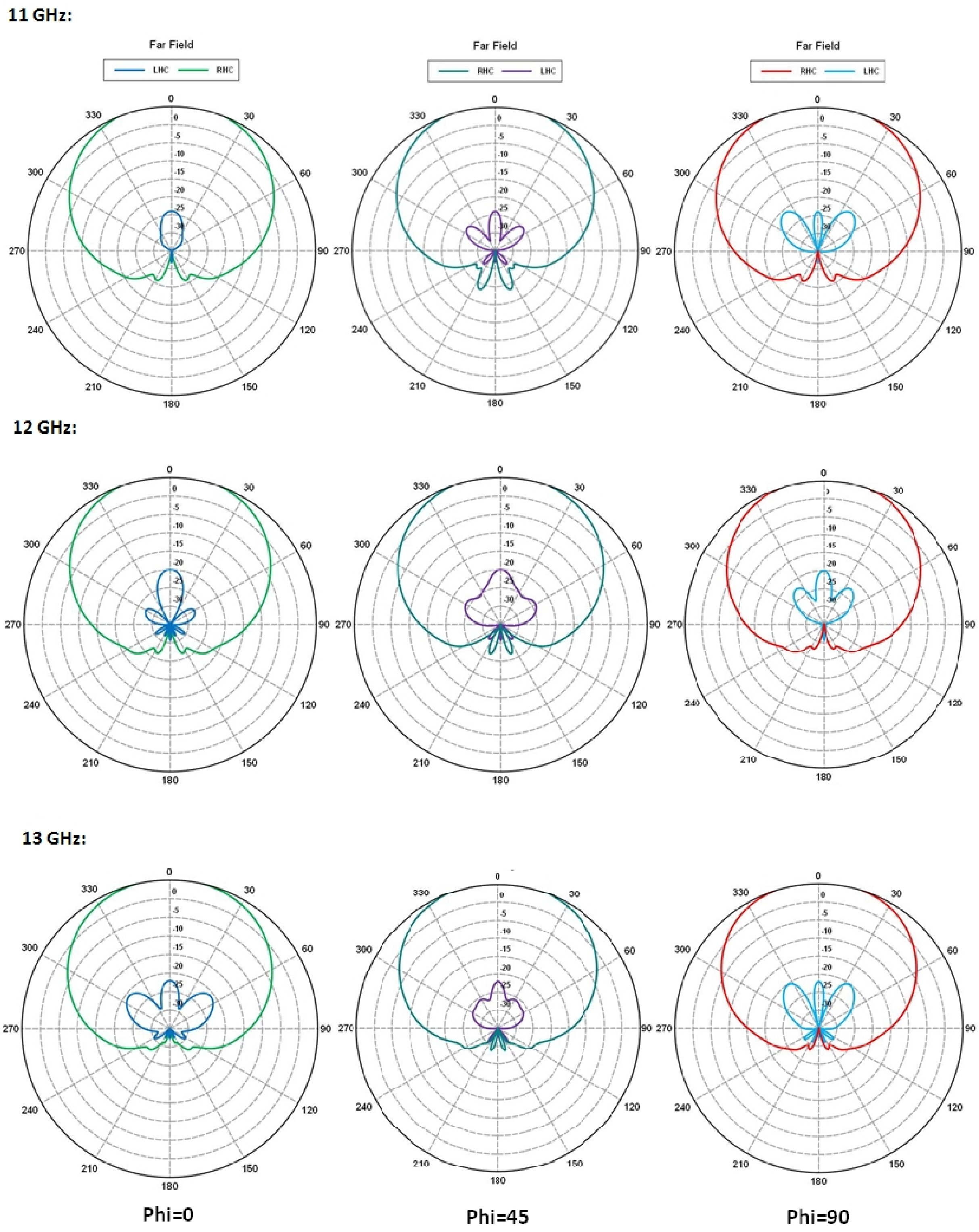

Figure 6-8: Gain (dB) for principal planes $\phi = 0°$, a diagonal cut $\phi = 45°$ and $\phi = 90°$ at 11, 12 and 13 GHz

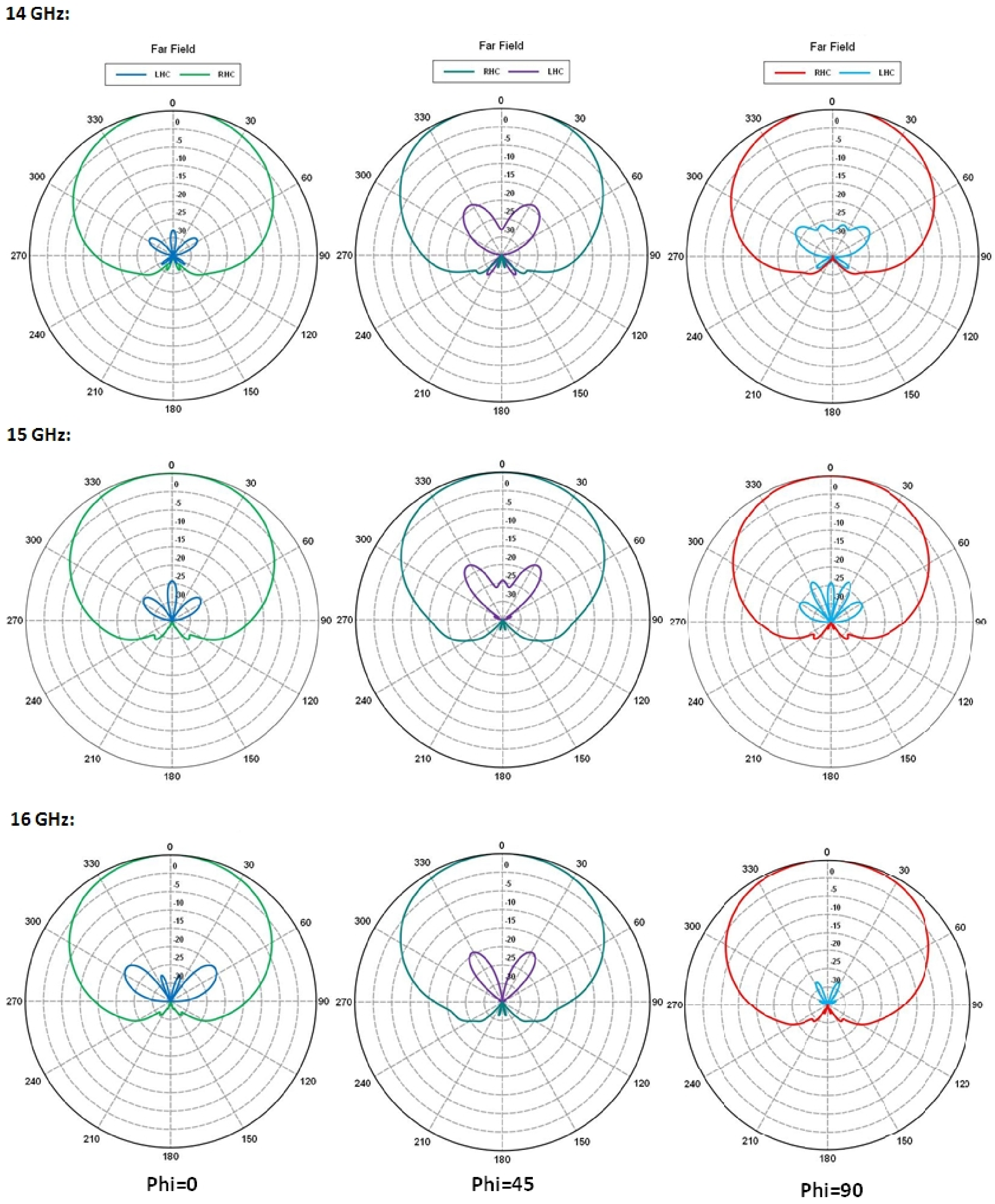

Figure 6-9: Gain (dB) for principal planes $\phi = 0°$, a diagonal cut $\phi = 45°$ and $\phi = 90°$ at 14, 15 and 16 GHz

17 GHz:

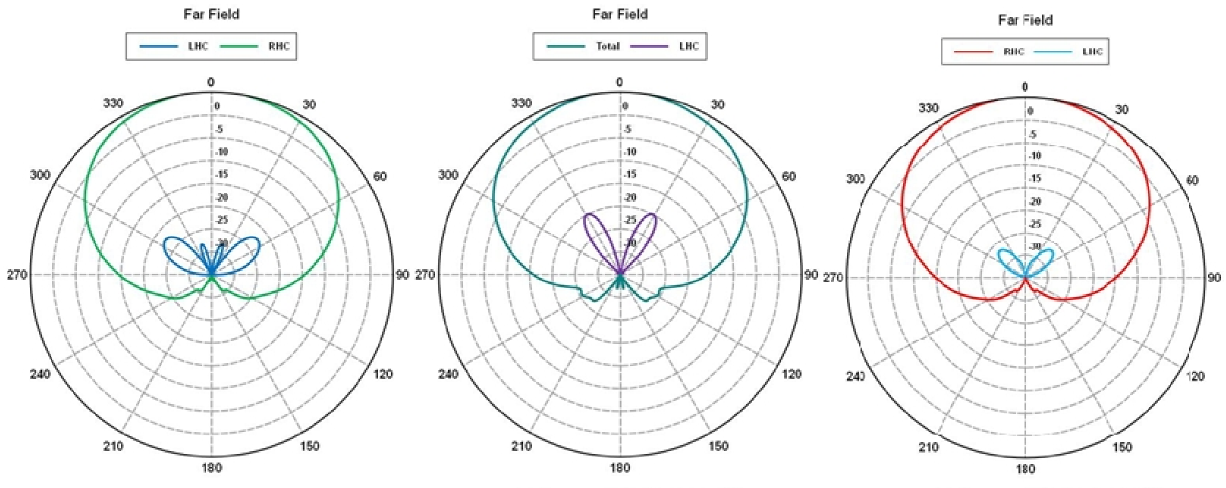

18 GHz:

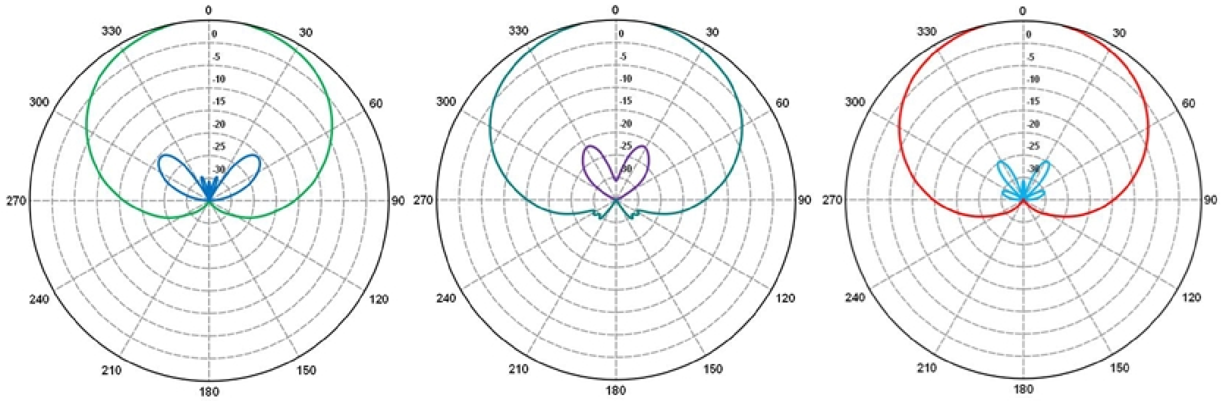

Figure 6-10: Gain (dB) for principal planes $\phi = 0°$, a diagonal cut $\phi = 45°$ and $\phi = 90°$ at 17, and 18 GHz

VSWR

Figure 6-14 shows the VSWR performance of the cavity-backed spiral antenna. The VSWR is referenced to 188Ω and is less than 2.5:1 for the entire bandwidth of operation, representing a fairly good design.

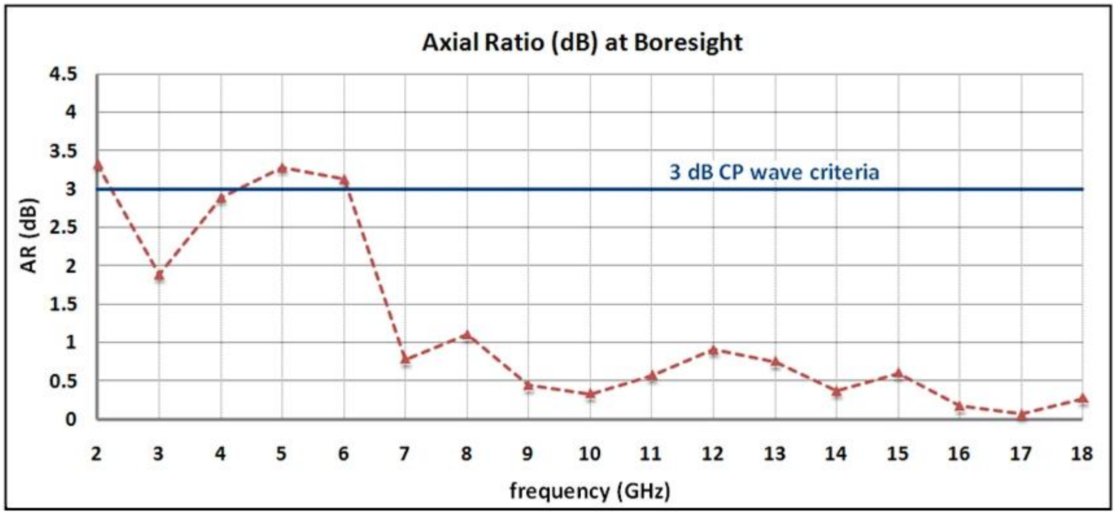

Figure 6-11: Axial Ratio (dB) vs. Frequency (GHz)

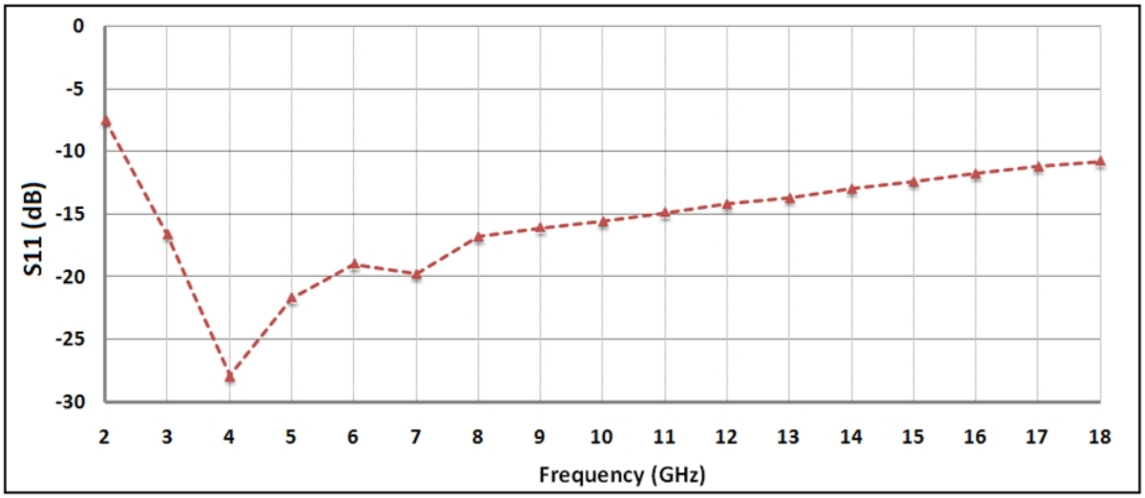

Figure 6-12: S11 (dB) vs. Frequency (GHz)

6.1.3 Discussion

Performance Comparison of Polygonal Spiral with Circular and Square Spiral

We compared the radiation performance of a 2" diameter shallow cavity-backed polygonal spiral antenna with 2" circular spiral and a 2" square spiral antenna. The results show that the polygonal antenna significantly improved the axial ratio of the antenna while maintaining equivalent gain-bandwidth performance of both a circular spiral

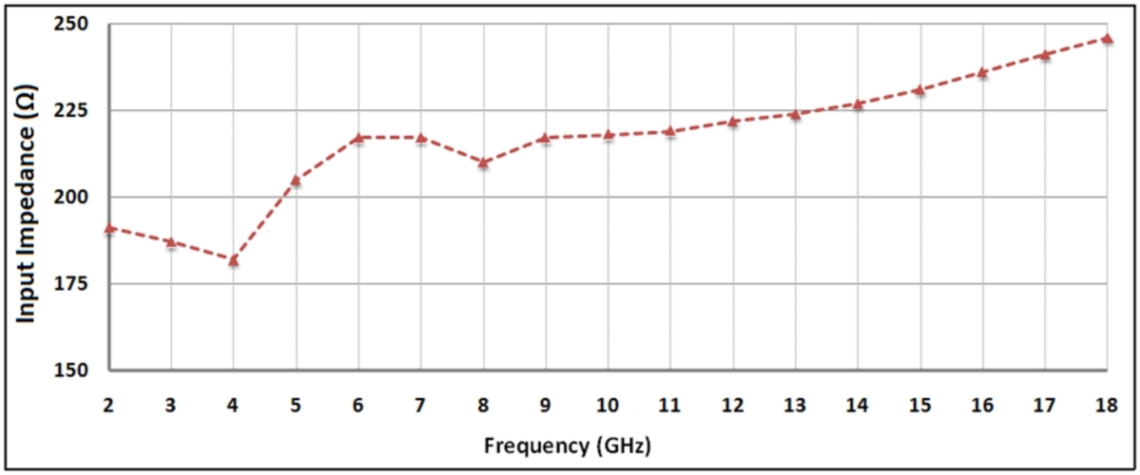

Figure 6-13: Input Impedance vs. Frequency (GHz)

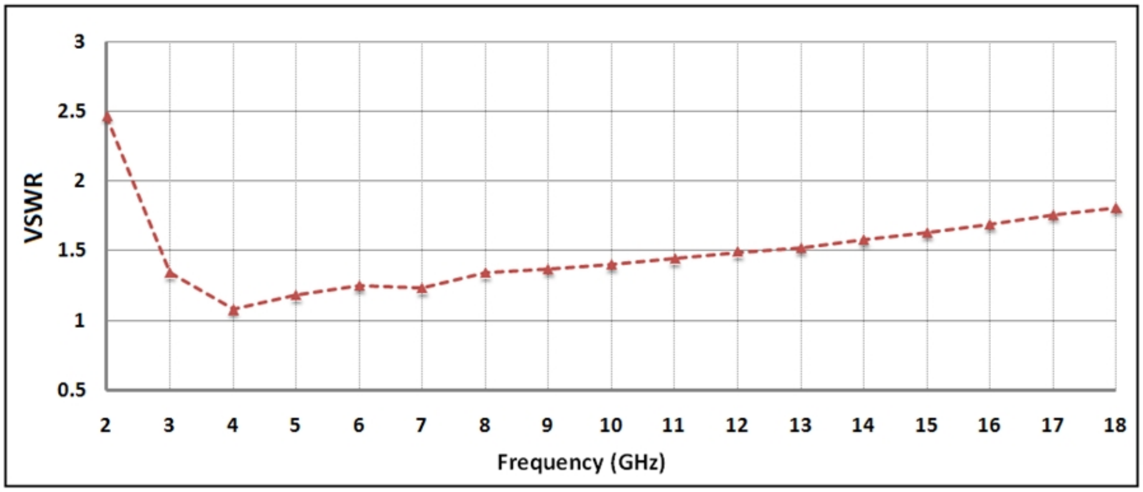

Figure 6-14: VSWR vs. Frequency (GHz)

and a square spiral. Table 6.1 demonstrates the performance comparison of a polygonal spiral and a circular spiral from 2-18 GHz at 1 GHz intervals.

Table 6.2 demonstrates the performance comparison of a polygonal spiral and a square spiral from 2-18 GHz at 2 GHz intervals. It is evident that circular spirals operate with better axial ratio than their square counterparts, and that, for equal diameters, the polygonal spiral has the best axial ratio performance of all three configurations.

Table 6.1: BORESIGHT RHC AND LHC GAIN, AXIAL RATIO, S11, VSWR, AND INPUT IMPEDANCE COMPARISON OF CIRCULAR AND ORIGINAL POLYGONAL SPIRAL ANTENNA

f(GHz)	Gain (dB)				AR(dB)		S11(dB)		VSWR		Input Ω	
	RHC		LHC									
	Circ.	Poly.	Circ.	Poly.	Circ.	Poly.	Circ.	Poly.	Circ.	Poly.	Circ.	Poly.
2	-2.22	-1.94	-7.26	-16.4	11.00	3.33	-6.73	-7.45	2.71	2.47	70.3	191
3	1.22	0.80	-12.7	-18.6	-3.57	1.88	-13.9	-16.6	1.50	1.34	128	187
4	3.84	3.29	-8.53	-12.4	4.26	2.89	-13.9	-27.9	1.50	1.08	127	182
5	5.56	4.51	-7.02	-10.1	4.16	3.28	-12.1	-21.7	1.65	1.18	115	205
6	6.37	5.08	-19.8	-9.9	0.86	3.13	-13.7	-19.0	1.52	1.25	124	217
7	6.58	6.07	-32.5	-20.9	0.19	0.78	-13.2	-19.8	1.56	1.23	121	217
8	6.52	6.49	-36.0	-17.5	0.13	1.10	-13.9	-16.8	1.50	1.34	125	210
9	6.04	6.27	-40.9	-25.8	0.08	0.44	-14.2	-16.1	1.48	1.37	127	217
10	5.24	5.75	-52.3	-28.8	0.02	0.33	-12.6	-15.6	1.61	1.40	117	218
11	4.09	5.77	-49.2	-23.9	0.04	0.57	-9.08	-14.9	2.08	1.44	91.7	219
12	4.01	5.58	-50.2	-20.0	0.03	0.91	-9.81	-14.2	1.95	1.49	97	222
13	4.55	5.24	-54.5	-22.1	0.02	0.75	-10.1	-13.7	1.90	1.52	101	224
14	4.96	5.51	-48.8	-28.0	0.04	0.37	-10.6	-13.0	1.83	1.58	105	227
15	5.15	4.92	-53.3	-24.3	0.02	0.60	-11.0	-12.4	1.79	1.63	106	231
16	5.46	5.05	-57.0	-35.0	0.01	0.17	-11.6	-11.8	1.72	1.69	110	236
17	5.58	5.26	-86.5	-42.5	0.00	0.07	-11.8	-11.2	1.69	1.76	111	241
18	5.66	5.41	-64.9	-30.7	0.01	0.27	-12.5	-10.8	1.62	1.81	117	246

Table 6.2: BORESIGHT RHC AND LHC GAIN, AXIAL RATIO, S11, VSWR, AND INPUT IMPEDANCE COMPARISON OF SQUARE AND ORIGINAL POLYGONAL SPIRAL ANTENNA

f(GHz)	Gain (dB)				AR(dB)		S11(dB)		VSWR		Input Ω	
	RHC		LHC									
	Sqr.	Poly.	Sqr.	Poly.	Sqr.	Poly.	Sqr.	Poly.	Sqr.	Poly.	Sqr.	Poly.
2	-1.54	-1.94	-18.1	-16.4	2.59	3.33	-28.1	-7.45	1.08	2.47	201	191
4	3.23	3.29	-13.3	-12.4	2.6	2.89	-25.8	-27.9	1.11	1.08	208	182
6	5.53	5.08	-8.97	-9.9	3.31	3.13	-28.4	-19.0	1.08	1.25	203	217
8	6.23	6.49	-5.11	-17.5	4.83	1.10	-22.6	-16.8	1.16	1.34	204	210
10	5.51	5.75	-5.63	-28.8	4.95	0.33	-23.9	-15.6	1.14	1.40	211	218
12	4.19	5.58	-5.36	-20.0	6.01	0.91	-24.9	-14.2	1.12	1.49	207	222
14	5.05	5.51	-4.73	-28.0	5.85	0.37	-21	-13.0	1.20	1.58	214	227
16	5.84	5.05	-3.86	-35.0	5.9	0.17	-18.9	-11.8	1.26	1.69	219	236
18	4.82	5.41	-7.04	-30.7	4.53	0.27	-18	-10.8	1.29	1.81	221	246

Performance Analysis of Polygonal Spiral at Lower Frequencies

To verify the axial ratio performance of the polygonal spiral antenna at lower frequencies, we simulated the model from 2-4 GHz at 100 MHz intervals and compared the axial ratio to that of a circular spiral. Table 6.3 demonstrates the performance comparison of a polygonal spiral and a circular spiral from 2-4 GHz at 0.1 GHz intervals. The polygonal spiral shows ≥ 3dB axial ratio at frequency interval 2.0-2.4 GHz and in the vicinity of 3.3 GHz. The axial ratio degradation is explained in terms of the current band theory next.

Table 6.3: BORESIGHT RHC AND LHC GAIN, AXIAL RATIO, S11, VSWR, AND INPUT IMPEDANCE COMPARISON OF A CIRCULAR AND ORGINAL POLYGONAL SPIRAL ANTENNA AT LOW FREQUENCIES

f(GHz)	Gain (dB)				AR(dB)		S11(dB)		VSWR		Input Ω	
	RHC		LHC									
	Circ.	Poly.	Circ.	Poly.	Circ.	Poly.	Circ.	Poly.	Circ.	Poly.	Circ.	Poly.
2	-2.220	-1.96	-7.26	-16.5	11.00	3.29	-6.73	-7.42	2.71	2.48	70.3	192
2.1	-0.867	-1.19	-9.35	-13.9	6.88	4.10	-10.8	-13.8	1.81	1.51	109	270
2.2	-0.261	-1.04	-12.0	-13.4	4.61	4.29	-13.5	-18.0	1.53	1.29	125	238
2.3	0.001	-1.57	-14.1	-11.6	3.48	5.68	-14.5	-11.0	1.46	1.78	129	314
2.4	0.109	-0.60	-14.9	-14.3	3.11	3.63	-15.1	-16.4	1.43	1.36	132	139
2.5	0.152	-0.52	-14.9	-14.5	3.11	3.51	-15.0	-11.5	1.43	1.73	132	189
2.6	0.277	-0.203	-14.4	-18.9	3.25	2.02	-13.9	-13.5	1.50	1.53	126	264
2.7	0.571	0.025	-13.6	-19.1	3.46	1.92	-12.8	-15.6	1.60	1.40	118	261
2.8	0.843	0.229	-13.0	-19.8	3.59	1.73	-12.4	-17.3	1.63	1.31	115	210
2.9	0.985	0.581	-12.8	-20.0	3.61	1.63	-12.7	-20.9	1.60	1.20	118	157
3.0	1.220	0.756	-12.7	-18.8	3.56	1.84	-14.1	-17.2	1.49	1.32	127	189
3.1	1.680	0.961	-11.8	-16.2	3.73	2.41	-15.7	-16.4	1.39	1.36	135	240
3.2	1.99	1.25	-11.0	-16.8	3.98	2.19	-15.8	-17.4	1.39	1.31	136	246
3.3	2.04	1.31	-10.8	-11.9	4.01	3.87	-14.0	-20.9	1.50	1.20	128	194
3.4	2.27	1.67	-10.8	-14.1	3.91	2.86	-12.5	-21.7	1.62	1.18	117	164
3.5	2.64	1.86	-10.0	-17.3	4.12	1.92	-12.0	-21.2	1.67	1.19	113	191
3.6	2.82	2.23	-9.48	-13.8	4.30	2.76	-12.5	-22.1	1.63	1.17	116	202
3.7	3.12	2.48	-9.50	-14.7	4.14	2.42	-14.3	-19.5	1.48	1.24	130	219
3.8	3.56	2.72	-8.93	-17.3	4.20	1.74	-15.4	-23.3	1.41	1.19	135	208
3.9	3.72	2.95	-8.33	-14.4	4.43	2.36	-15.1	-21.6	1.42	1.44	132	201
4.0	3.79	3.17	-8.56	-12.5	4.27	2.88	-13.0	-23.4	1.58	1.15	119	192

Analysis of Axial Ratio Performance of Polygonal Spiral Antenna

The polygonal spiral antenna demonstrates ≥ 3 dB axial ratio at narrow frequency intervals. The reason for the axial ratio degradation at particular discrete frequencies can be best understood from a heuristic approach and explained in terms of the current band theory explained earlier in chapter 2.

In the polygonal spiral antenna, the radiating current bands or in-phase currents in adjacent arms are rotating with time. When the effective wavelength is such that the current band or the same phase currents between the adjacent arms reaches a point where one arm is transitioning the antenna geometry from a 2^n side polygon to a to a 2^{n-1} side polygon, while the other arm remains in a 2^n sided polygonal turn, the currents are no longer in phase in the vicinity of the transition point. Furthermore, at the transition points, a differential group of currents in phase quadrature may not be available, which is a necessary condition for the radiation of circularly polarized waves. The out-of-phase currents at the transition points for the original polygonal model are illustrated in Figure 6-15.

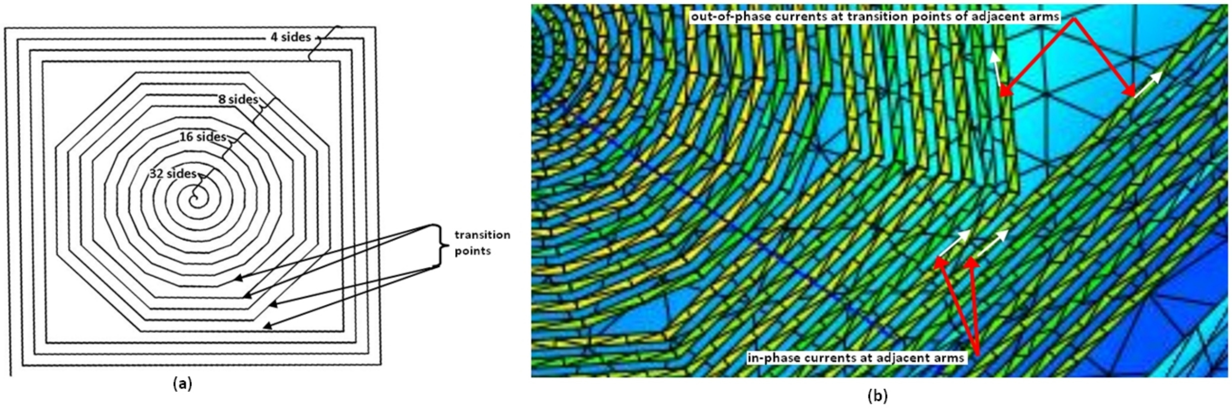

(a)

(b)

Figure 6-15: (a) transition points in polygonal spiral antenna (b) in-phase and out-of-phase currents in adjacent arms in a polygonal spiral antenna

The narrowband axial ratio deterioration can thus be attributed to the fact that the current wavelengths corresponding to these frequencies are located at the transition points of the polygonal geometry. For this reason, we have further developed and analyzed three modifications to the original polygonal structure to reduce abrupt transition from a 2^n side polygon to a to a 2^{n-1} side polygon, as will be explained next.

6.2 Polygonal Spiral Antenna with 12th Interpolated Turn

6.2.1 Antenna Geometry

In our initial geometry of the polygonal spiral antenna, we observed ≥ 3 dB axial ratios at discrete frequencies 2.1-2.5 GHz and at 3.3 GHz. This phenomenon can be attributed to the fact that the current wavelengths corresponding to these frequencies are located at the transition points of the polygonal geometry. In this model, we have modified the 12th turn of the spiral such that instead of a regular octagon, the spiral arm is an octagon interpolated from an 8-sided to a 4-sided polygon. The purpose of this modification is to reduce the transition gap in the antenna model to allow for a smoother transition from an 8 sided to a 4 sided polygon and reduce the axial ratio at 2.1-2.5 GHz range. The spiral curve and the corresponding fabricated antenna model are shown in Figure 6-16.

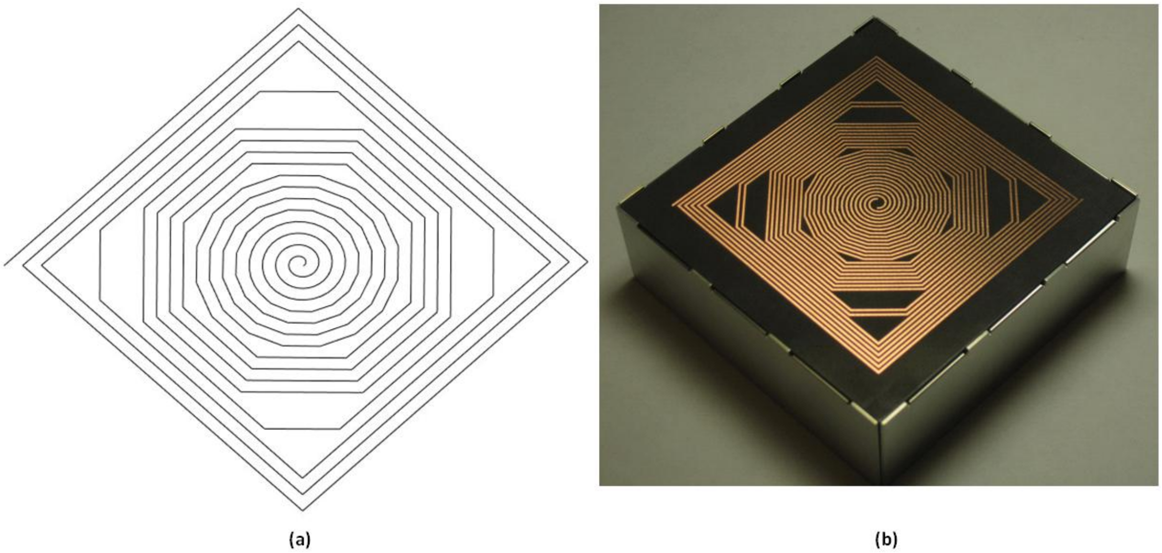

Figure 6-16: (a) Spiral Curve (b) Fabricated Antenna

The computer code used to generate the spiral curve is included in Appendix A.

6.2.2 Results

Gain

The polar plots for gain (dB) for principal planes $\phi = 0°$ and $\phi = 90°$ and a diagonal cut $\phi = 45°$ are shown in Figures 6-17, 6-18, 6-19, 6-20, 6-21 and 6-22. The antenna demonstrates sufficiently high and stable gains, low sidelobes and no splits in the main beam across the bandwidth.

Axial Ratio

In this modification of the polygonal spiral antenna, we were able to observe significant improvements in axial ratio performance. The low-frequency axial ratios at 2-2.2 GHz and at 3.5 GHz remained slightly above 3 dB. The axial ratio remained $\leq$ 3dB for 98.5% of the 2-18 GHz bandwidth. Figure 6-23 demonstrates the overall axial ratio performance for the polygonal spiral with last interpolated turn antenna model. This configuration of polygonal spiral gave the best axial ratio performance of all four configurations.

S11

Figure 6-24 shows the reflection coefficient at the antenna input port assuming matched conditions. The results show that the reflection coefficient is efficiently minimized to adequate levels across the bandwidth.

2 GHz:

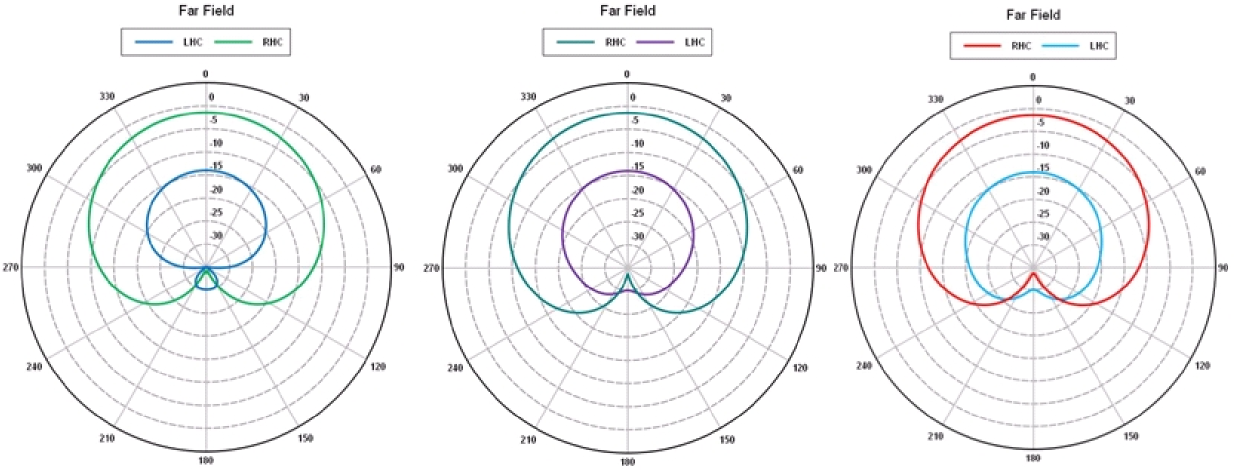

3 GHz:

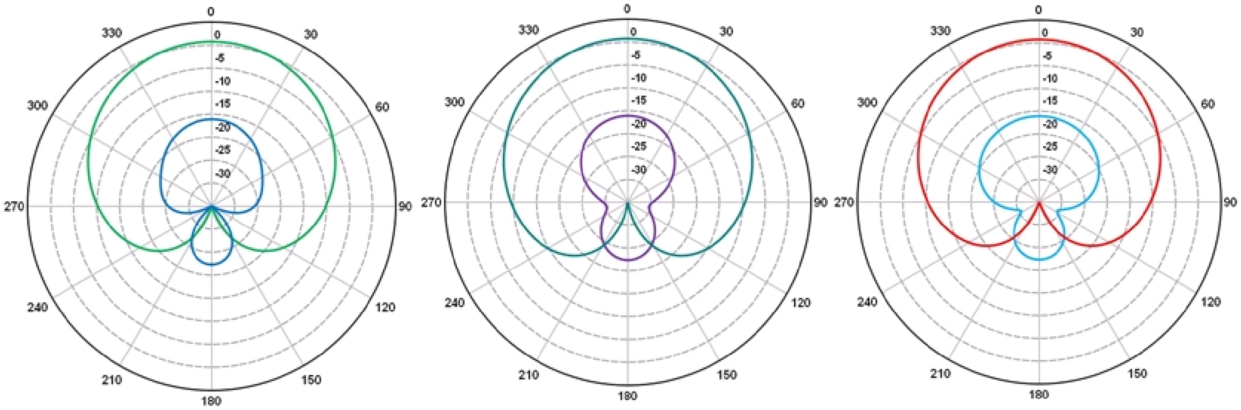

4 GHz:

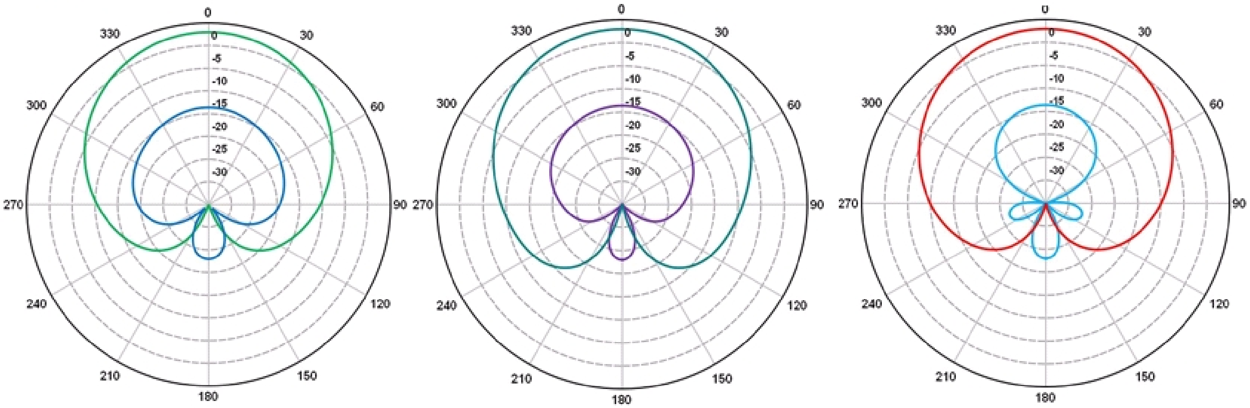

Phi=0 **Phi=45** **Phi=90**

Figure 6-17: Gain (dB) for principal planes $\phi = 0°$, a diagonal cut $\phi = 45°$ and $\phi = 90°$ at 2, 3 and 4 GHz

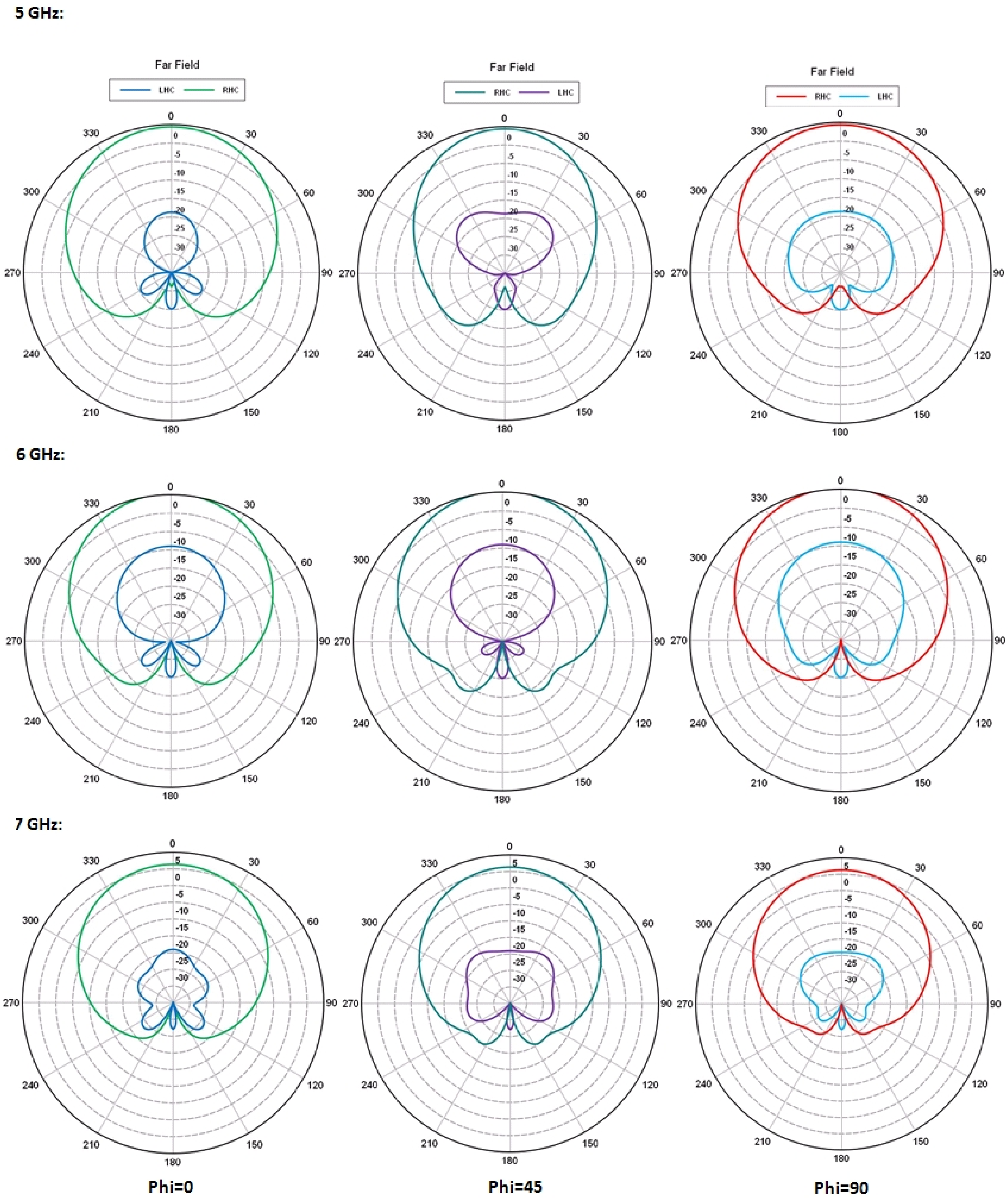

Figure 6-18: Gain (dB) for principal planes $\phi = 0°$, a diagonal cut $\phi = 45°$ and $\phi = 90°$ at 5, 6 and 7 GHz

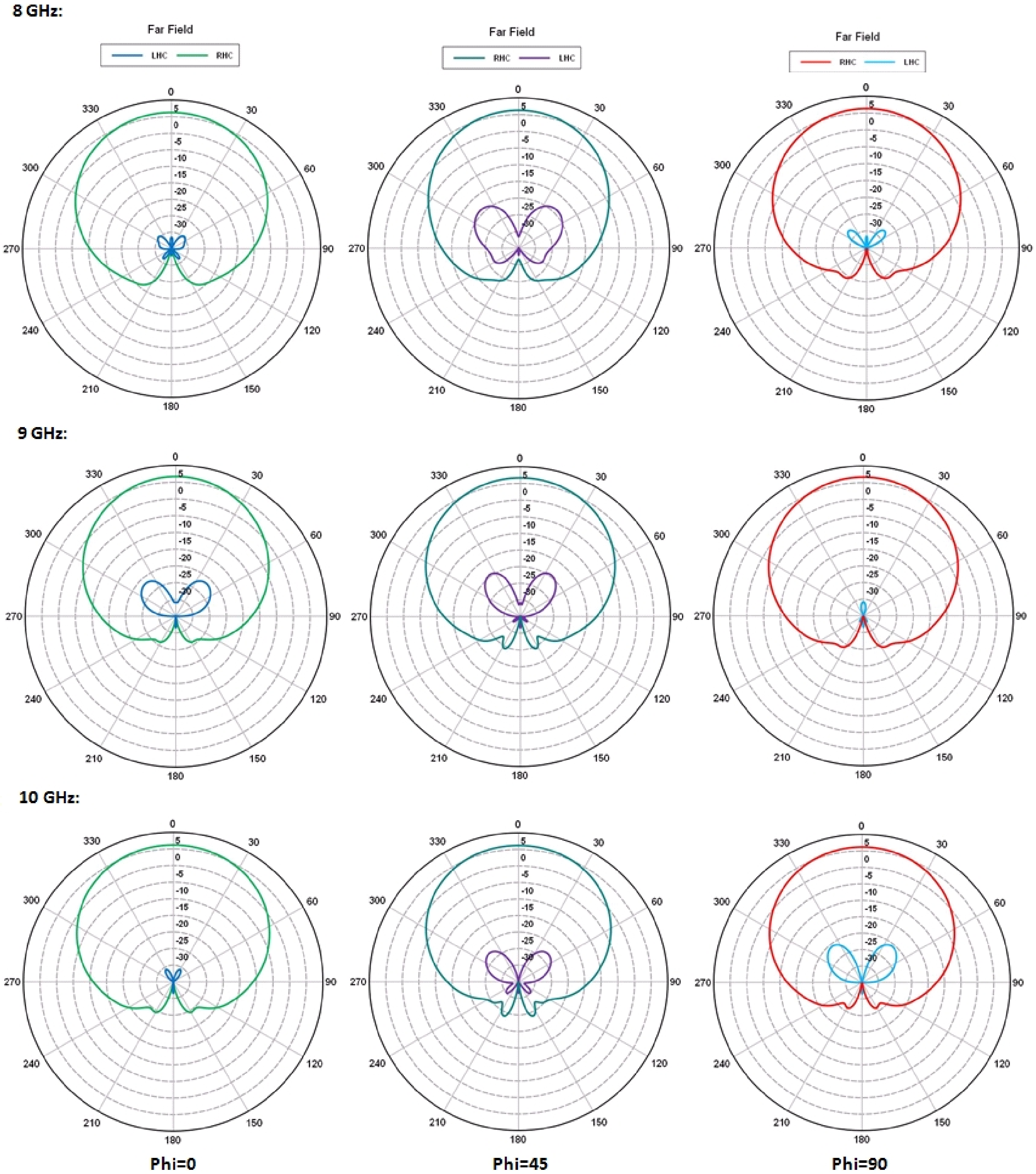

Figure 6-19: Gain (dB) for principal planes $\phi = 0°$, a diagonal cut $\phi = 45°$ and $\phi = 90°$ at 8, 9 and 10 GHz

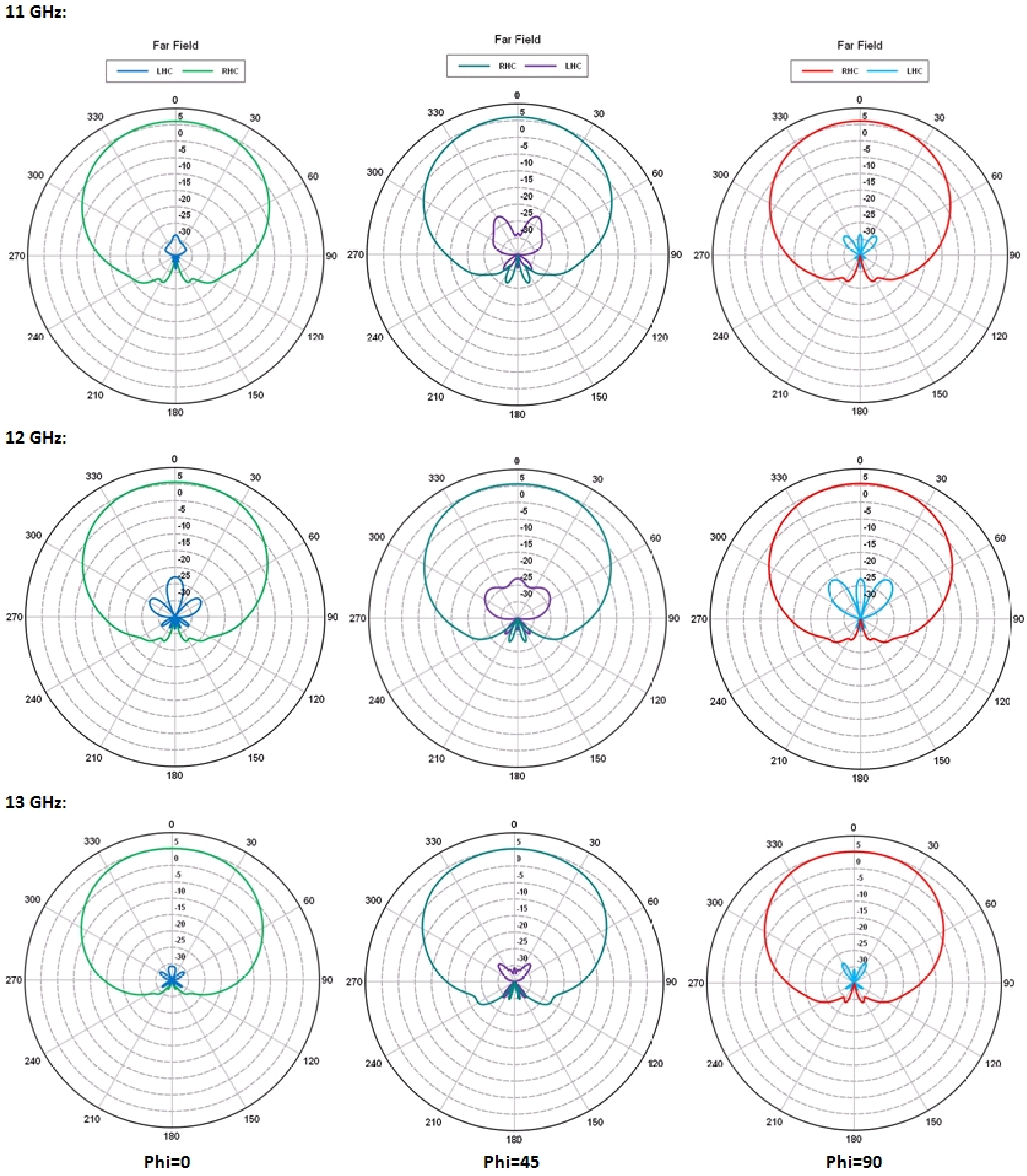

Figure 6-20: Gain (dB) for principal planes $\phi = 0°$, a diagonal cut $\phi = 45°$ and $\phi = 90°$ at 11, 12 and 13 GHz

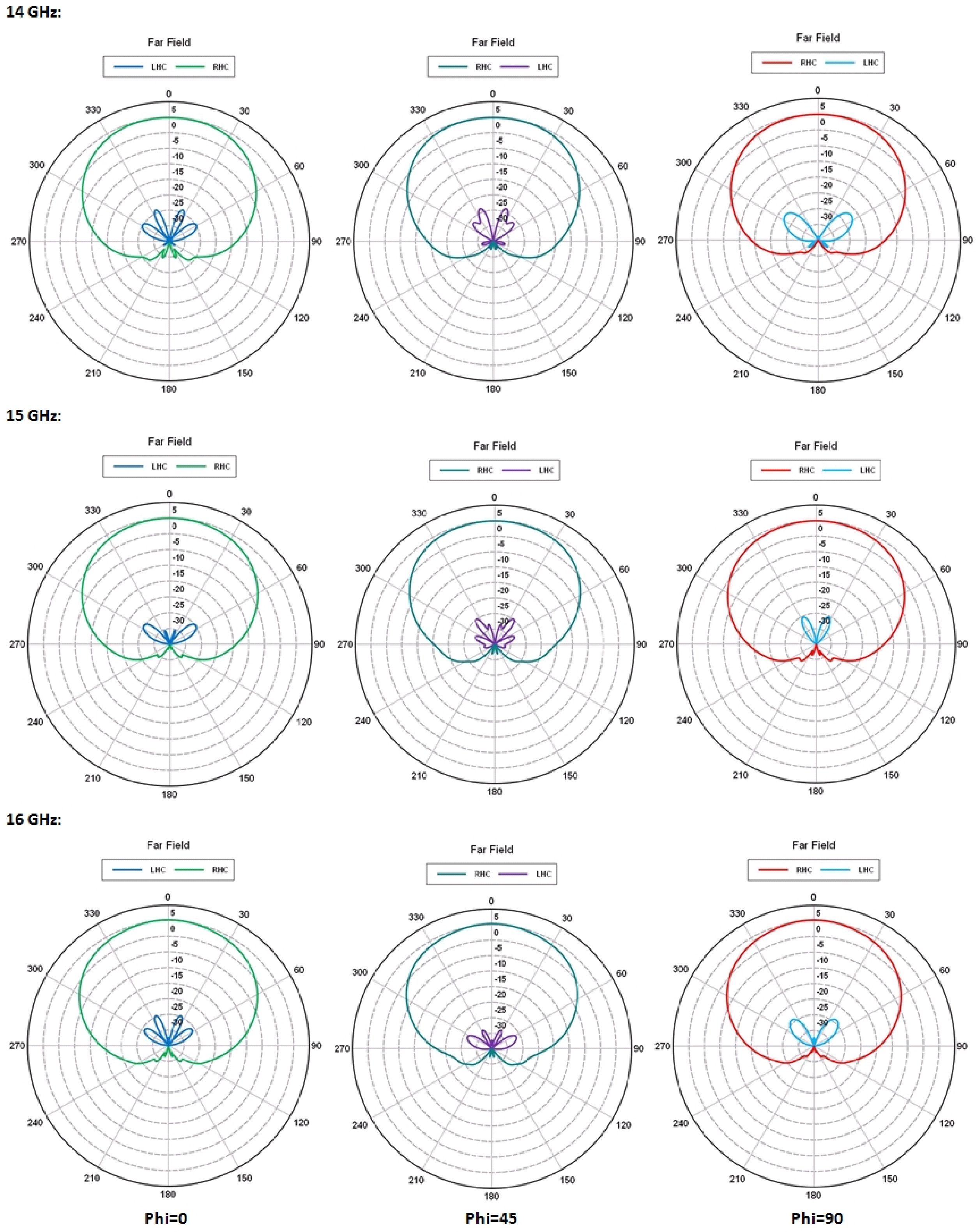

Figure 6-21: Gain (dB) for principal planes $\phi = 0°$, a diagonal cut $\phi = 45°$ and $\phi = 90°$ at 14, 15 and 16 GHz

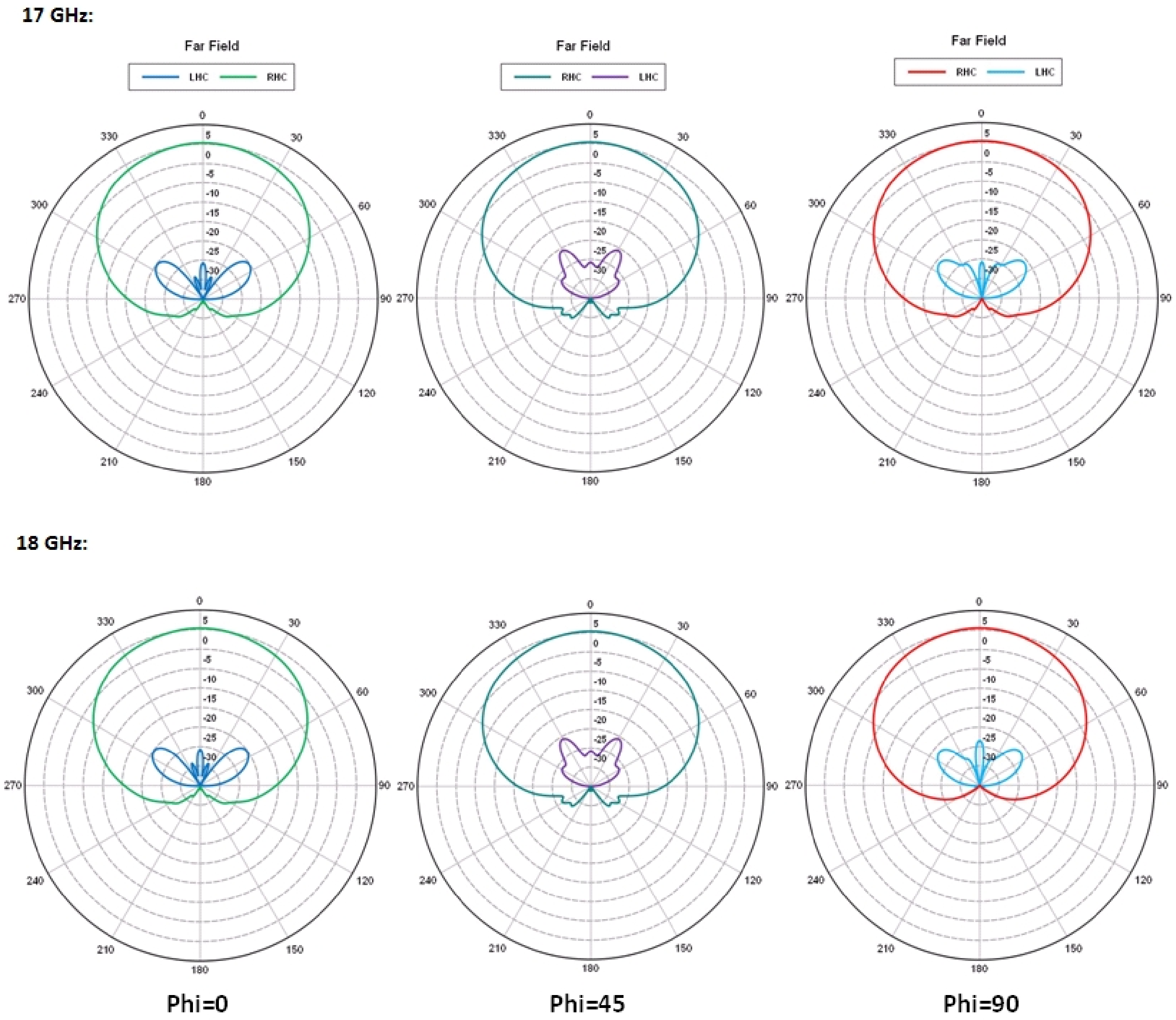

Figure 6-22: Gain (dB) for principal planes $\phi = 0°$, a diagonal cut $\phi = 45°$ and $\phi = 90°$ at 17 and 18 GHz

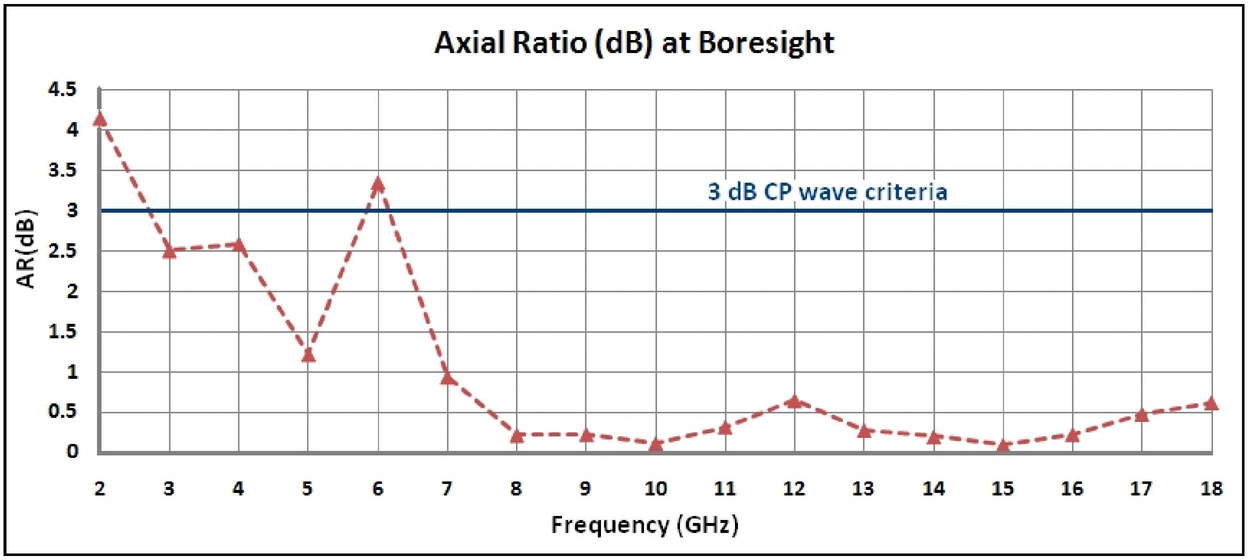

Figure 6-23: Axial Ratio (dB) vs. Frequency (GHz)

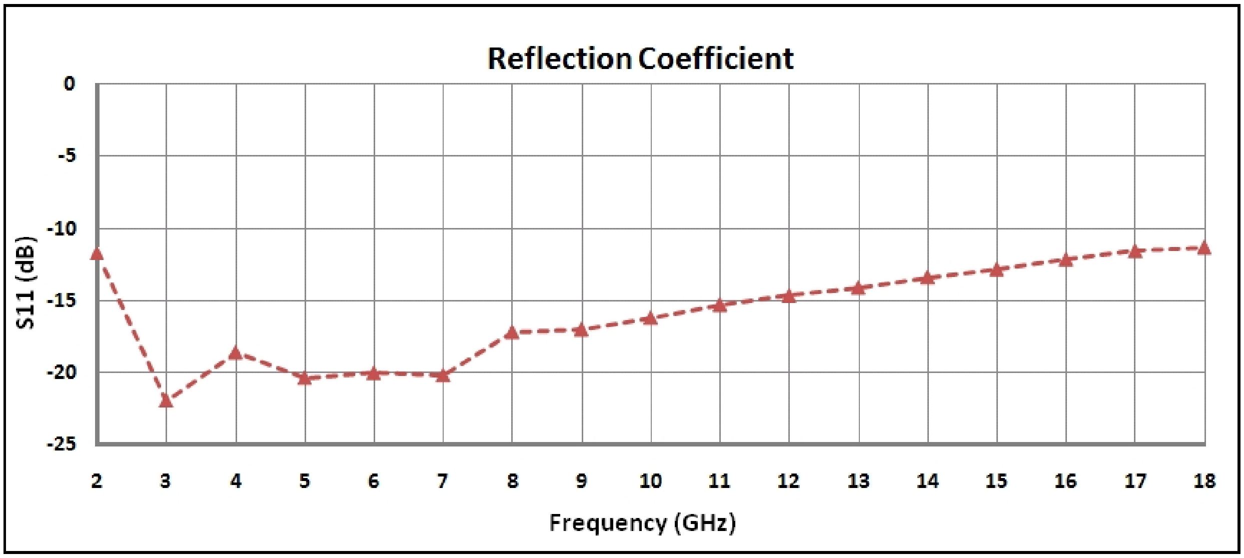

Figure 6-24: S11 (dB) vs. Frequency (GHz)

Input Impedance

Figure 6-25 shows the input impedance to the cavity-backed Archimedean spiral antenna. The antenna realizes a near constant input impedance structure over an ultra-wide bandwidth. This configuration of polygonal spiral antenna demonstrates the best input impedance performance of the four configurations.

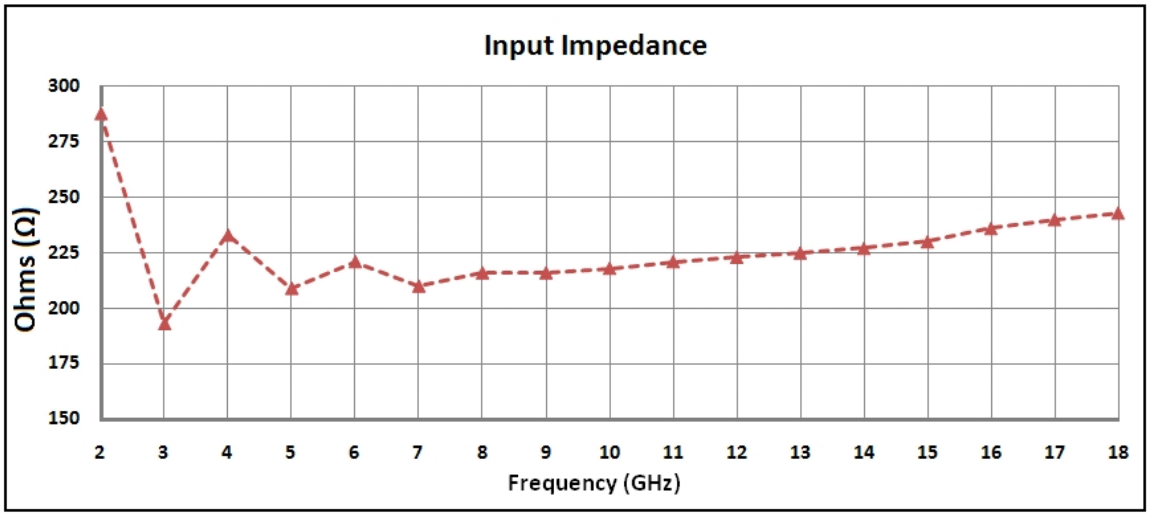

Figure 6-25: Input Impedance vs. Frequency (GHz)

VSWR

Figure 6-26 shows the VSWR performance of the cavity-backed spiral antenna. The VSWR is referenced to 188Ω and is approximately less than 2:1 for the entire bandwidth of operation, resembling the best VSWR performance of the four configurations.

6.2.3 Discussion

Performance Comparison of Polygonal Spiral with Circular and Square Spiral

Table 6.4 demonstrates the performance comparison of a polygonal spiral with 12th interpolated last turn and a circular spiral from 2-18 GHz at 1 GHz intervals.

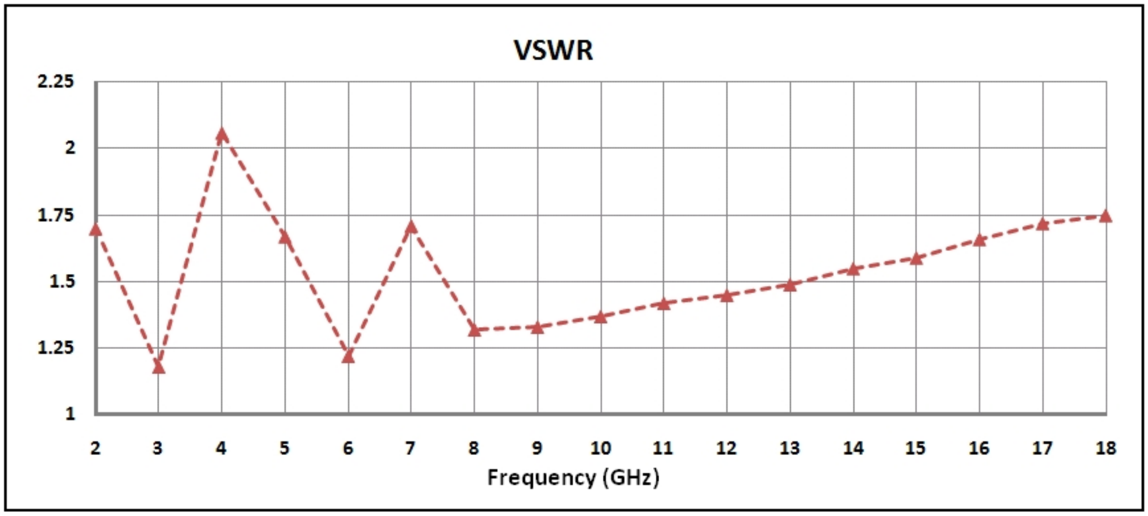

Figure 6-26: VSWR vs. Frequency (GHz)

Table 6.4: BORESIGHT RHC AND LHC GAIN, AXIAL RATIO, S11, VSWR, AND INPUT IMPEDANCE COMPARISON OF CIRCULAR AND POLYGONAL SPIRAL ANTENNA WITH 12TH INTERPOLATED TURN

f(GHz)	Gain (dB)				AR(dB)		S11(dB)		VSWR		Input Ω	
	RHC		LHC									
	Circ.	Poly.	Circ.	Poly.	Circ.	Poly.	Circ.	Poly.	Circ.	Poly.	Circ.	Poly.
2	-2.22	-1.46	-7.26	-14.0	11.00	4.16	-6.73	-11.735	2.71	1.70	70.3	288
3	1.22	0.77	-12.7	-16.1	-3.57	2.51	-13.9	-21.942	1.50	1.18	128	193
4	3.84	2.97	-8.53	-13.6	4.26	2.59	-13.9	-18.579	1.50	2.06	127	233
5	5.56	4.35	-7.02	-18.7	4.16	1.22	-12.1	-20.362	1.65	1.67	115	209
6	6.37	5.33	-19.8	-9.03	0.86	3.36	-13.7	-20.022	1.52	1.22	124	221
7	6.58	6.31	-32.5	-19.1	0.19	0.94	-13.2	-20.164	1.56	1.71	121	210
8	6.52	6.29	-36.0	-31.5	0.13	0.22	-13.9	-17.195	1.50	1.32	125	216
9	6.04	6.66	-40.9	-30.8	0.08	0.23	-14.2	-16.98	1.48	1.33	127	216
10	5.24	6.16	-52.3	-36.9	0.02	0.12	-12.6	-16.18	1.61	1.37	117	218
11	4.09	6.00	-49.2	-28.6	0.04	0.32	-9.08	-15.29	2.08	1.42	91.7	221
12	4.01	5.57	-50.2	-23.0	0.03	0.65	-9.81	-14.65	1.95	1.45	97	223
13	4.55	5.17	-54.5	-30.8	0.02	0.28	-10.1	-14.09	1.90	1.49	101	225
14	4.96	4.90	-48.8	-33.7	0.04	0.20	-10.6	-13.38	1.83	1.55	105	227
15	5.15	4.91	-53.3	-39.7	0.02	0.10	-11.0	-12.82	1.79	1.59	106	230
16	5.46	5.25	-57.0	-32.3	0.01	0.23	-11.6	-12.12	1.72	1.66	110	236
17	5.58	5.33	-86.5	-25.8	0.00	0.48	-11.8	-11.54	1.69	1.72	111	240
18	5.66	5.52	-64.9	-23.5	0.01	0.62	-12.5	-11.30	1.62	1.75	117	243

Table 6.5 demonstrates the performance comparison of a polygonal spiral with interpolated last turn and a square spiral from 2-18 GHz at 2 GHz intervals.

Table 6.5: BORESIGHT RHC AND LHC GAIN, AXIAL RATIO, S11, VSWR, AND INPUT IMPEDANCE COMPARISON OF SQUARE AND POLYGONAL SPIRAL ANTENNA WITH 12TH INTERPOLATED TURN

f(GHz)	Gain (dB)				AR(dB)		S11(dB)		VSWR		Input Ω	
	RHC		LHC									
	Sqr.	Poly.	Sqr.	Poly.	Sqr.	Poly.	Sqr.	Poly.	Sqr.	Poly.	Sqr.	Poly.
2	-1.54	-1.46	-18.1	-14.0	2.59	4.16	-28.1	-11.735	1.08	1.70	201	288
4	3.23	2.97	-13.3	-13.6	2.6	2.59	-25.8	-18.579	1.11	2.06	208	233
6	5.53	5.33	-8.97	-9.03	3.31	3.36	-28.4	-20.022	1.08	1.22	203	221
8	6.23	6.29	-5.11	-31.5	4.83	0.22	-22.6	-17.195	1.16	1.32	204	216
10	5.51	6.16	-5.63	-36.9	4.95	0.12	-23.9	-16.18	1.14	1.37	211	218
12	4.19	5.57	-5.36	-23.0	6.01	0.65	-24.9	-14.65	1.12	1.45	207	223
14	5.05	4.90	-4.73	-33.7	5.85	0.20	-21	-13.38	1.20	1.55	214	227
16	5.84	5.25	-3.86	-32.3	5.9	0.23	-18.9	-12.12	1.26	1.66	219	236
18	4.82	5.52	-7.04	-23.5	4.53	0.62	-18	-11.30	1.29	1.75	221	243

Performance Analysis of Polygonal Spiral at Lower Frequencies

To verify the axial ratio performance of the polygonal spiral antenna at lower frequencies, we simulated the model from 2-4 GHz and 5-7 GHz at 100 MHz intervals. Table 6.6 demonstrates the performance comparison of a polygonal spiral and a circular spiral from 2-4 GHz at 0.1 GHz intervals. The polygonal spiral shows ≥ 3 dB axial ratio at frequency interval 2.0-2.23 GHz, 5.9-6.2 GHz and in the vicinity of 5.4 and 3.5 GHz.

Table 6.6: BORESIGHT RHC AND LHC GAIN, AXIAL RATIO, S11, VSWR, AND INPUT IMPEDANCE COMPARISON OF A CIRCULAR AND POLYGONAL SPIRAL ANTENNA WITH 12TH INTERPOLATED TURN AT LOW FREQUENCIES

f(GHz)	Gain (dB)				AR(dB)		S11(dB)		VSWR		Input Ω	
	RHC		LHC									
	Circ.	Poly.	Circ.	Poly.	Circ.	Poly.	Circ.	Poly.	Circ.	Poly.	Circ.	Poly.
2	-2.220	-1.46	-7.26	-14.0	11.00	4.16	-6.73	-11.74	2.71	1.70	70.3	288
2.1	-0.867	-1.32	-9.35	-13.5	6.88	4.34	-10.8	-14.27	1.81	1.48	109	237
2.2	-0.261	-1.15	-12.0	-13.9	4.61	4.06	-13.5	-13.72	1.53	1.52	125	148
2.3	0.001	-0.71	-14.1	-17.0	3.48	2.69	-14.5	-14.32	1.46	1.48	129	229
2.4	0.109	-0.52	-14.9	-16.6	3.11	2.73	-15.1	-14.03	1.43	1.50	132	260
2.5	0.152	-0.45	-14.9	-22.2	3.11	1.42	-15.0	-13.94	1.43	1.50	132	270
2.6	0.277	-0.09	-14.4	-25.6	3.25	0.92	-13.9	-18.69	1.50	1.26	126	167
2.7	0.571	0.09	-13.6	-22.7	3.46	1.26	-12.8	-17.03	1.60	1.33	118	175
2.8	0.843	0.01	-13.0	-21.7	3.59	1.53	-12.4	-15.22	1.63	1.42	115	244
2.9	0.985	0.41	-12.8	-16.9	3.61	2.40	-12.7	-15.36	1.60	1.41	118	265
3.0	1.220	0.77	-12.7	-16.1	3.56	2.51	-14.1	-21.94	1.49	1.17	127	193
3.1	1.680	0.98	-11.8	-15.6	3.73	2.60	-15.7	-24.13	1.39	1.08	135	173
3.2	1.99	1.23	-11.0	-16.0	3.98	2.41	-15.8	-22.64	1.39	1.16	136	197
3.3	2.04	1.31	-10.8	-15.4	4.01	2.56	-14.0	-18.34	1.50	1.27	128	217
3.4	2.27	1.81	-10.8	-15.3	3.91	2.44	-12.5	-23.10	1.62	1.15	117	214
3.5	2.64	1.79	-10.0	-12.0	4.12	3.60	-12.0	-20.29	1.67	1.21	113	218
3.6	2.82	2.36	-9.48	-15.4	4.30	2.26	-12.5	-24.97	1.63	1.12	116	199
3.7	3.12	2.45	-9.50	-20.15	4.14	1.29	-14.3	-19.54	1.48	1.24	130	200
3.8	3.56	2.68	-8.93	-12.9	4.20	2.90	-15.4	-20.57	1.41	1.21	135	214
3.9	3.72	2.96	-8.33	-14.0	4.43	2.47	-15.1	-18.96	1.42	1.25	132	215
4.0	3.79	2.97	-8.56	-13.62	4.27	2.59	-13.0	-18.58	1.58	1.27	119	233
5.0	5.56	4.35	-7.02	-18.7	4.16	1.22	-12.1	-20.362	1.65	1.67	115	209
5.1	5.02	4.38	-7.70	-21.2	4.09	0.91	-8.94	-22.97	2.11	1.15	93	206
5.2	5.27	4.74	-7.67	-13.4	4.05	2.15	-7.93	-24.68	2.34	1.12	94	193
5.3	5.24	4.73	-7.57	-11.6	3.73	2.67	-7.93	-18.47	2.36	1.27	98	198
5.4	5.66	4.74	-8.25	-10.5	3.51	3.03	-9.24	-19.48	2.04	1.24	110	213
5.5	5.99	4.77	-8.35	-9.80	3.37	3.54	-12.0	-16.80	1.67	1.34	134	210
5.6	6.11	4.93	-8.35	-12.1	2.82	2.45	-14.74	-18.08	1.45	1.29	157	232
5.7	6.35	5.19	-9.75	-23.0	2.31	0.68	-16.96	-22.24	1.33	1.17	172	209
5.8	6.38	5.18	-11.37	-16.0	1.37	1.53	-19.83	-19.44	1.22	1.24	176	200
5.9	6.48	5.29	-15.76	-9.81	1.03	3.13	-23.88	-16.47	1.14	1.35	173	226
6.0	6.55	5.33	-18.02	-9.04	1.04	3.36	-24.61	-20.02	1.13	1.22	167	221
6.1	6.52	5.48	-17.90	-9.49	0.41	3.13	-19.7	-19.10	1.23	1.25	158	209
6.2	6.55	5.63	-26.06	-11.7	0.46	2.37	-16.54	-17.69	1.35	1.30	148	228
6.3	6.51	5.74	-24.98	-19.5	0.46	0.95	-14.76	-21.08	1.45	1.54	139	217
6.4	6.48	5.78	-25.01	-15.7	0.35	1.47	-13.57	-22.30	1.54	1.16	130	202
6.5	6.42	5.84	-27.52	-13.0	0.35	2.00	-12.46	-18.38	1.62	1.27	121	210
6.6	6.41	6.09	-27.12	-14.2	0.36	1.69	-11.57	-19.74	1.72	1.23	113	218
6.7	6.40	6.17	-30.91	-16.9	0.24	1.22	-11.14	-20.35	1.77	1.21	109	204
6.8	6.42	6.13	-28.84	-19.8	0.30	0.88	-10.91	-18.24	1.80	1.28	106	211
6.9	6.38	6.21	-35.30	-20.6	0.14	0.79	-10.71	-18.44	1.82	1.27	103	218
7.0	6.39	6.31	-31.27	-19.1	0.23	0.94	-10.56	-20.16	1.84	1.22	102	210

6.3 Polygonal Spiral Antenna with Interpolated Last Turns

6.3.1 Antenna Geometry

In another variation of the polygonal spiral antenna model, we have modified every last turn of each set of n-sided polygons. Each arm of the spiral antenna consists of 16 turns with 4 turns of n-sided polygons. Here, each 4 turns are such that instead of a regular n-sided polygon, the 4th turn is an n-sided polygon interpolated from an 2^n-sided to a 2^{n-1}-sided polygon. The spiral curve and the corresponding fabricated antenna are shown in Figure 6-27. The computer code used to generate the spiral curve is included in Appendix A.

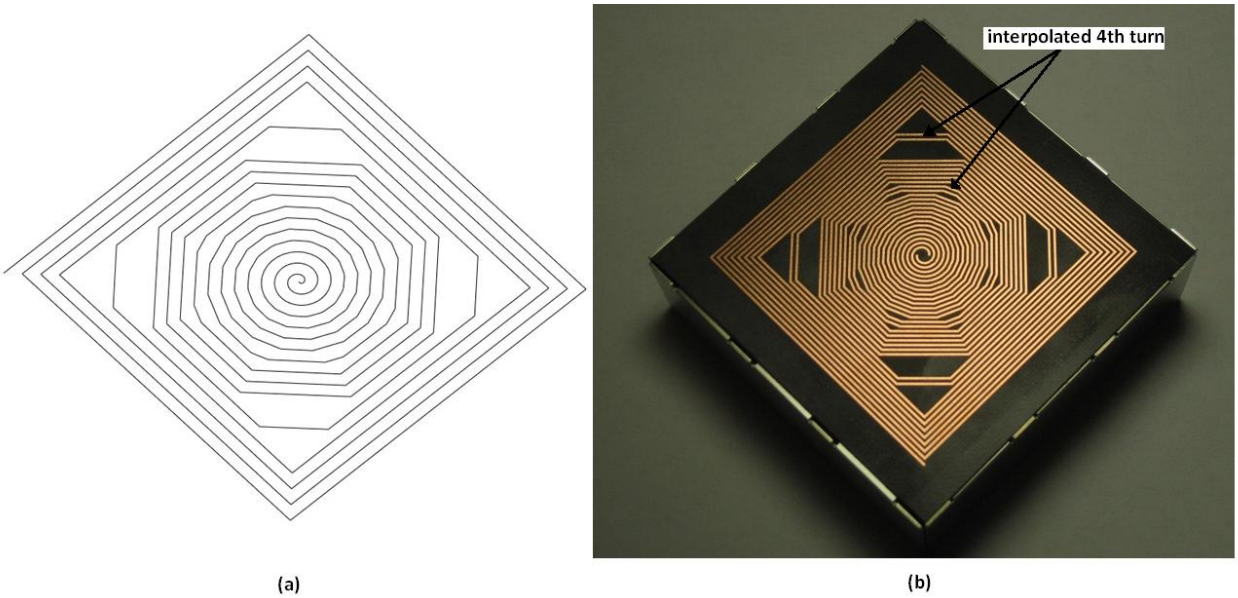

Figure 6-27: (a) Spiral Curve (b) Antenna Model

6.3.2 Results

Gain

The polar plots for gain (dB) for principal planes $\phi = 0^\circ$ and $\phi = 90^\circ$ and a diagonal cut $\phi = 45^\circ$ are shown in Figures 6-28, 6-29, 6-30, 6-31, 6-32 and 6-33. The antenna demonstrates sufficiently high and stable gains, low sidelobes and no splits in the main beam across the bandwidth.

Axial Ratio

In this modification of the polygonal spiral antenna, we were able to observe improvements in axial ratio performance in the vicinity of 5 GHz. However, the low frequency axial ratios at 2-2.6 GHz and at 4.8-5.1 GHz remained slightly above 3 dB. The axial ratio remained $\leq$ 3dB for 95% of the 2-18 GHz bandwidth. 6-34 demonstrates the overall axial ratio performance for the polygonal spiral with last interpolated turn antenna model.

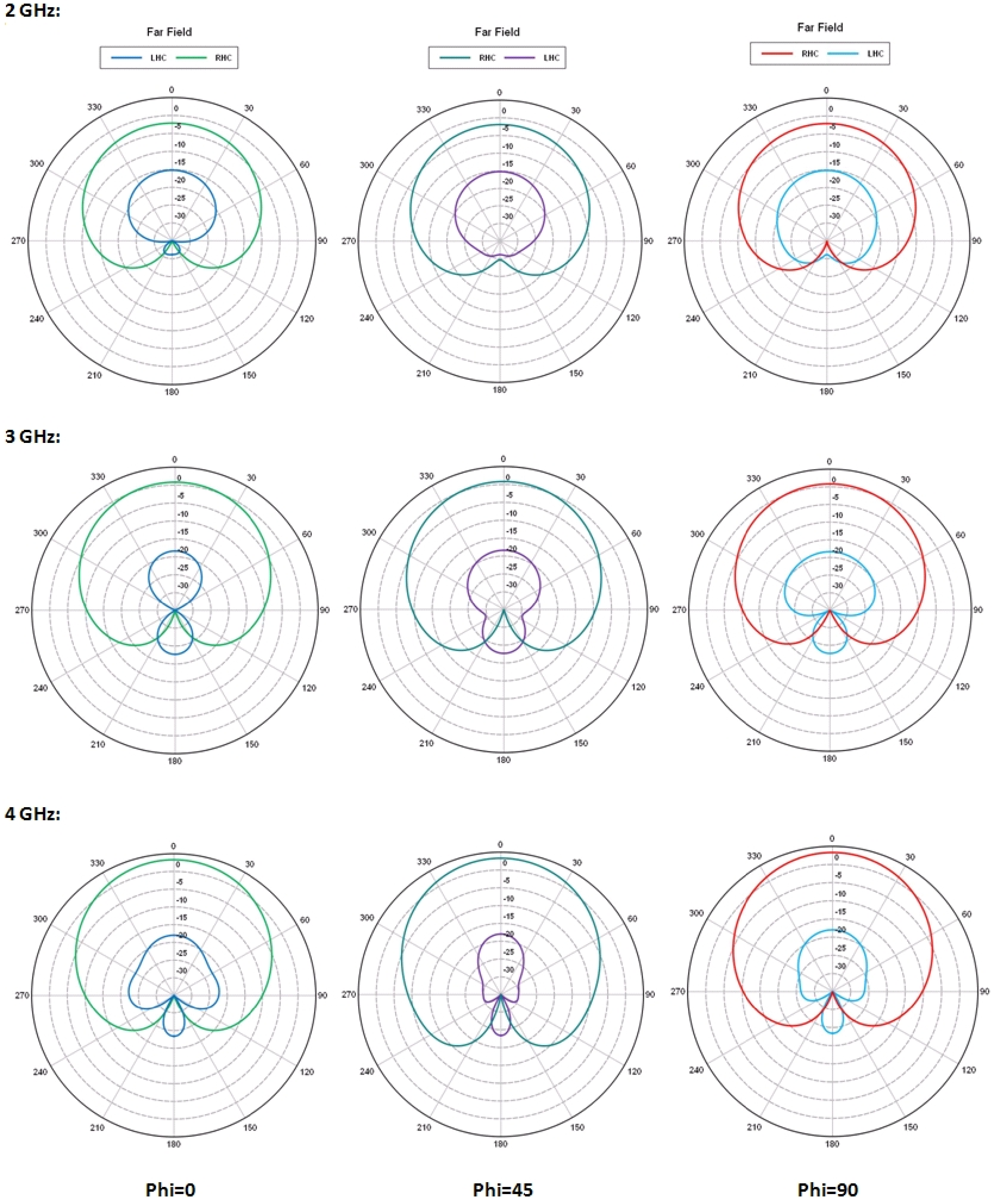

Figure 6-28: Gain (dB) for principal planes $\phi = 0°$, a diagonal cut $\phi = 45°$ and $\phi = 90°$ at 2, 3 and 4 GHz

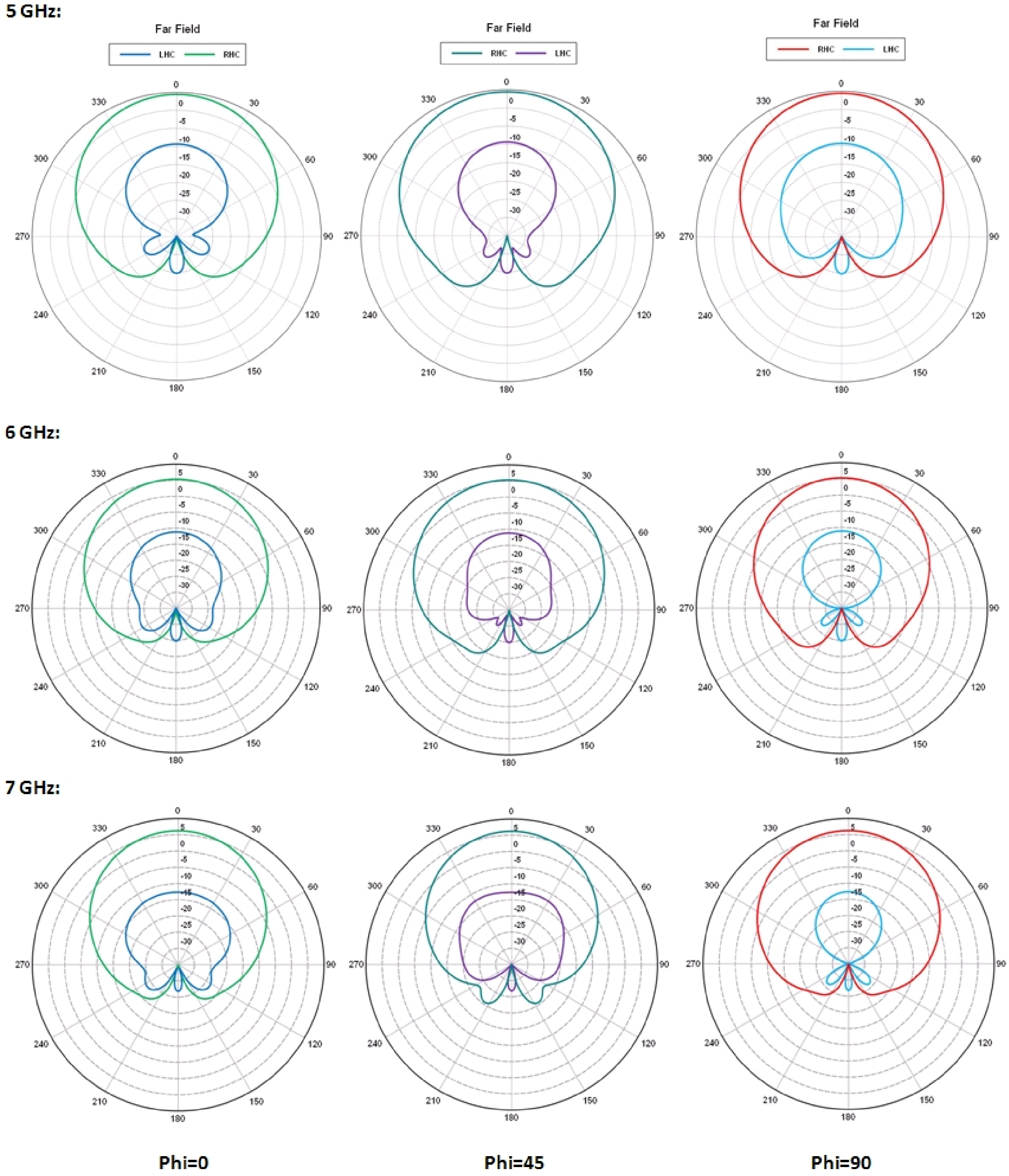

Figure 6-29: Gain (dB) for principal planes $\phi = 0°$, a diagonal cut $\phi = 45°$ and $\phi = 90°$ at 5, 6 and 7 GHz

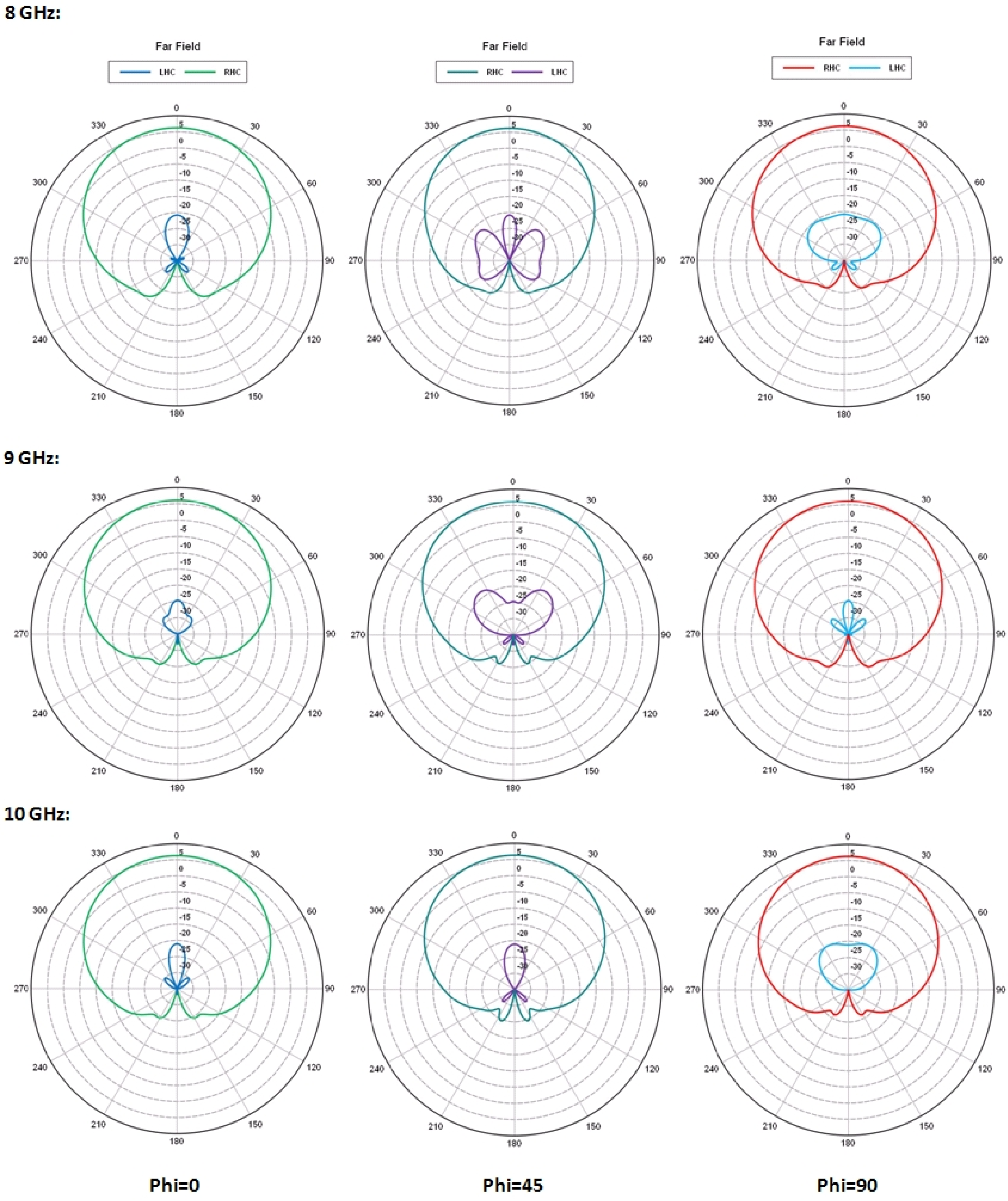

Figure 6-30: Gain (dB) for principal planes $\phi = 0°$, a diagonal cut $\phi = 45°$ and $\phi = 90°$ at 8, 9 and 10 GHz

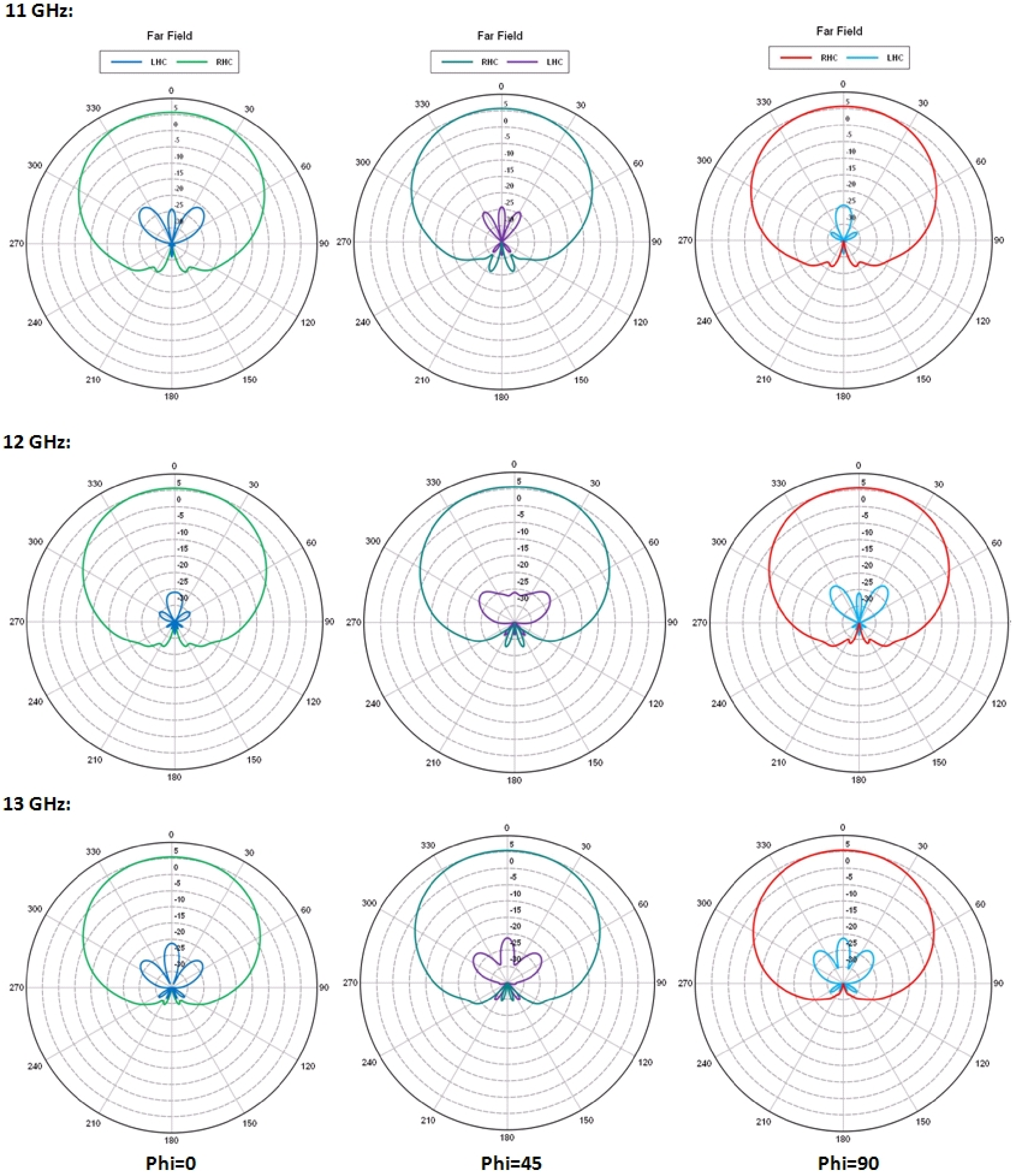

Figure 6-31: Gain (dB) for principal planes $\phi = 0°$, a diagonal cut $\phi = 45°$ and $\phi = 90°$ at 11, 12 and 13 GHz

14 GHz:

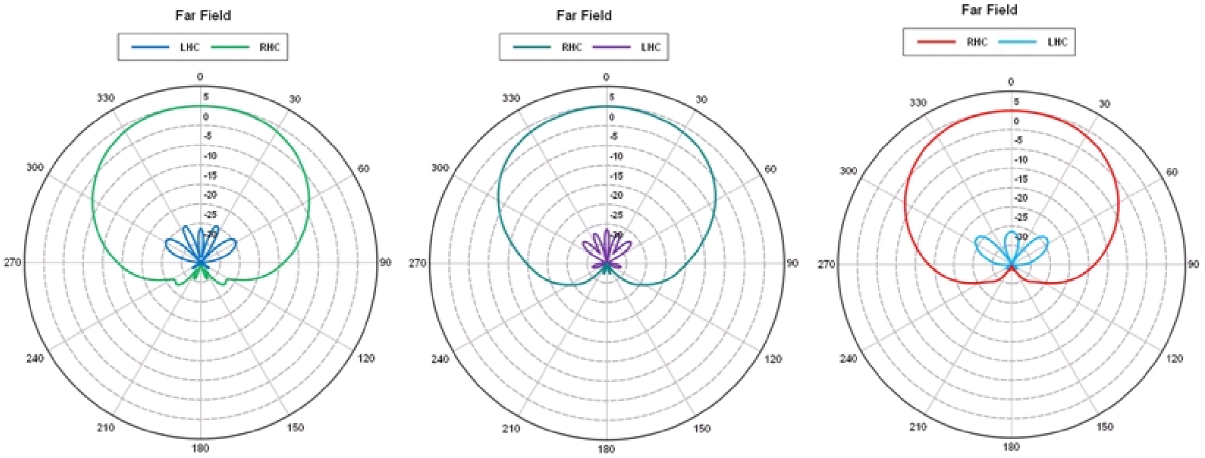

15 GHz:

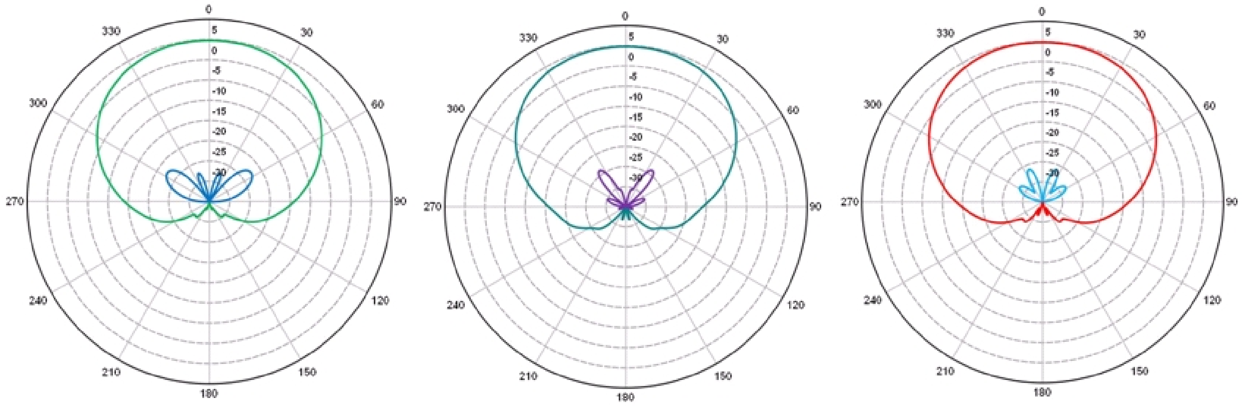

16 GHz:

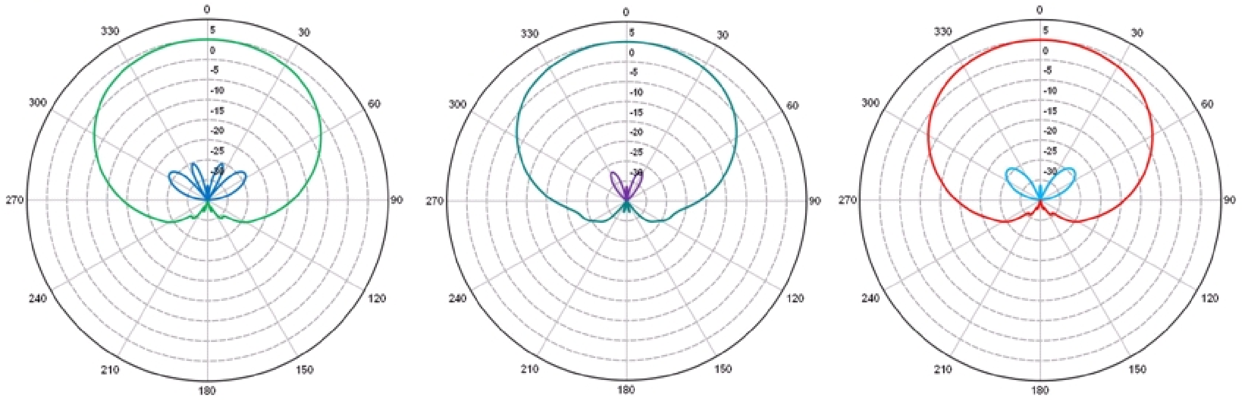

Phi=0 **Phi=45** **Phi=90**

Figure 6-32: Gain (dB) for principal planes $\phi = 0°$, a diagonal cut $\phi = 45°$ and $\phi = 90°$ at 14, 15 and 16 GHz

17 GHz:

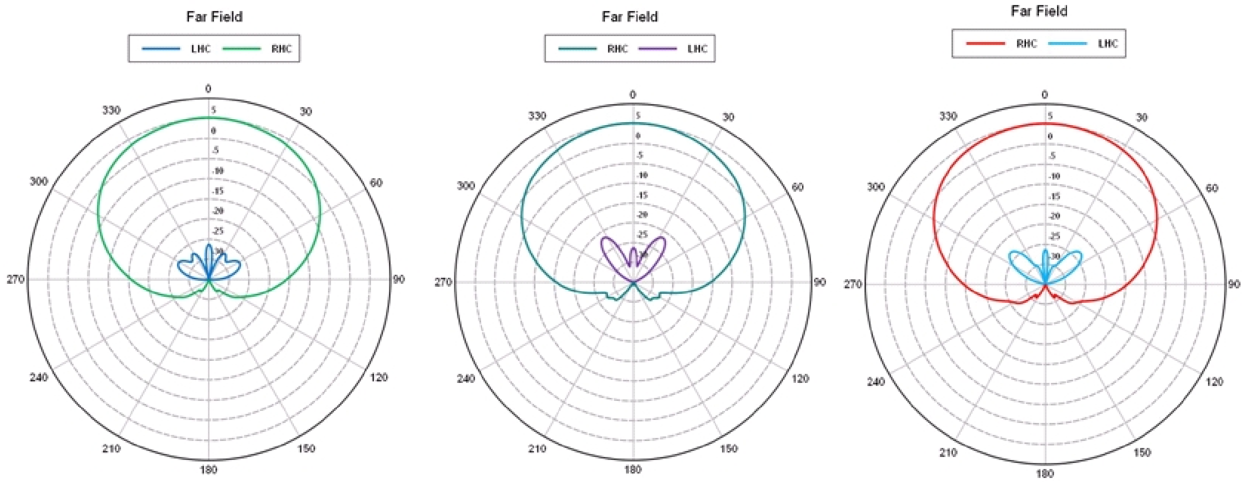

18 GHz:

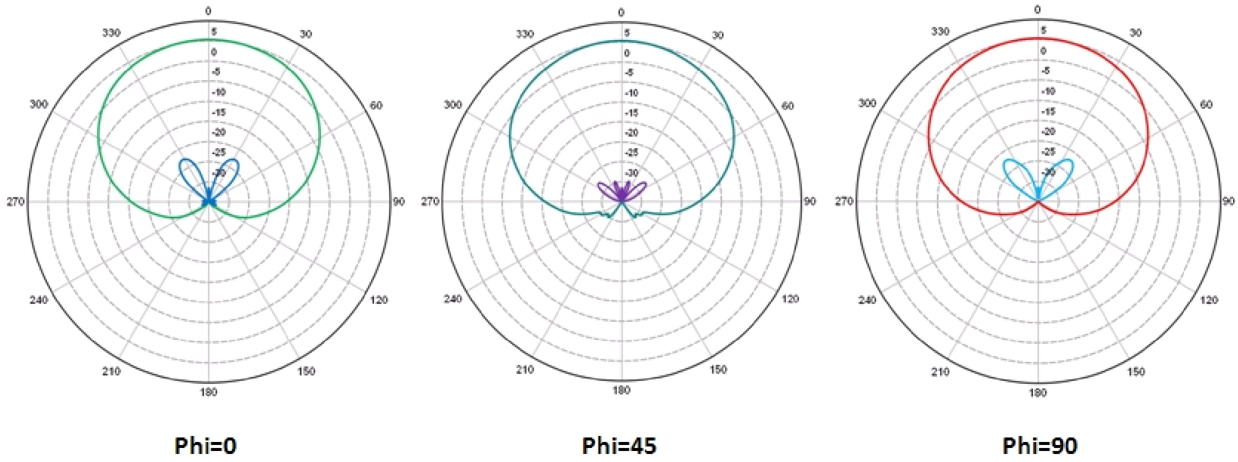

Figure 6-33: Gain (dB) for principal planes $\phi = 0°$, a diagonal cut $\phi = 45°$ and $\phi = 90°$ at 17 and 18 GHz

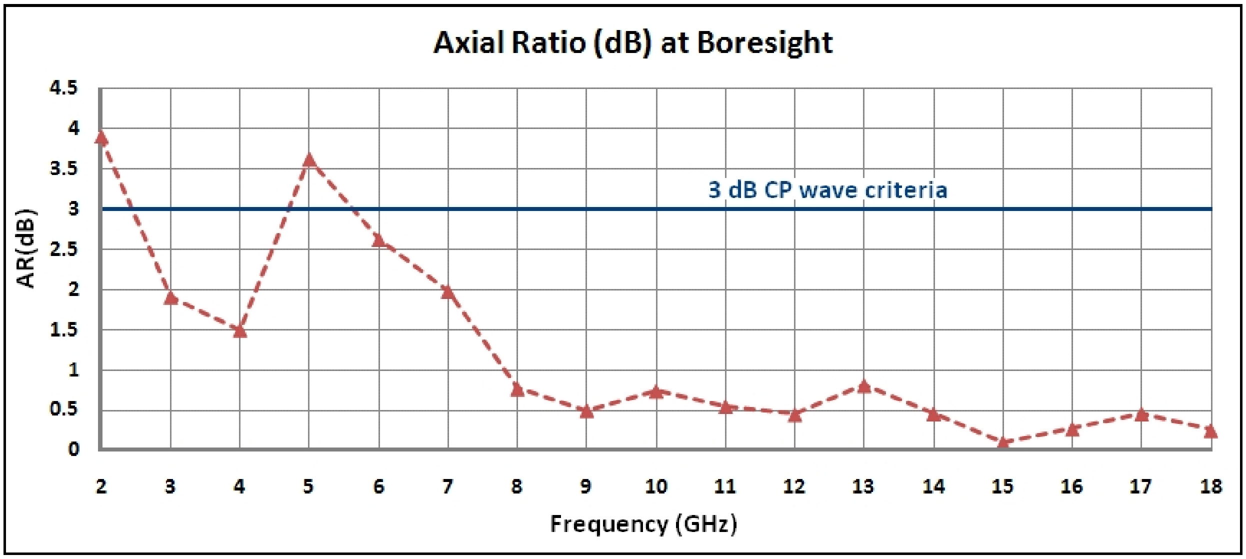

Figure 6-34: Axial Ratio (dB) vs. Frequency (GHz)

S11

Figure 6-35shows the reflection coefficient at the antenna input port assuming matched conditions. The results show that the reflection coefficient is efficiently minimized to adequate levels across the bandwidth.

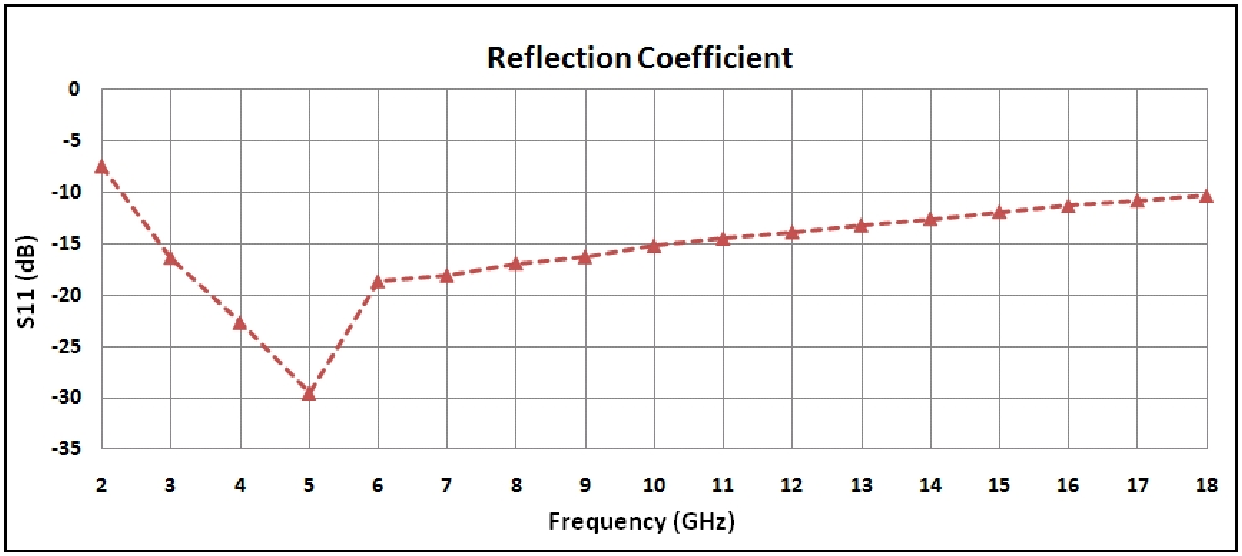

Figure 6-35: S11 (dB) vs. Frequency (GHz

Input Impedance

Figure 6-36 shows the input impedance to the cavity-backed Archimedean spiral antenna. The input impedance remains fairly consistent over operational bandwidth.

VSWR

Figure 6-37 shows the VSWR performance of the cavity-backed spiral antenna. The VSWR is referenced to 188Ω and is less than 2.5:1 for the entire bandwidth of operation, indicating a fairly good design.

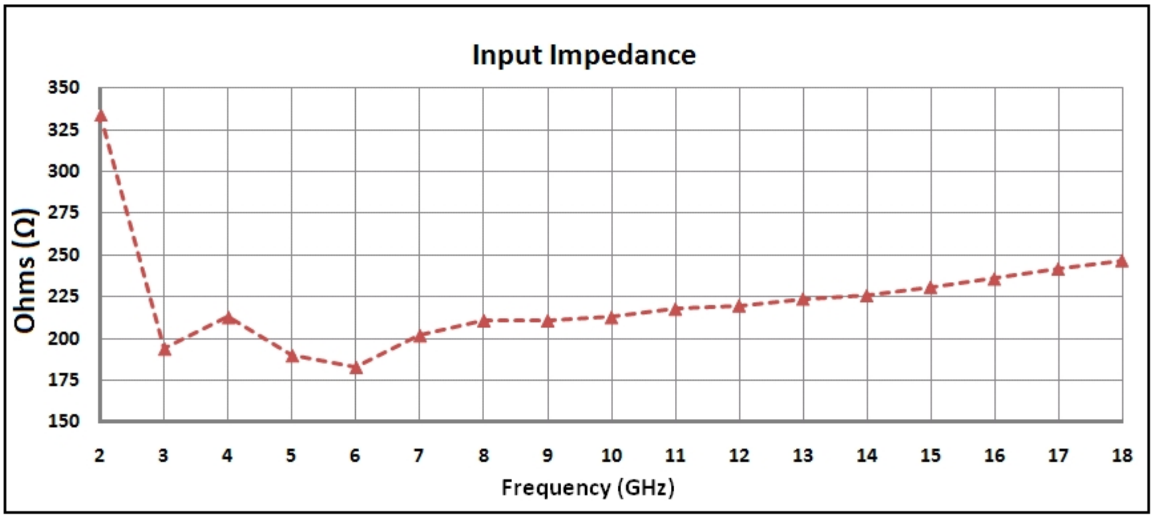

Figure 6-36: Input Impedance vs. Frequency (GHz)

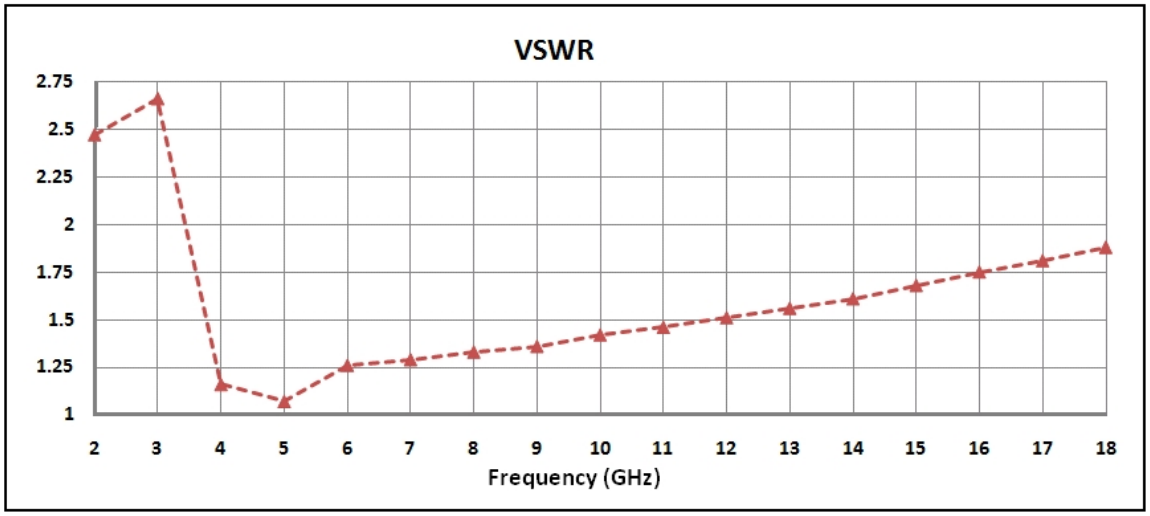

Figure 6-37: VSWR vs. Frequency (GHz)

6.3.3 Discussion

Performance Comparison of Polygonal Spiral with Circular and Square Spiral

Table 6.7 demonstrates the performance comparison of a polygonal spiral with interpolated last turns and a circular spiral from 2-18 GHz at 1 GHz intervals.

Table 6.8 demonstrates the performance comparison of a polygonal spiral with interpolated last turn and a square spiral from 2-18 GHz at 2 GHz intervals.

Table 6.7: BORESIGHT RHC AND LHC GAIN, AXIAL RATIO, S11, VSWR, AND INPUT IMPEDANCE COMPARISON OF CIRCULAR AND POLYGONAL SPIRAL ANTENNA WITH LAST INTERPOLATED TURNS

f(GHz)	Gain (dB)				AR(dB)		S11(dB)		VSWR		Input Ω	
	RHC		LHC									
	Circ.	Poly.	Circ.	Poly.	Circ.	Poly.	Circ.	Poly.	Circ.	Poly.	Circ.	Poly.
2	-2.22	-2.12	-7.26	-15.2	11.00	3.90	-6.73	-7.47	2.71	2.47	70.3	334
3	1.22	0.81	-12.7	-18.4	3.56	1.91	-14.1	-16.35	1.49	2.66	127	194
4	3.79	3.30	-8.56	-18.0	4.27	1.50	-13.0	-22.67	1.58	1.16	119	213
5	5.47	4.41	-6.94	-9.34	4.05	3.62	-11.4	-29.55	1.54	1.07	125	190
6	6.55	5.30	-18.02	-11.2	1.04	2.62	-24.61	-18.66	1.13	1.26	167	183
7	6.58	6.18	-32.5	-12.7	0.19	1.98	-13.2	-18.08	1.56	1.29	121	202
8	6.52	6.22	-36.0	-20.8	0.13	0.77	-13.9	-16.90	1.50	1.33	125	211
9	6.04	6.16	-40.9	-24.7	0.08	0.50	-14.2	-16.28	1.48	1.36	127	211
10	5.24	6.27	-52.3	-21.1	0.02	0.74	-12.6	-15.19	1.61	1.42	117	213
11	4.09	5.70	-49.2	-24.3	0.04	0.55	-9.08	-14.50	2.08	1.46	91.7	218
12	4.01	5.61	-50.2	-26.1	0.03	0.45	-9.81	-13.88	1.95	1.51	97	220
13	4.55	5.40	-54.5	-21.3	0.02	0.81	-10.1	-13.20	1.90	1.56	101	224
14	4.96	4.91	-48.8	-26.4	0.04	0.46	-10.6	-12.59	1.83	1.61	105	226
15	5.15	4.77	-53.3	-40.3	0.02	0.10	-11.0	-11.88	1.79	1.68	106	231
16	5.46	4.98	-57.0	-31.3	0.01	0.27	-11.6	-11.31	1.72	1.75	110	236
17	5.58	5.18	-86.5	-26.3	0.00	0.46	-11.8	-10.79	1.69	1.81	111	242
18	5.66	5.28	-64.9	-31.5	0.01	0.25	-12.5	-10.33	1.62	1.88	117	247

Table 6.8: BORESIGHT RHC AND LHC GAIN, AXIAL RATIO, S11, VSWR, AND INPUT IMPEDANCE COMPARISON OF SQUARE AND POLYGONAL SPIRAL ANTENNA WITH LAST INTERPOLATED TURNS

f(GHz)	Gain (dB)				AR(dB)		S11(dB)		VSWR		Input Ω	
	RHC		LHC									
	Sqr.	Poly.	Sqr.	Poly.	Sqr.	Poly.	Sqr.	Poly.	Sqr.	Poly.	Sqr.	Poly.
2	-1.54	-2.12	-18.1	-15.2	2.59	3.90	-28.1	-7.47	1.08	2.47	201	334
4	3.23	3.30	-13.3	-18.0	2.6	1.50	-25.8	-22.67	1.11	1.16	208	213
6	5.53	5.30	-8.97	-11.2	3.31	2.62	-28.4	-18.66	1.08	1.26	203	183
8	6.23	6.22	-5.11	-20.8	4.83	0.77	-22.6	-16.90	1.16	1.33	204	211
10	5.51	6.27	-5.63	-21.1	4.95	0.74	-23.9	-15.19	1.14	1.42	211	213
12	4.19	5.61	-5.36	-26.1	6.01	0.45	-24.9	-13.88	1.12	1.51	207	220
14	5.05	4.91	-4.73	-26.4	5.85	0.46	-21	-12.59	1.20	1.61	214	226
16	5.84	4.98	-3.86	-31.3	5.9	0.27	-18.9	-11.31	1.26	1.75	219	236
18	4.82	5.28	-7.04	-31.5	4.53	0.25	-18	-10.33	1.29	1.88	221	247

Performance Analysis of Polygonal Spiral at Lower Frequencies

To verify the axial ratio performance of the polygonal spiral antenna at lower frequencies, we simulated the model from 2-6 GHz 100 MHz intervals. Table 6.9 demonstrates the performance comparison of a polygonal spiral and a circular spiral from 2-6 GHz at 0.1 GHz intervals. The polygonal spiral shows $\geq$ 3 dB axial ratio at frequency interval 2.0-2.6 GHz, 4.8-5.1 GHz and in the vicinity of 3.8 GHz.

Table 6.9: BORESIGHT RHC AND LHC GAIN, AXIAL RATIO, S11, VSWR, AND INPUT IMPEDANCE COMPARISON OF A CIRCULAR AND POLYGONAL SPIRAL ANTENNA WITH LAST INTERPOLATED TURNS AT LOW FREQUENCIES

f(GHz)	Gain (dB)				AR(dB)		S11(dB)		VSWR		Input Ω	
	RHC		LHC									
	Circ.	Poly.	Circ.	Poly.	Circ.	Poly.	Circ.	Poly.	Circ.	Poly.	Circ.	Poly.
2	-2.22	-2.12	-7.26	-15.2	11.00	3.90	-6.73	-7.47	2.71	2.47	70.3	334
2.1	-0.87	-2.17	-9.35	-15.5	6.88	3.83	-10.8	-7.44	1.81	2.48	109	352
2.2	-0.26	-0.92	-12.0	-14.0	4.61	3.93	-13.5	-23.83	1.53	1.12	125	213
2.3	0.00	-0.62	-14.1	-14.0	3.48	3.79	-14.5	-17.44	1.46	2.10	129	149
2.4	0.11	-0.72	-14.9	-16.6	3.11	2.82	-15.1	-13.11	1.43	1.57	132	209
2.5	0.15	-0.65	-14.9	-14.6	3.11	3.52	-15.0	-13.18	1.43	1.56	132	292
2.6	0.28	0.01	-14.4	-21.9	3.25	1.73	-13.9	-24.63	1.50	1.17	126	213
2.7	0.57	0.20	-13.6	-18.2	3.46	2.09	-12.8	-24.63	1.60	1.12	118	211
2.8	0.84	0.35	-13.0	-21.5	3.59	1.40	-12.4	-27.66	1.63	1.09	115	180
2.9	0.99	0.65	-12.8	-31.0	3.61	0.46	-12.7	-20.80	1.60	1.20	118	166
3.0	1.22	0.81	-12.7	-18.4	3.56	1.91	-14.1	-16.35	1.49	2.66	127	194
3.1	1.68	0.98	-11.8	-17.0	3.73	2.21	-15.7	-16.85	1.39	1.34	135	228
3.2	1.99	1.27	-11.0	-16.0	3.98	2.41	-15.8	-17.99	1.39	1.29	136	239
3.3	2.04	1.53	-10.8	-14.6	4.01	2.74	-14.0	-24.56	1.50	1.13	128	207
3.4	2.27	1.76	-10.8	-14.5	3.91	2.69	-12.5	-24.17	1.62	1.13	117	173
3.5	2.64	2.03	-10.0	-14.6	4.12	2.58	-12.0	-19.30	1.67	1.24	113	192
3.6	2.82	2.31	-9.48	-15.0	4.30	2.39	-12.5	-19.45	1.63	1.24	116	195
3.7	3.12	2.41	-9.50	-16.0	4.14	2.09	-14.3	-17.01	1.48	1.33	130	217
3.8	3.56	2.77	-8.93	-10.6	4.20	3.77	-15.4	-21.60	1.41	1.18	135	204
3.9	3.72	2.92	-8.33	-13.7	4.43	2.59	-15.1	-21.80	1.42	1.42	132	208
4.0	3.79	3.30	-8.56	-18.0	4.27	1.50	-13.0	-22.67	1.58	1.16	119	213
4.1	3.75	3.45	-8.26	-12.5	4.27	2.80	-11.7	-25.72	1.74	1.11	109	194
4.2	3.94	3.66	-8.41	-12.4	4.24	2.78	-14.1	-19.90	1.70	1.22	111	213
4.3	4.43	3.88	-7.97	-13.2	4.44	2.46	-15.6	-22.23	1.49	1.17	127	211
4.4	4.62	3.88	-7.41	-13.2	4.29	2.46	-12.9	-22.23	1.40	1.17	135	211
4.5	4.62	4.16	-7.70	-17.9	4.21	1.38	-11.2	-18.84	1.59	1.26	122	225
4.6	4.81	4.10	-7.67	-13.1	4.37	2.42	-11.4	-25.57	1.76	1.11	108	200
4.7	4.94	4.34	-7.23	-13.5	4.22	2.24	-13.4	-21.74	1.74	1.18	108	215
4.8	5.14	4.38	-7.32	-10.7	4.13	3.10	-15.1	-25.35	1.54	1.11	123	195
4.9	5.48	4.22	-7.17	-9.18	4.24	3.77	-13.4	-22.14	1.42	1.17	132	210
5.0	5.47	4.41	-6.94	-9.34	4.05	3.62	-11.4	-29.55	1.54	1.07	125	190
5.1	5.02	4.40	-7.70	-8.94	4.09	3.80	-8.94	-19.49	2.11	1.24	111	191
5.2	5.27	4.54	-7.67	-11.2	4.05	2.87	-7.93	-18.85	2.34	1.99	94	215
5.3	5.24	4.75	-7.57	-12.3	3.73	2.46	-7.93	-23.77	2.36	1.14	98	200
5.4	5.66	4.84	-8.25	-10.9	3.51	2.85	-9.24	-22.03	2.04	1.17	110	206
5.5	5.99	4.87	-8.35	-10.5	3.37	2.99	-12.0	-23.73	1.67	1.14	134	184
5.6	6.11	4.87	-8.35	-11.4	2.82	2.68	-14.74	-17.46	1.45	1.31	157	191
5.7	6.35	4.95	-9.75	-13.1	2.31	2.17	-16.96	-17.15	1.33	1.32	172	217
5.8	6.38	5.18	-11.37	-29.8	1.37	0.31	-19.83	-32.23	1.22	1.22	176	213
5.9	6.48	5.30	-15.76	-15.0	1.03	1.68	-23.88	-24.09	1.14	1.13	173	196
6.0	6.55	5.30	-18.02	-11.2	1.04	2.62	-24.61	-18.66	1.13	1.26	167	183

6.4 Polygonal Spiral Antenna with Gradually Transitioning Arms

6.4.1 Antenna Geometry

In this model of the of the polygonal spiral antenna model, each arm of the spiral antenna consists of 16 turns with sets of 4 turns of n-sided polygons. However, each 4 turns are such that the first turn is a regular n-sided polygon with n-equal sides, then the consecutive turns are n-sided polygons gradually transitioning from a 2^n-sided to a 2^{n-1} polygon. The the spiral curve and the corresponding fabricated antenna is shown in Figure 6-38. The computer code used to generate the spiral curve is included in Appendix A.

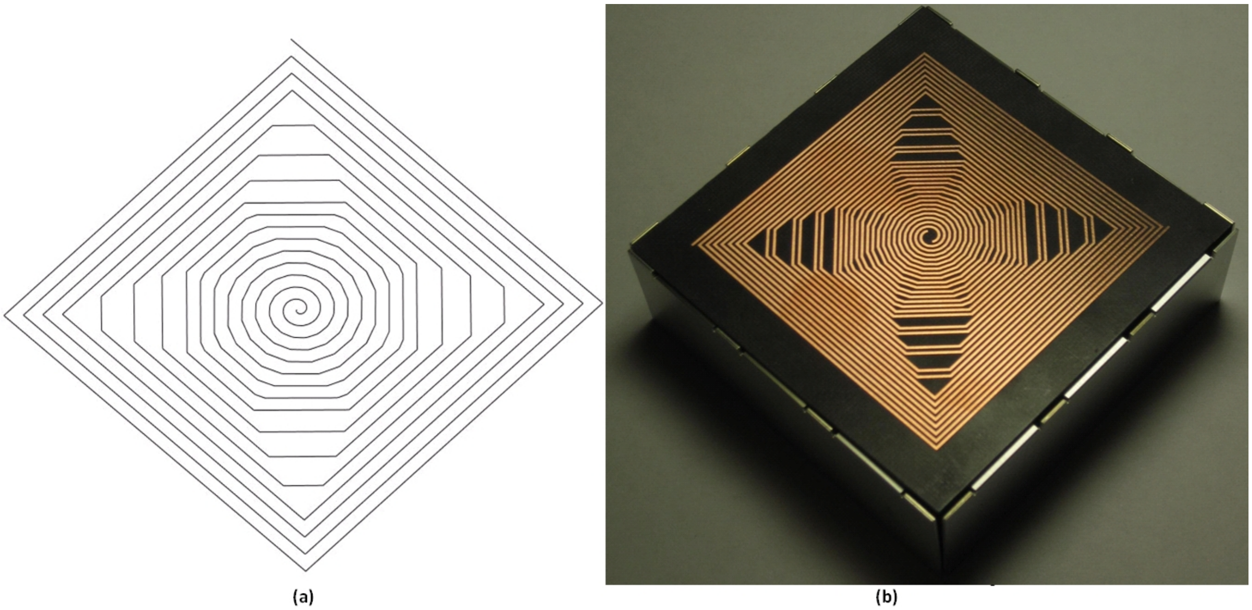

Figure 6-38: (a) Spiral Curve (b) Antenna Model

6.4.2 Results

Gain

The polar plots for gain (dB) for principal planes $\phi = 0°$ and $\phi = 90°$ and a diagonal cut $\phi = 45°$ are shown in Figures 6-39, 6-40, 6-41, 6-42, 6-43 and 6-44. The antenna demonstrates sufficiently high and stable gains, low sidelobes and no splits in the main beam across the bandwidth.

Axial Ratio

In this modification of the polygonal spiral antenna, we were able to observe very good low-frequency and overall axial ratio performance. The axial ratios at 2.1 GHz, 4.9-5.0 GHz and 5.3-5.7 GHz remained slightly above 3 dB. The axial ratio remained $\leq$ 3 dB for 97.5% of the 2-18 GHz bandwidth. Figure 6-45 demonstrates the overall axial ratio for the polygonal spiral antenna with gradually transitioning arms.

S11

Figure 6-46 shows the reflection coefficient at the antenna input port assuming matched conditions. The results show that the reflection coefficient is efficiently minimized to adequate levels across the bandwidth.

Input Impedance

Figure 6-47 shows the input impedance to the cavity-backed Archimedean spiral antenna. The input impedance remains fairly consistent over operational bandwidth.

VSWR

Figure 6-48 shows the VSWR performance of the cavity-backed spiral antenna. The VSWR is referenced to 188Ω and is approximately less than 2:1 for the entire bandwidth of operation, indicating a good VSWR performance for this configuration of the polygonal spiral antenna.

6.4.3 Discussion

Performance Comparison of Polygonal Spiral with Circular and Square Spiral

Table 6.10 demonstrates the performance comparison of a polygonal spiral with gradually transitioning arms and a circular spiral from 2-18 GHz at 1 GHz intervals.

Table 6.10: BORESIGHT RHC AND LHC GAIN, AXIAL RATIO, S11, VSWR, AND INPUT IMPEDANCE COMPARISON OF CIRCULAR AND POLYGONAL SPIRAL ANTENNA WITH GRADUALLY TRANSITIONING ARMS

f(GHz)	Gain (dB)				AR(dB)		S11(dB)		VSWR		Input Ω	
	RHC		LHC									
	Circ.	Poly.	Circ.	Poly.	Circ.	Poly.	Circ.	Poly.	Circ.	Poly.	Circ.	Poly.
2	-2.220	-1.49	-7.26	-16.9	11.00	2.97	-6.73	-13.87	2.71	1.51	70.3	152
3	1.220	0.83	-12.7	-16.8	3.56	2.29	-14.1	-21.85	1.49	1.18	127	221
4	3.79	3.21	-8.56	-13.9	4.27	2.44	-13.0	-22.63	1.58	1.16	119	211
5	5.47	4.28	-6.94	-8.4	4.05	4.12	-11.4	-17.40	1.54	1.31	125	199
6	6.55	5.26	-18.02	-13.2	1.04	2.09	-24.61	-16.17	1.13	1.37	167	209
7	6.58	6.01	-32.5	-10.6	0.19	2.59	-13.2	-16.18	1.56	1.37	121	205
8	6.52	6.19	-36.0	-12.3	0.13	2.08	-13.9	-14.52	1.50	1.46	125	228
9	6.04	6.02	-40.9	-21.3	0.08	0.75	-14.2	-14.32	1.48	1.48	127	220
10	5.24	5.94	-52.3	-21.2	0.02	0.77	-12.6	-14.19	1.61	1.48	117	221
11	4.09	5.93	-49.2	-26.1	0.04	0.44	-9.08	-13.24	2.08	1.56	91.7	224
12	4.01	5.44	-50.2	-22.8	0.03	0.68	-9.81	-12.65	1.95	1.60	97	226
13	4.55	5.17	-54.5	-37.3	0.02	0.13	-10.1	-11.84	1.90	1.69	101	232
14	4.96	4.89	-48.8	-19.5	0.04	1.05	-10.6	-11.30	1.83	1.75	105	236
15	5.15	4.89	-53.3	-37.6	0.02	0.13	-11.0	-10.63	1.79	1.83	106	243
16	5.46	4.81	-57.0	-26.4	0.01	0.48	-11.6	-10.03	1.72	1.92	110	249
17	5.58	4.96	-86.5	-28.1	0.00	0.39	-11.8	-9.55	1.69	2.00	111	257
18	5.66	5.15	-64.9	-28.6	0.01	0.36	-12.5	-9.14	1.62	2.07	117	264

Table 6.11 demonstrates the performance comparison of the polygonal spiral and a square spiral from 2-18 GHz at 2 GHz intervals.

Performance Analysis of Polygonal Spiral at Lower Frequencies

To verify the axial ratio performance of the polygonal spiral antenna at lower frequencies, we simulated the model from 2-6 GHz 100 MHz intervals. Table 6.12 demonstrates the performance comparison of a polygonal spiral and a circular spiral from

Table 6.11: BORESIGHT RHC AND LHC GAIN, AXIAL RATIO, S11, VSWR, AND INPUT IMPEDANCE COMPARISON OF SQUARE AND POLYGONAL SPIRAL ANTENNA WITH GRADUALLY TRANSITIONING ARMS

f(GHz)	Gain (dB)				AR(dB)		S11(dB)		VSWR		Input Ω	
	RHC		LHC									
	Sqr.	Poly.	Sqr.	Poly.	Sqr.	Poly.	Sqr.	Poly.	Sqr.	Poly.	Sqr.	Poly.
2	-1.54	-1.49	-18.1	-16.9	2.59	2.97	-28.1	-13.87	1.08	1.51	201	152
4	3.23	3.21	-13.3	-13.9	2.6	2.44	-25.8	-22.63	1.11	1.16	208	211
6	5.53	5.26	-8.97	-13.2	3.31	2.09	-28.4	-16.17	1.08	1.37	203	209
8	6.23	6.19	-5.11	-12.3	4.83	2.08	-22.6	-14.52	1.16	1.46	204	228
10	5.51	5.94	-5.63	-21.2	4.95	0.77	-23.9	-14.19	1.14	1.48	211	221
12	4.19	5.44	-5.36	-22.8	6.01	0.68	-24.9	-12.65	1.12	1.60	207	226
14	5.05	4.89	-4.73	-19.5	5.85	1.05	-21	-11.30	1.20	1.75	214	236
16	5.84	4.81	-3.86	-26.4	5.9	0.48	-18.9	-10.03	1.26	1.92	219	249
18	4.82	5.15	-7.04	-28.6	4.53	0.36	-18	-9.14	1.29	2.07	221	264

2-6 GHz at 0.1 GHz intervals. The polygonal spiral shows ≥ 3 axial ratio at frequency interval 4.9-5.0 GHz, 5.3-5.7 GHz, and in the vicinity of 2.1 GHz.

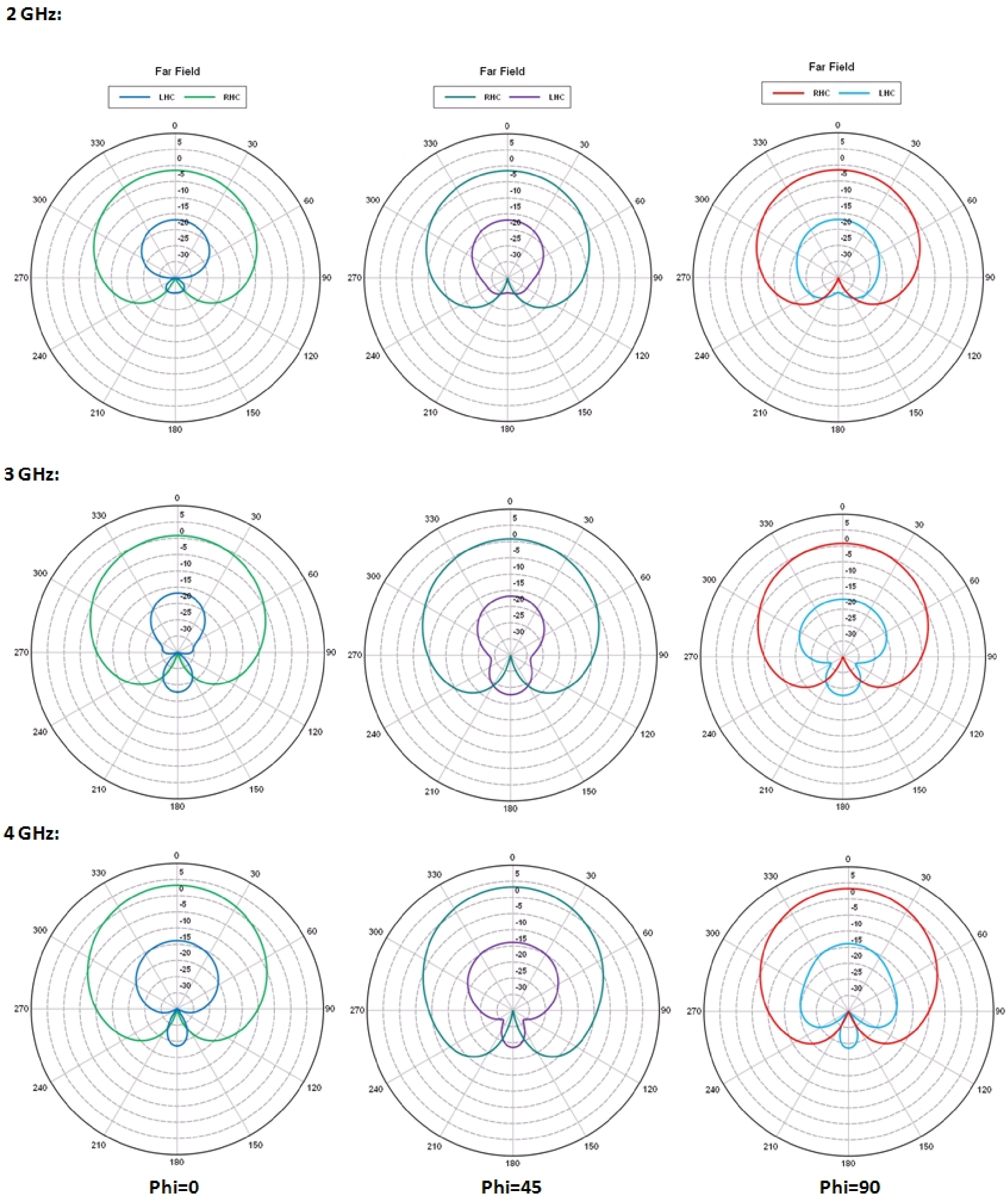

Figure 6-39: Gain (dB) for principal planes $\phi = 0°$, a diagonal cut $\phi = 45°$ and $\phi = 90°$ at 2, 3 and 4 GHz

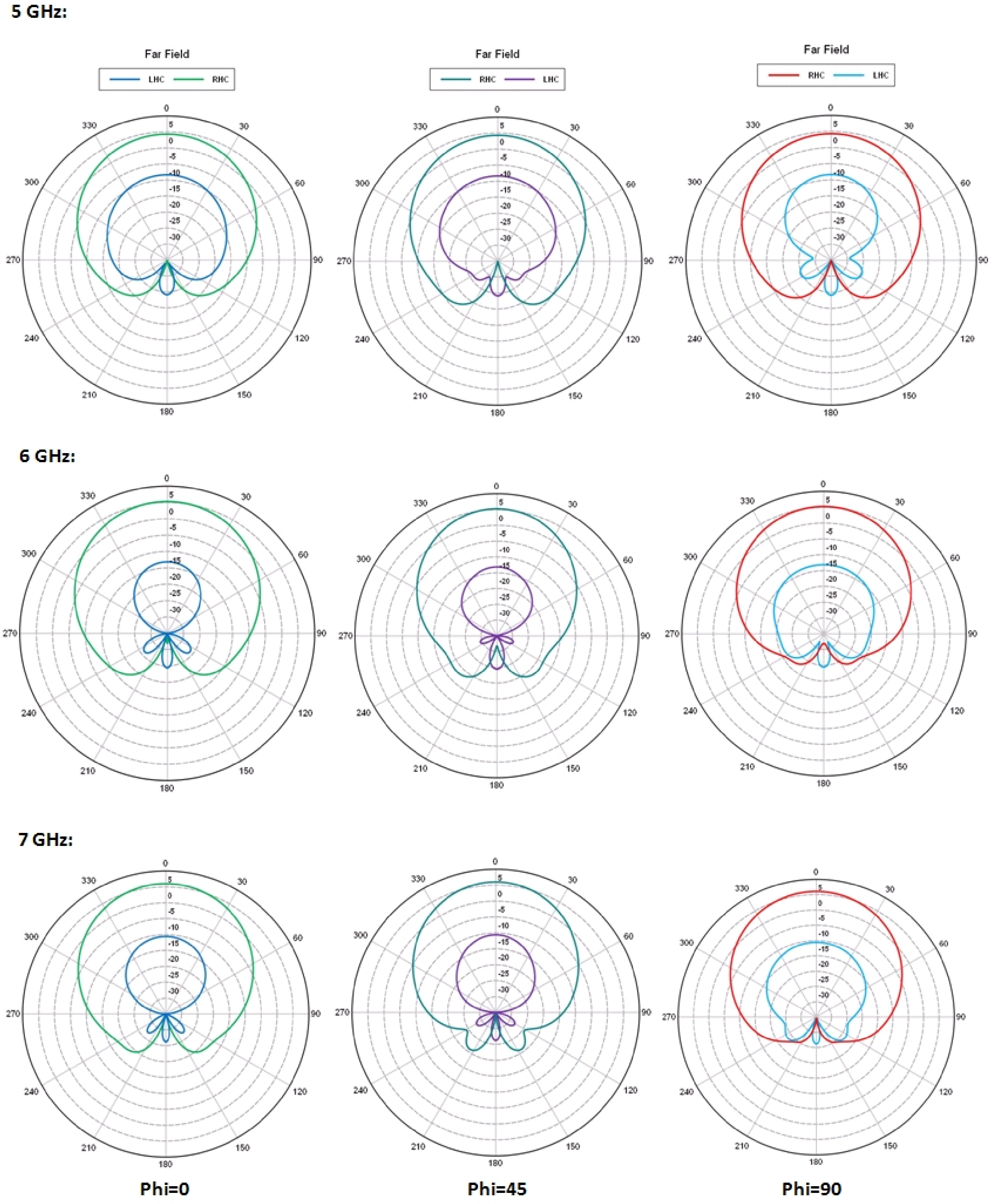

Figure 6-40: Gain (dB) for principal planes $\phi = 0°$, a diagonal cut $\phi = 45°$ and $\phi = 90°$ at 5, 6 and 7 GHz

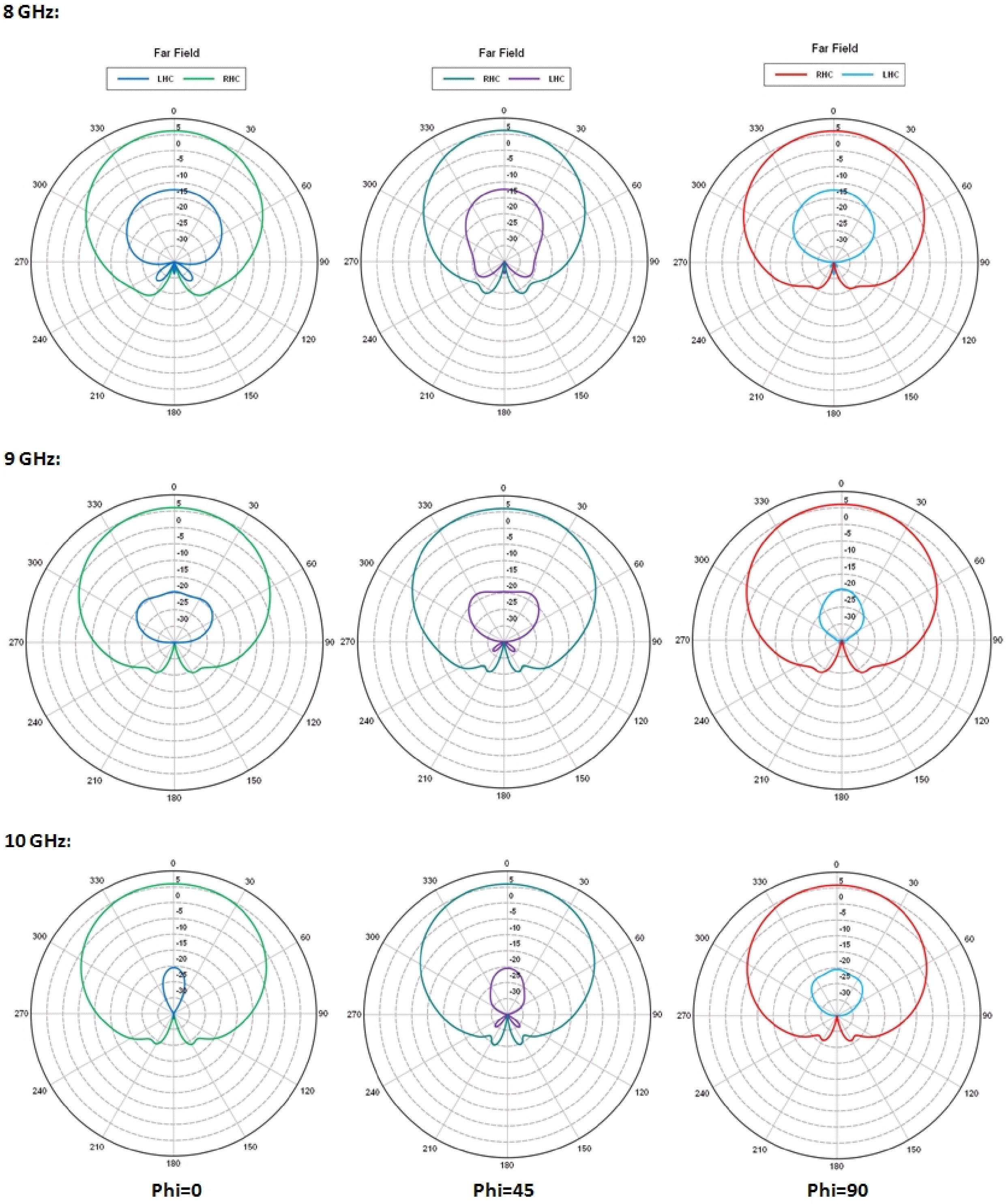

Figure 6-41: Gain (dB) for principal planes $\phi = 0°$, a diagonal cut $\phi = 45°$ and $\phi = 90°$ at 8, 9 and 10 GHz

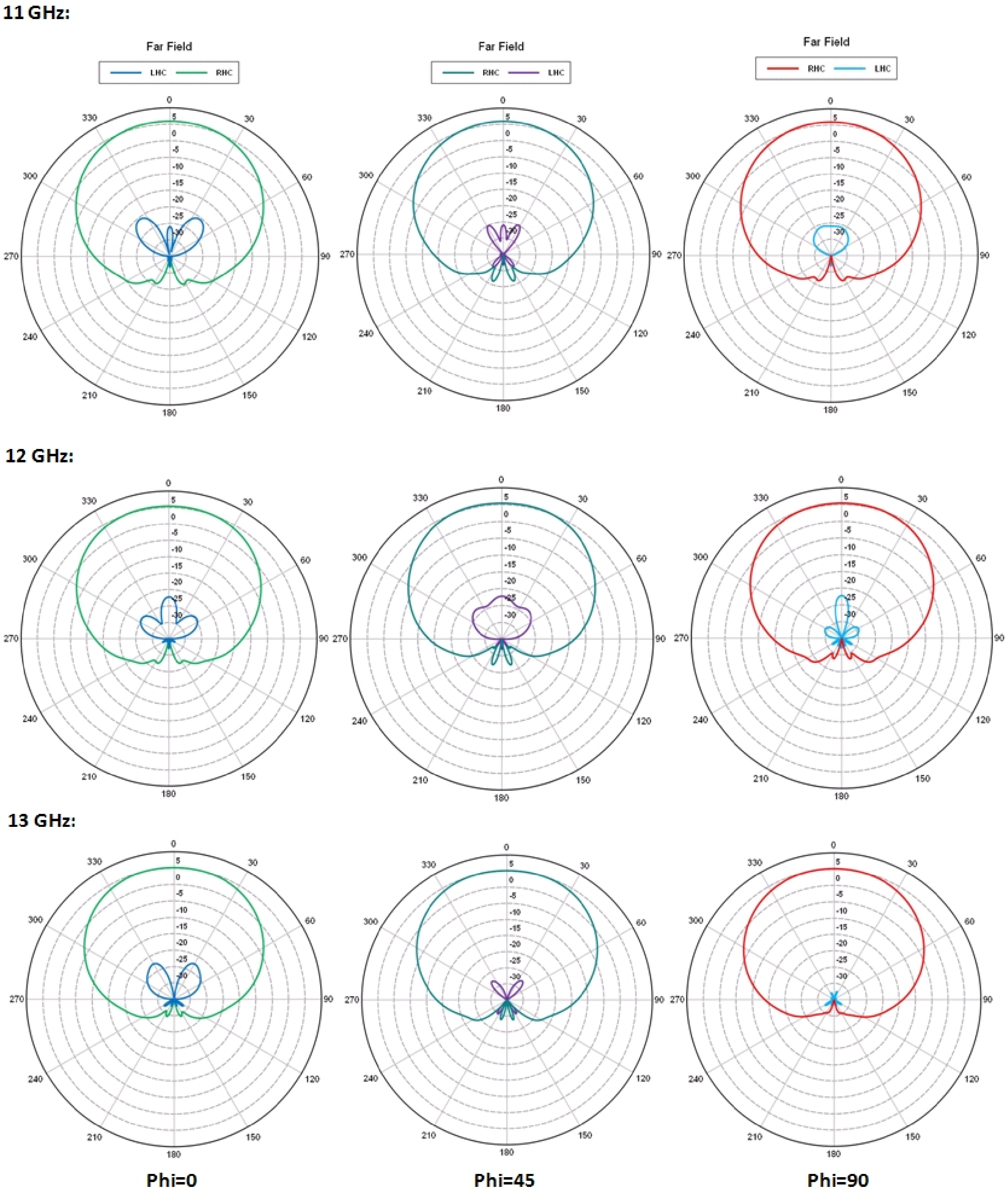

Figure 6-42: Gain (dB) for principal planes $\phi = 0°$, a diagonal cut $\phi = 45°$ and $\phi = 90°$ at 11, 12 and 13 GHz

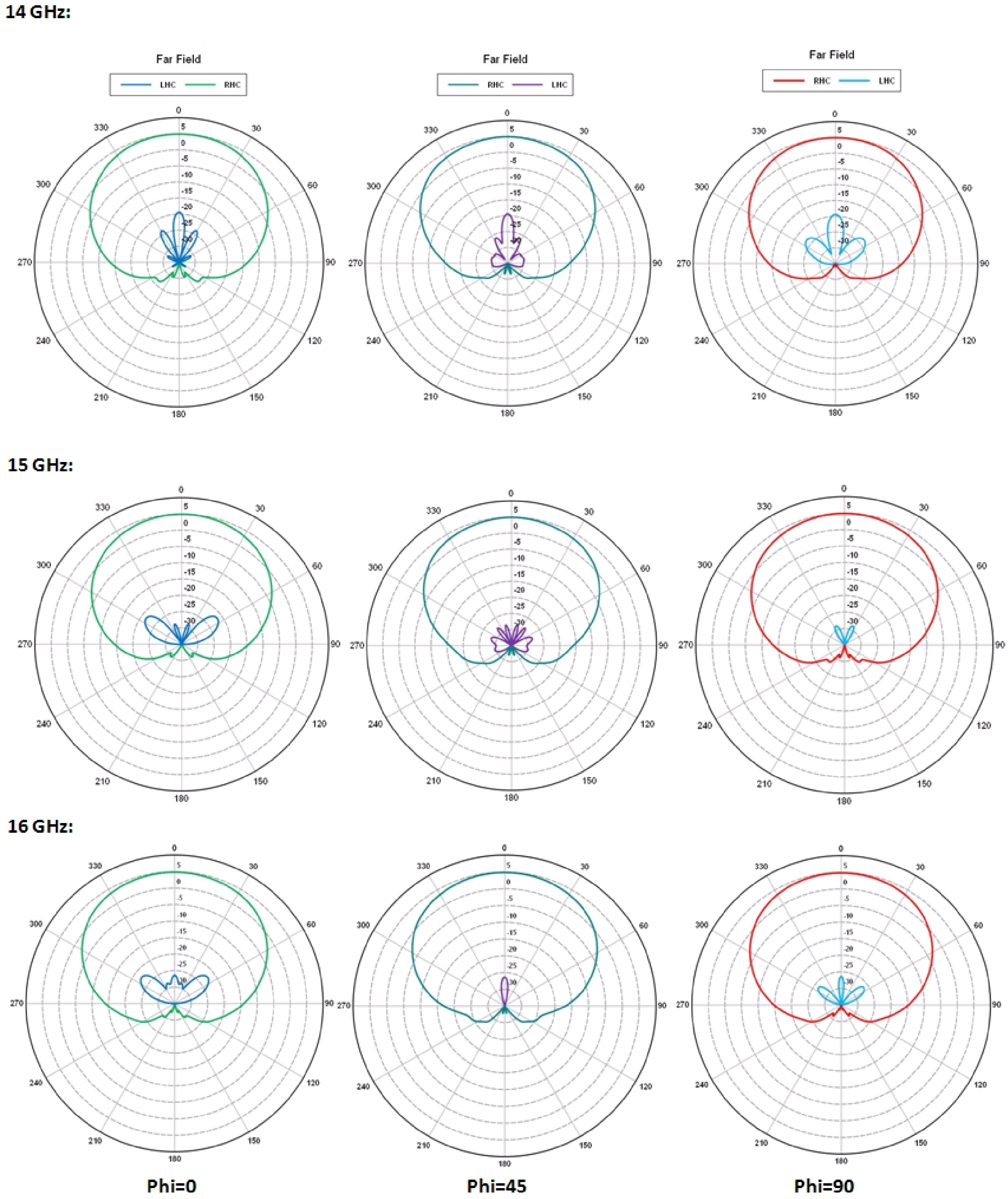

Figure 6-43: Gain (dB) for principal planes $\phi = 0°$, a diagonal cut $\phi = 45°$ and $\phi = 90°$ at 14, 15 and 16 GHz

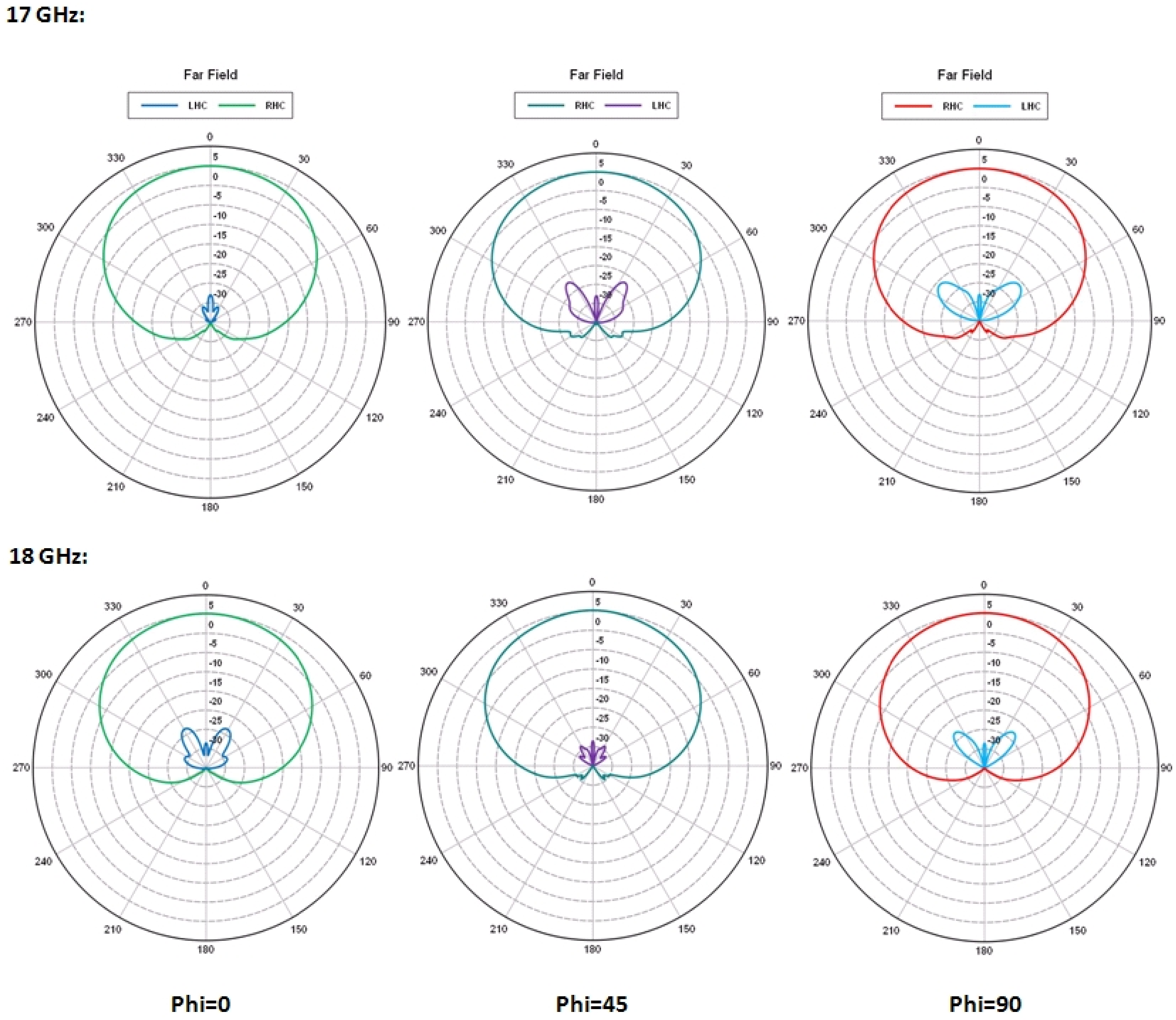

Figure 6-44: Gain (dB) for principal planes $\phi = 0°$, a diagonal cut $\phi = 45°$ and $\phi = 90°$ at 17 and 18 GHz

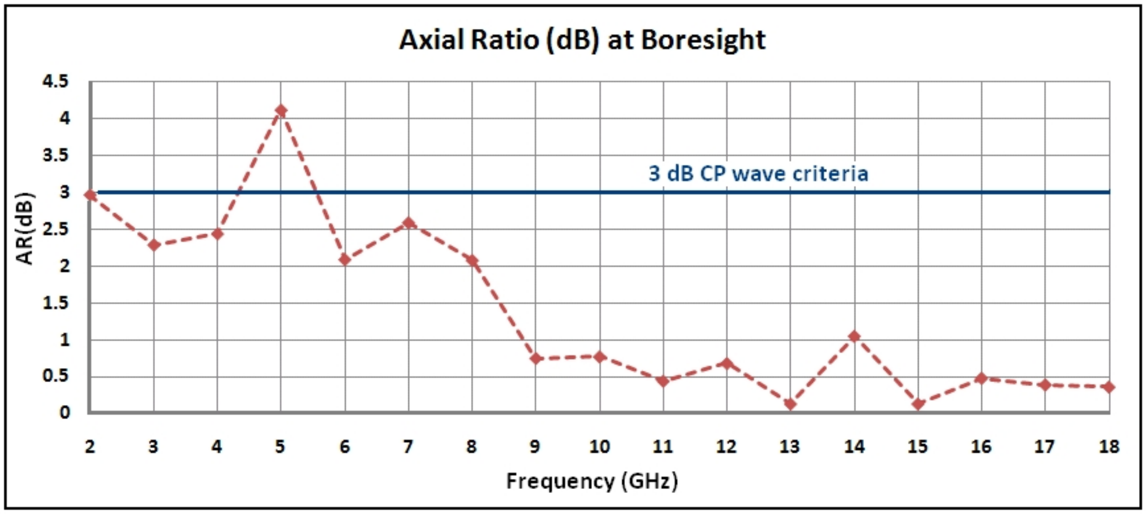

Figure 6-45: Axial Ratio (dB) vs. Frequency (GHz)

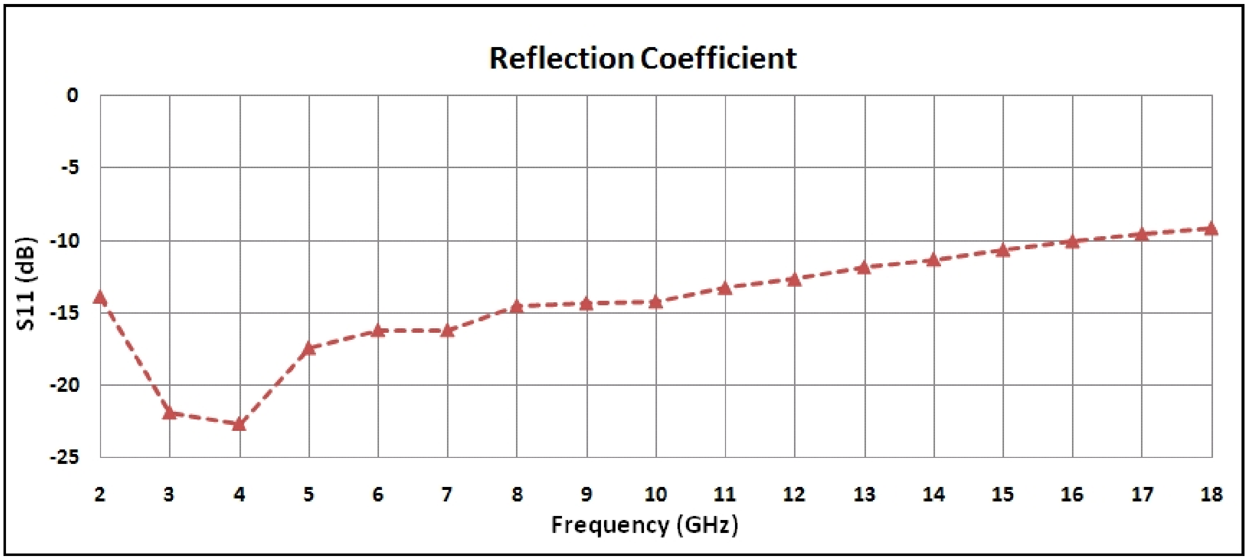

Figure 6-46: S11 (dB) vs. Frequency (GHz

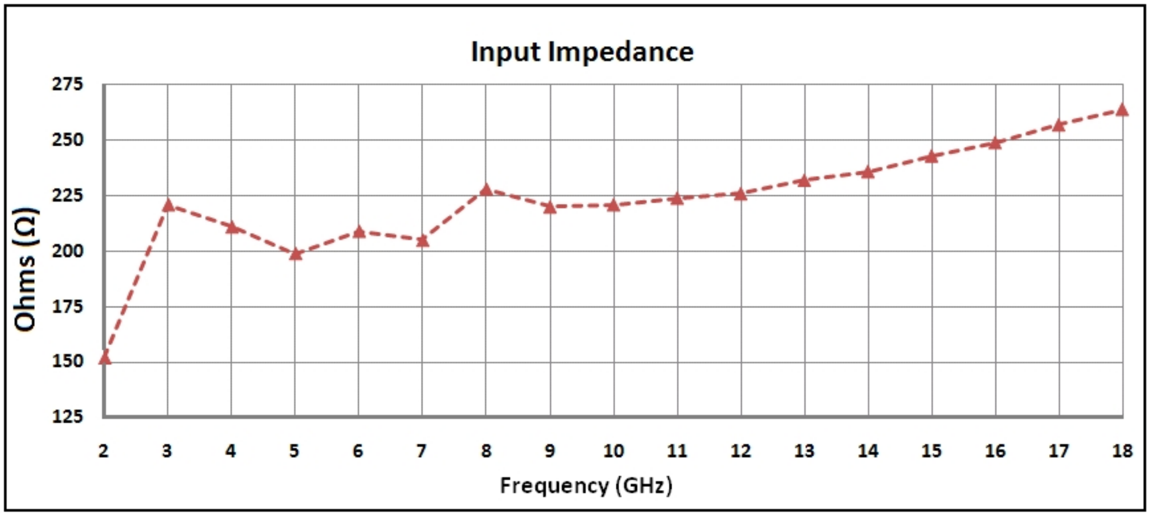

Figure 6-47: Input Impedance vs. Frequency (GHz)

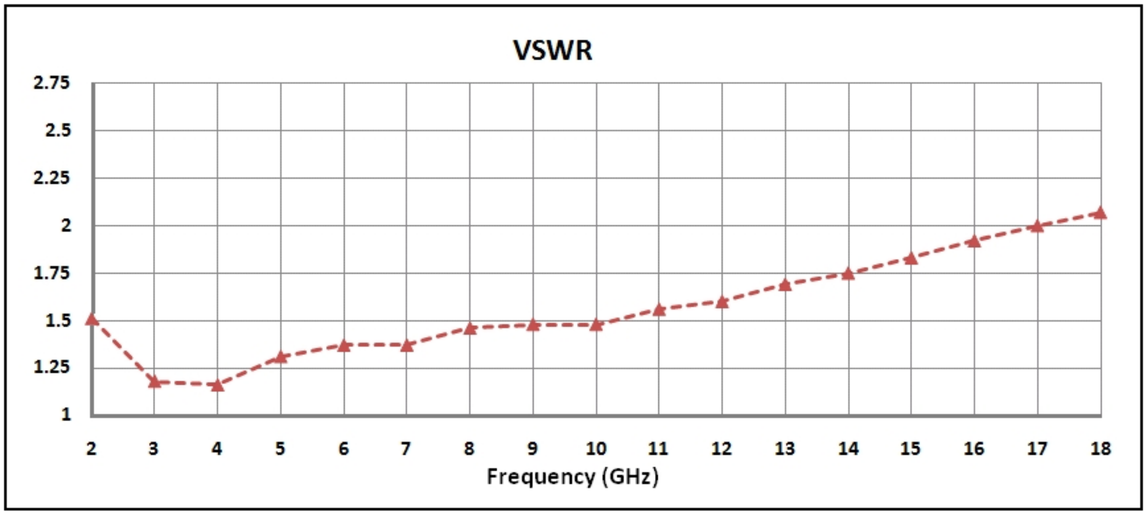

Figure 6-48: VSWR vs. Frequency (GHz)

Table 6.12: BORESIGHT RHC AND LHC GAIN, AXIAL RATIO, S11, VSWR, AND INPUT IMPEDANCE COMPARISON OF A CIRCULAR AND POLYGONAL SPIRAL ANTENNA WITH GRADUALLY TRANSITIONING ARMS AT LOW FREQUENCIES

f(GHz)	Gain (dB)				AR(dB)		S11(dB)		VSWR		Input Ω	
	RHC		LHC									
	Circ.	Poly.	Circ.	Poly.	Circ.	Poly.	Circ.	Poly.	Circ.	Poly.	Circ.	Poly.
2	-2.220	-1.49	-7.26	-16.9	11.00	2.97	-6.73	-13.87	2.71	1.51	70.3	152
2.1	-0.867	-1.47	-9.35	-16.6	6.88	3.09	-10.8	-15.48	1.81	1.40	109	139
2.2	-0.261	-1.08	-12.0	-16.5	4.61	2.98	-13.5	-16.72	1.53	1.34	125	194
2.3	0.001	-0.68	-14.1	-16.3	3.48	2.90	-14.5	-30.11	1.46	1.06	129	200
2.4	0.109	-0.76	-14.9	-16.3	3.11	2.94	-15.1	-16.56	1.43	1.35	132	142
2.5	0.152	-0.84	-14.9	-16.6	3.11	2.87	-15.0	-11.39	1.43	1.74	132	188
2.6	0.277	-0.42	-14.4	-17.2	3.25	2.54	-13.9	-10.80	1.50	1.81	126	310
2.7	0.571	-0.12	-13.6	-17.1	3.46	2.48	-12.8	-13.63	1.60	1.53	118	269
2.8	0.843	0.15	-13.0	-17.1	3.59	2.39	-12.4	-21.82	1.63	1.41	115	183
2.9	0.985	0.65	-12.8	-17.5	3.61	2.16	-12.7	-27.11	1.60	1.09	118	194
3.0	1.220	0.83	-12.7	-16.8	3.56	2.29	-14.1	-21.85	1.49	1.18	127	221
3.1	1.680	1.02	-11.8	-16.6	3.73	2.30	-15.7	-26.17	1.39	1.10	135	184
3.2	1.99	1.41	-11.0	-17.5	3.98	1.97	-15.8	-24.68	1.39	1.12	136	169
3.3	2.04	1.48	-10.8	-17.7	4.01	1.91	-14.0	-18.35	1.50	1.27	128	171
3.4	2.27	1.69	-10.8	-16.4	3.91	2.17	-12.5	-17.11	1.62	1.32	117	203
3.5	2.64	2.14	-10.0	-15.7	4.12	2.25	-12.0	-18.70	1.67	1.26	113	207
3.6	2.82	2.20	-9.48	-16.0	4.30	2.14	-12.5	-18.61	1.63	1.26	116	217
3.7	3.12	2.58	-9.50	-16.1	4.14	2.02	-14.3	-19.87	1.48	1.22	130	213
3.8	3.56	2.68	-8.93	-17.0	4.20	1.81	-15.4	-19.65	1.41	1.23	135	209
3.9	3.72	2.90	-8.33	-15.0	4.43	2.23	-15.1	-18.49	1.42	1.27	132	230
4.0	3.79	3.21	-8.56	-13.9	4.27	2.44	-13.0	-22.63	1.58	1.16	119	211
4.1	3.75	3.39	-8.26	-12.7	4.27	2.75	-11.7	-20.29	1.74	1.21	109	218
4.2	3.94	3.65	-8.41	-12.4	4.24	2.75	-14.1	-23.78	1.70	1.14	111	212
4.3	4.43	3.71	-7.97	-12.7	4.44	2.65	-15.6	-25.51	1.49	1.11	127	207
4.4	4.62	3.98	-7.41	-13.4	4.29	2.37	-12.9	-22.20	1.40	1.17	135	186
4.5	4.62	4.15	-7.70	-12.8	4.21	2.50	-11.2	-19.53	1.59	1.24	122	203
4.6	4.81	4.18	-7.67	-15.6	4.37	1.78	-11.4	-20.39	1.76	1.21	108	196
4.7	4.94	4.22	-7.23	-23.3	4.22	0.74	-13.4	-21.98	1.74	1.17	108	199
4.8	5.14	4.25	-7.32	-11.3	4.13	2.92	-15.1	-16.33	1.54	1.36	123	208
4.9	5.48	4.25	-7.17	-7.8	4.24	4.34	-13.4	-21.57	1.42	1.18	132	213
5.0	5.47	4.28	-6.94	-8.4	4.05	4.12	-11.4	-17.40	1.54	1.31	125	199
5.1	5.02	4.64	-7.70	-11.4	4.09	2.76	-8.94	-19.24	2.11	1.25	93	216
5.2	5.27	4.61	-7.67	-11.4	4.05	2.76	-7.93	-17.11	2.34	1.32	94	215
5.3	5.24	4.75	-7.57	-10.3	3.73	3.10	-7.93	-18.87	2.36	1.26	98	226
5.4	5.66	4.79	-8.25	-9.96	3.51	3.22	-9.24	-24.46	2.04	1.13	110	196
5.5	5.99	4.84	-8.35	-9.27	3.37	3.47	-12.0	-18.12	1.67	1.28	134	199
5.6	6.11	4.81	-8.35	-8.22	2.82	3.94	-14.74	-19.20	1.45	1.25	157	210
5.7	6.35	4.97	-9.75	-10.3	2.31	3.03	-16.96	-18.70	1.33	1.26	172	216
5.8	6.38	5.17	-11.37	-12.0	1.37	2.43	-19.83	-23.29	1.22	1.15	176	193
5.9	6.48	5.24	-15.76	-12.8	1.03	2.19	-23.88	-17.47	1.14	1.31	173	188
6.0	6.55	5.26	-18.02	-13.2	1.04	2.09	-24.61	-16.17	1.13	1.37	167	209

6.5 Antenna Fabrication and Measurements

The antennas were fabricated on Rogers Type RT5880 Duroid substrate that is 20 mils thick. The substrate is copper-clad on both sides, therefore the copper was etched off the back side. This substrate was chosen because it provides the closest permittivity match ($\epsilon_r = 2.20$) to air from 2-18 GHz. A 60 mil-diameter spacing (1.524 mm) was used at the feedpoints at the center of the antenna structure. The antennas were fed in unbalanced co-axial mode from the back of the cavity. A wideband balun was used that transformed the unbalanced coaxial mode into balanced two-wire transmission line mode that feeds the spiral antenna. The balun also allows for impedance transformation from the 50Ω impedance of the coaxial line to the impedance of the spiral antenna. The cavity depth is 0.625 inch including the air-gap between the radiator and the absorbing layers.

6.5.1 Gain

The fabricated polygonal antennas were tested in an anechoic chamber for their V-pol and H-pol gain components from 2-18 GHz. The measured antenna gains and simulation results at 4 GHz intervals are shown in Figures 6-49, 6-50, 6-51, 6-52, 6-53, 6-54, 6-55 and 6-56. Measurements for principle planes $\Phi = 0°$, $\Phi = 90°$ and a diagonal cut $\Phi = 45°$ are presented here. The figures indicate that the measured gains are well-consistent with those of the simulated gains.

6.5.2 Axial Ratio

The measured axial ratios at boresight for all four configurations of the polygonal antenna are shown in Figures 6-57, 6-58, 6-59 and 6-60.

6.5.3 Discussion

As discussed previously, a spiral antenna radiates from a region of the antenna where the circumference equals one wavelength. For a square spiral operating from 2-18

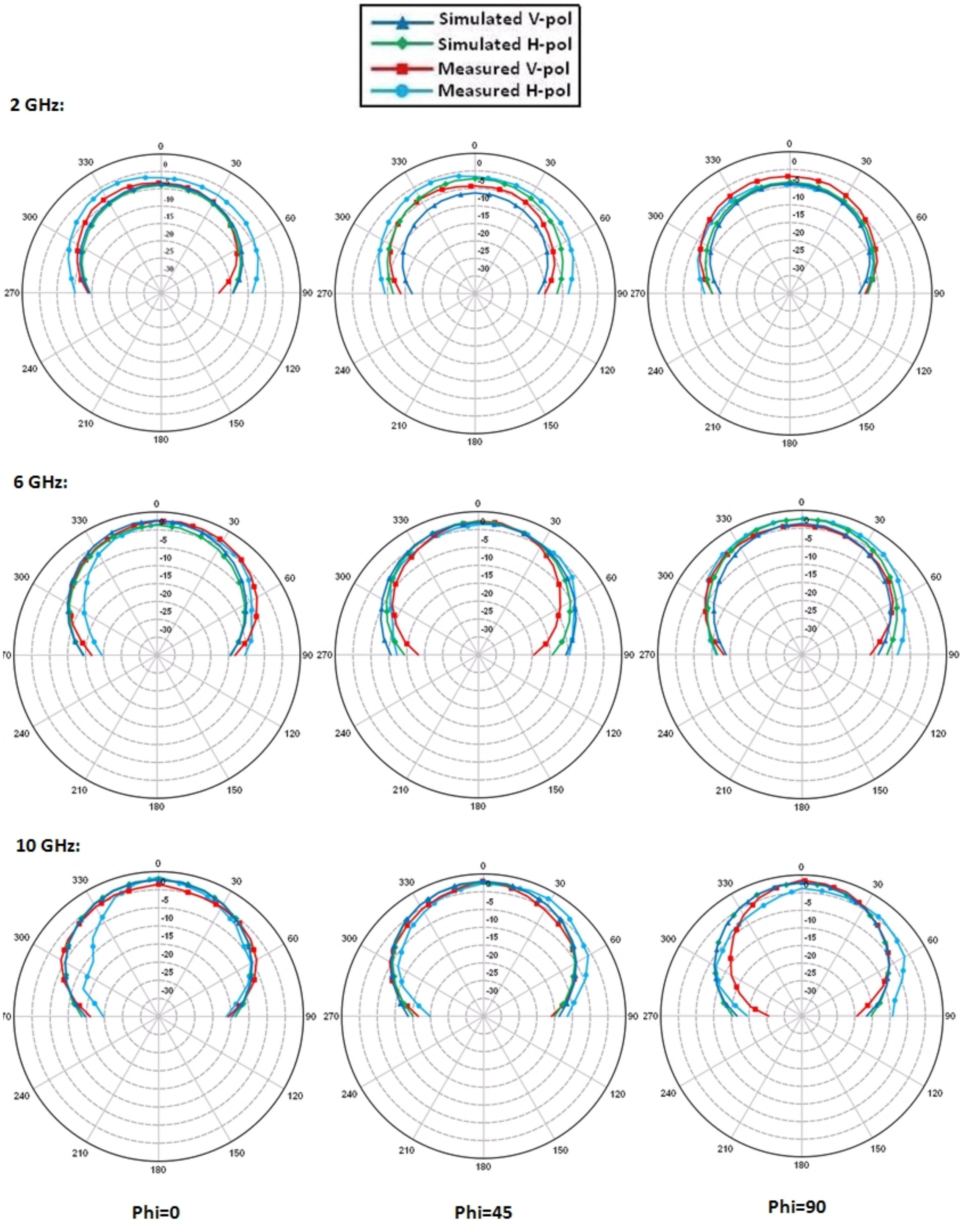

Figure 6-49: Measured vs. simulated V-pol and H-pol gains for original polygonal spiral antenna at 2, 6 and 10 GHz

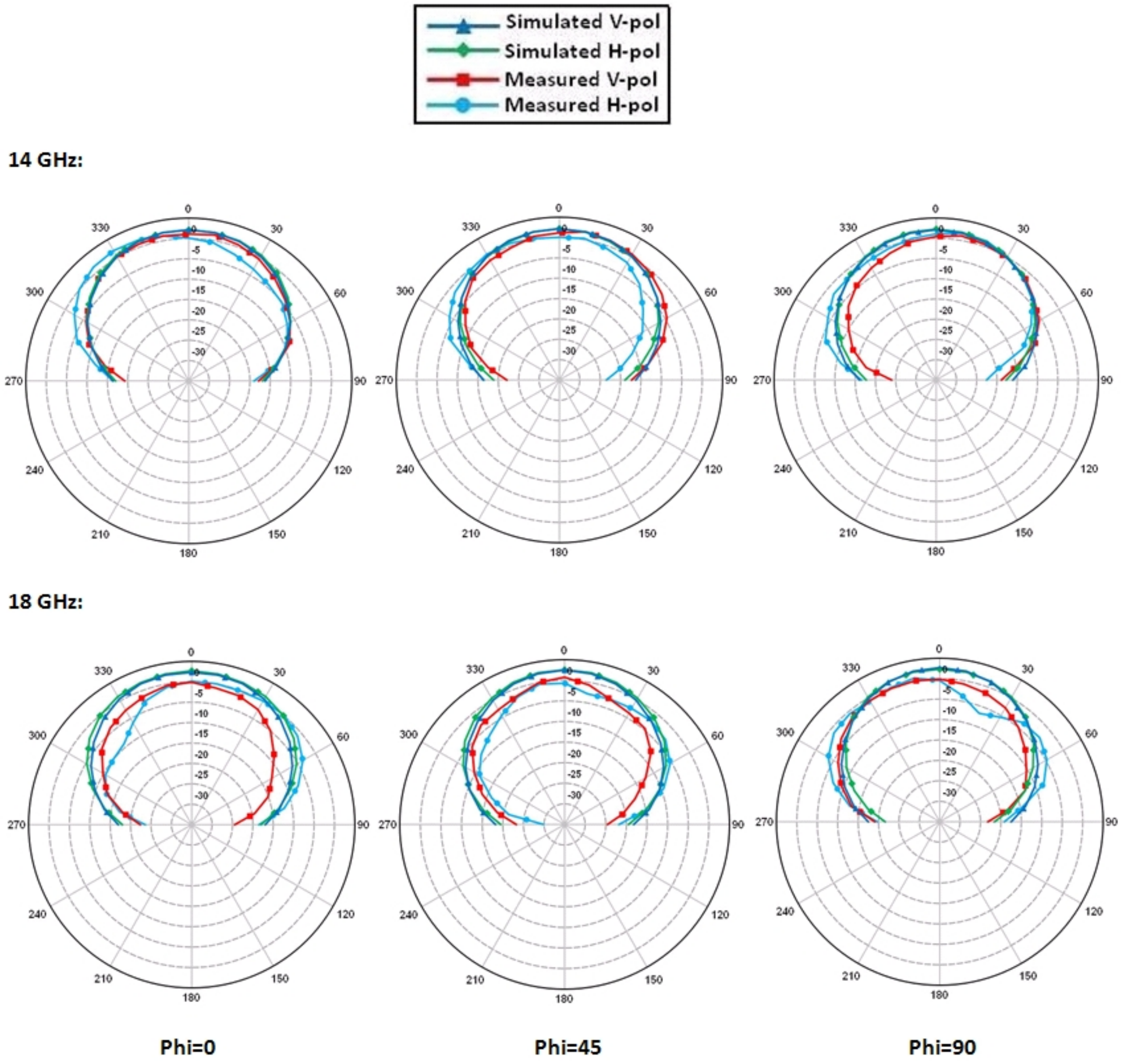

Figure 6-50: Measured vs. simulated V-pol and H-pol gains for original polygonal spiral antenna at 14 and 18 GHz

GHz, the outer circumference of the spiral needs to be at least 150 mm (wavelength at 2 GHz). For our polygonal models, the outer circumference corresponds to approximately 203 mm. The extra length was left to allow for residual currents to diminish sufficiently in magnitude before reaching the arm ends.

The fabricated antenna patterns demonstrate that the simulation patterns obtained from theoretical design translate considerably well to practice. A modified Archimedean polygonal spiral antenna spiral antenna demonstrates excellent axial

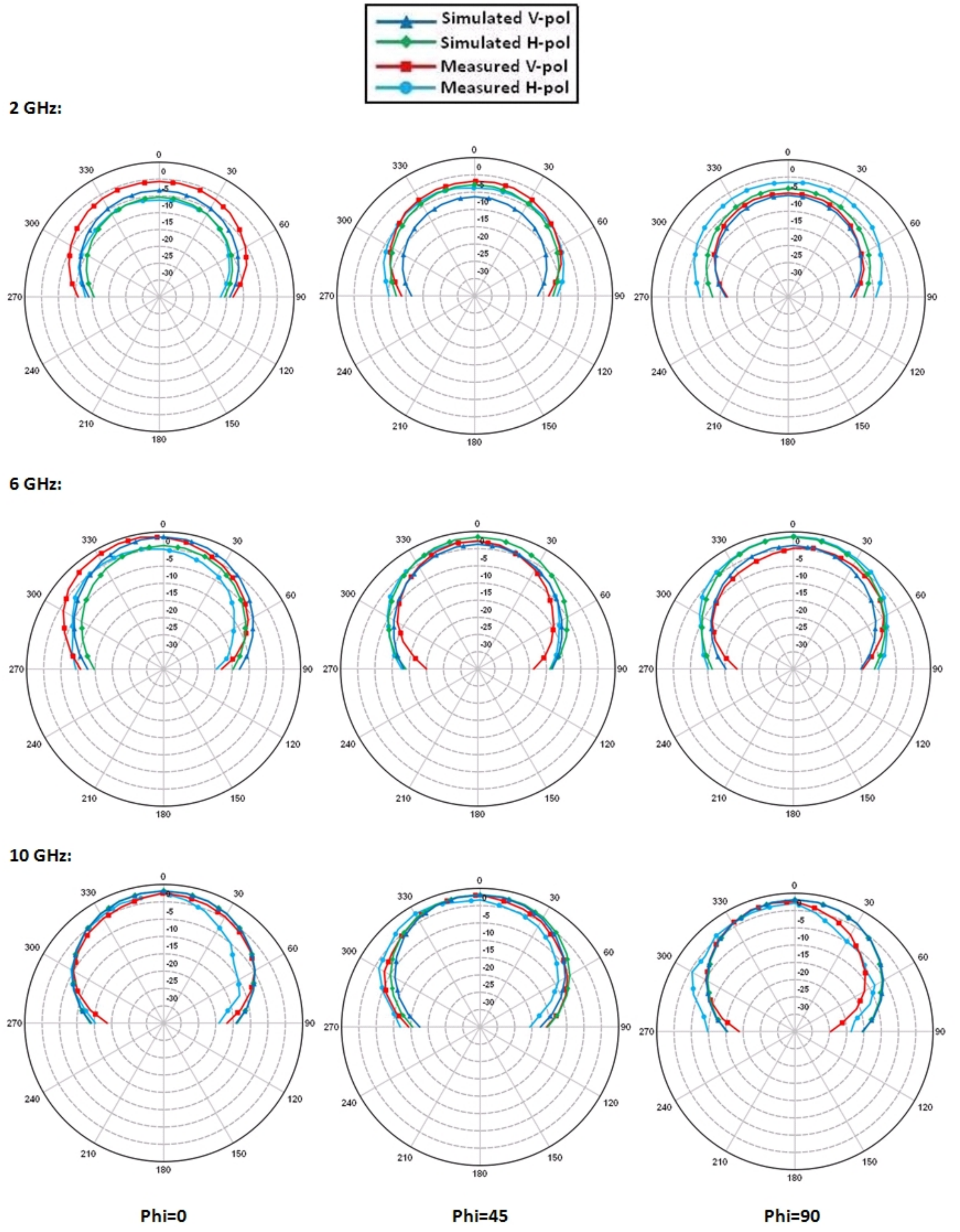

Figure 6-51: Measured vs. simulated V-pol and H-pol gains at 2, 6 and 10 GHz for polygonal spiral antenna with 12th interpolated turn

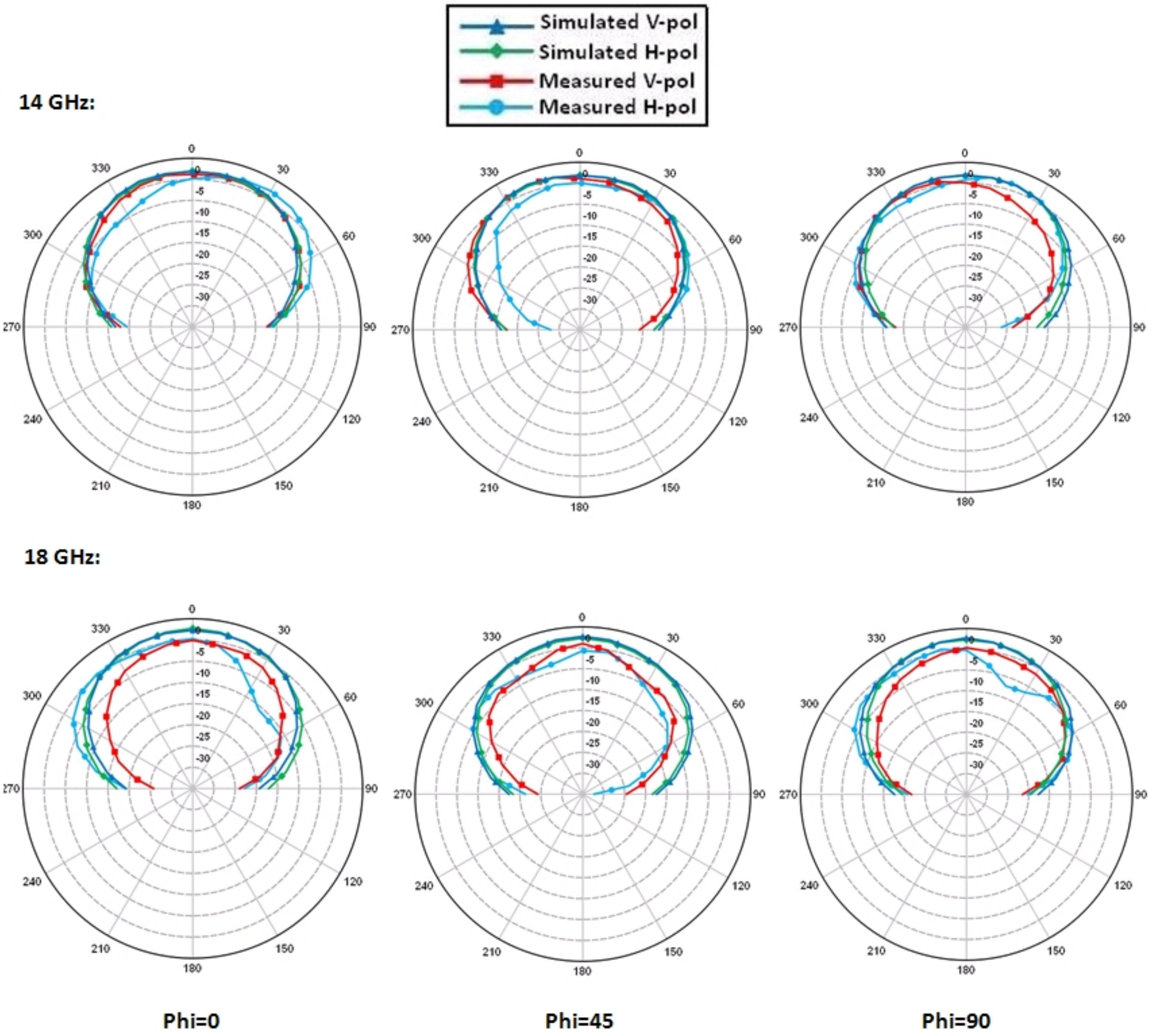

Figure 6-52: Measured vs. simulated V-pol and H-pol gains at 14 and 18 GHz for polygonal spiral antenna with 12th interpolated turn

ratio performance across the bandwidth compared to its square counterpart. The axial ratio in the original polyognal antenna and the antenna with gradually transitioning arms has been minimized to $\leq 3dB$ for almost 98% of the operational bandwidth. For circularly polarized applications in which antenna aperture size and a square footprint are important factors, these wideband antennas can prove to be extremely useful.

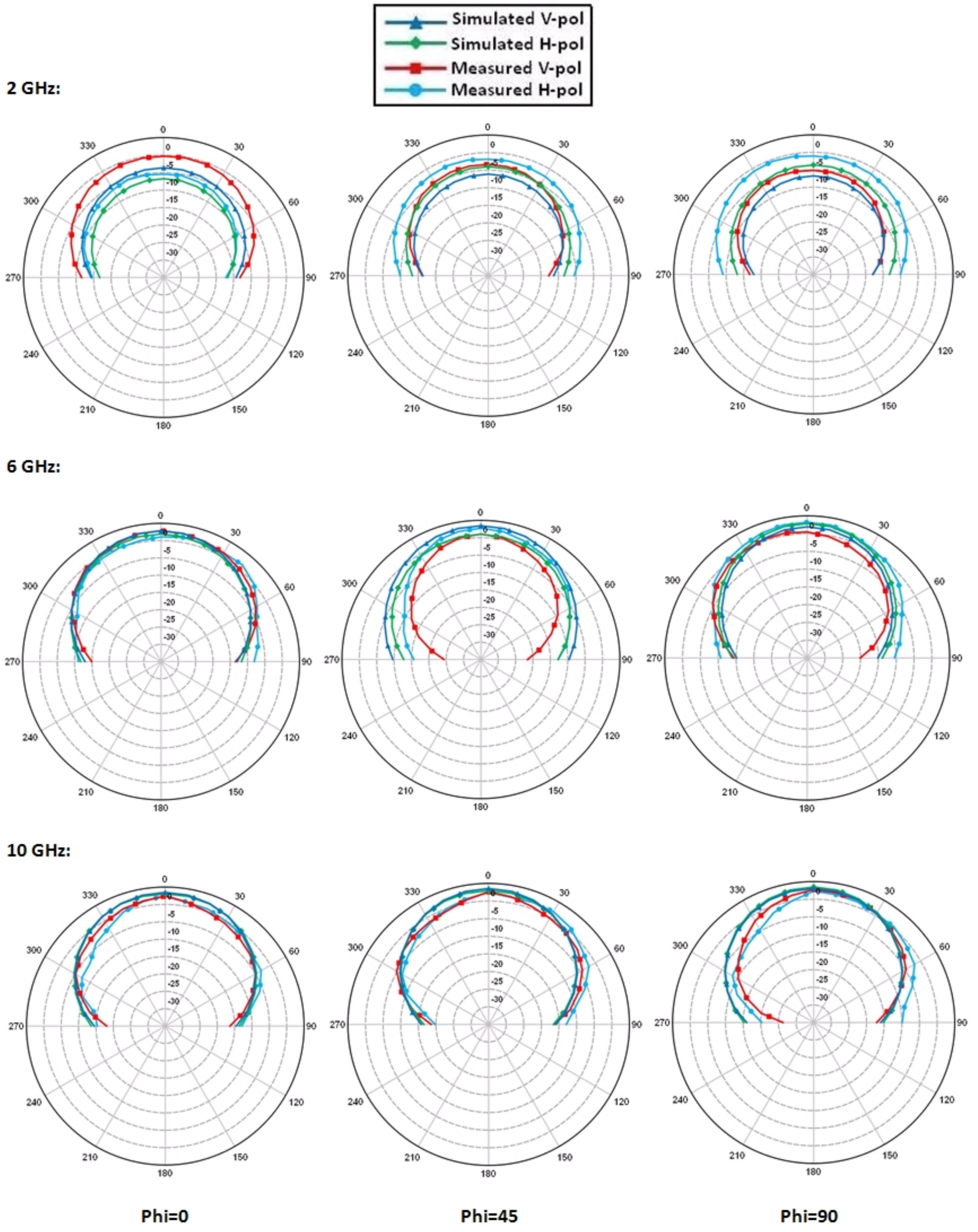

Figure 6-53: Measured vs. simulated V-pol and H-pol gains at 2, 6 and 10 GHz for polygonal spiral antenna with last interpolated turn

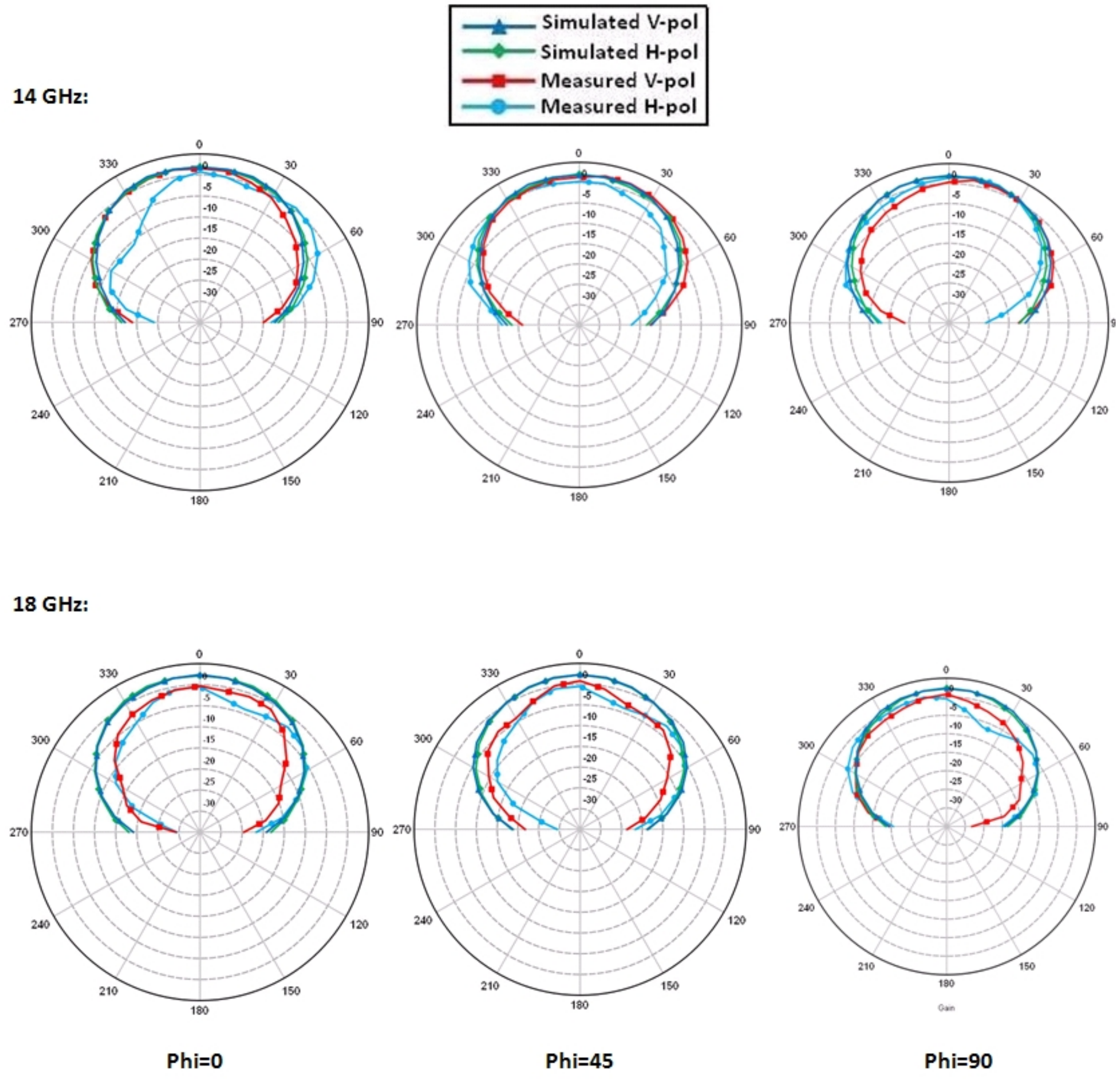

Figure 6-54: Measured vs. simulated V-pol and H-pol gains at 14 and 18 GHz for polygonal spiral antenna with last interpolated turn

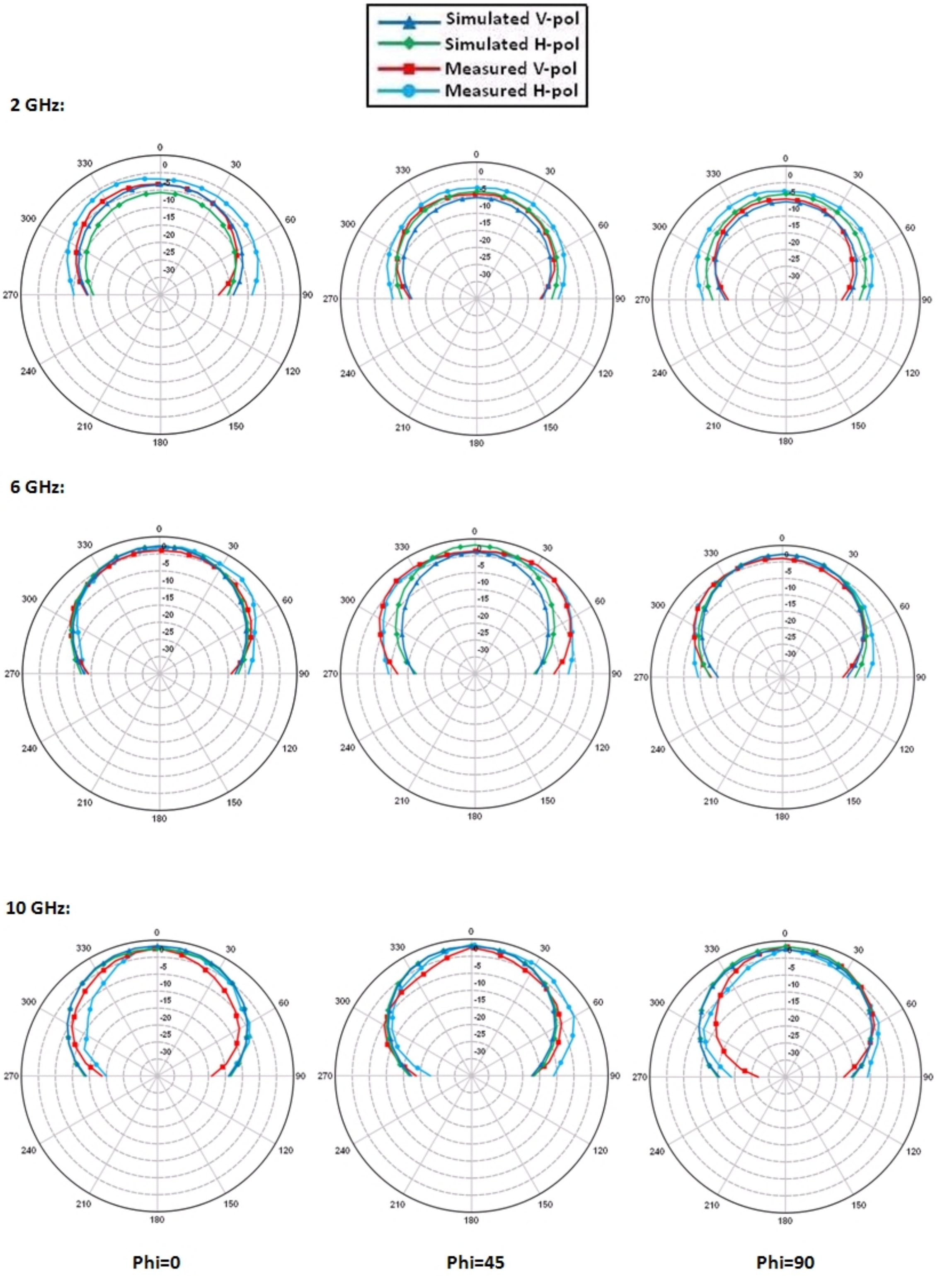

Figure 6-55: Measured vs. simulated V-pol and H-pol gains at 2, 6 and 10 GHz for polygonal spiral antenna with gradually transitioning arms

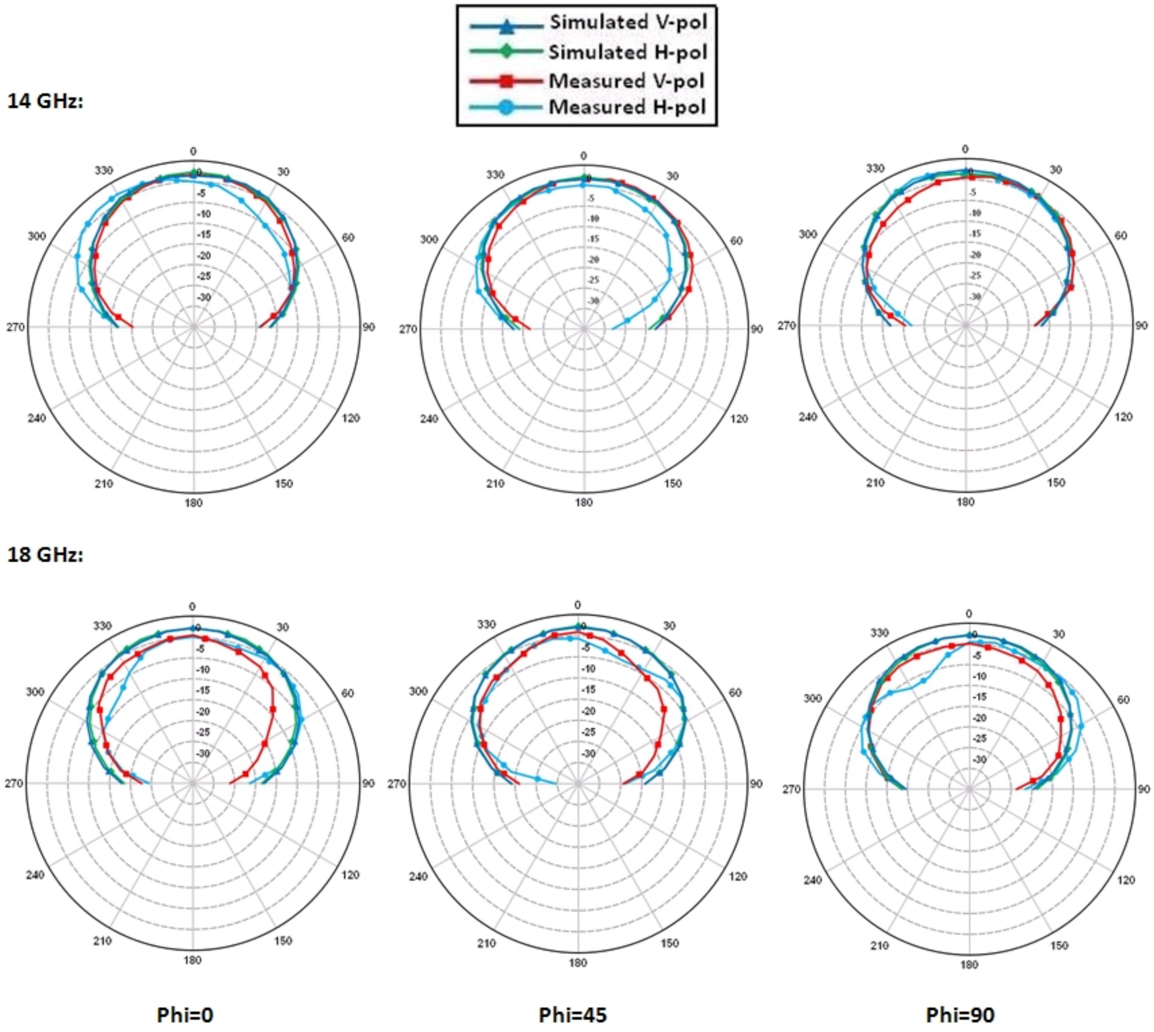

Figure 6-56: Measured vs. simulated V-pol and H-pol gains at 14 and 18 GHz for polygonal spiral antenna with gradually transitioning arms

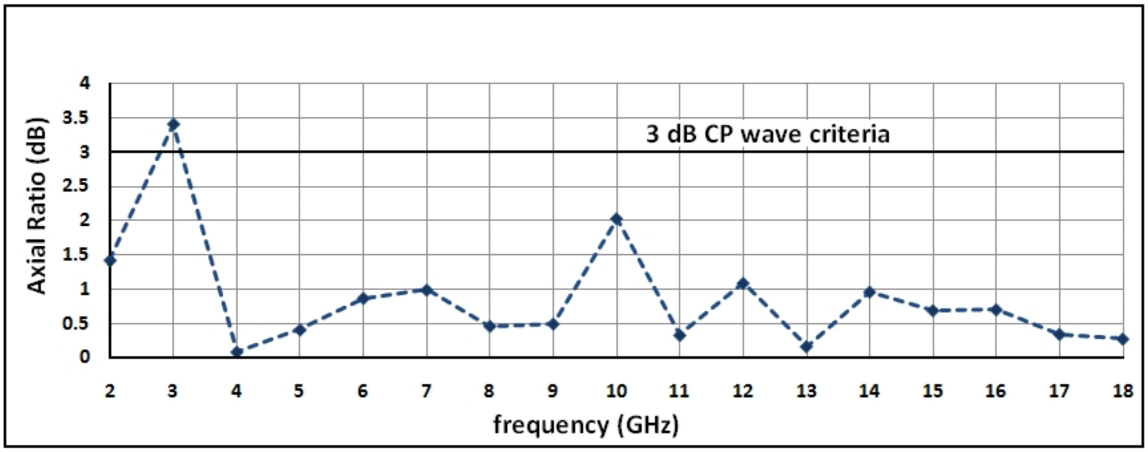

Figure 6-57: Measured axial ratio for original polygonal spiral antenna

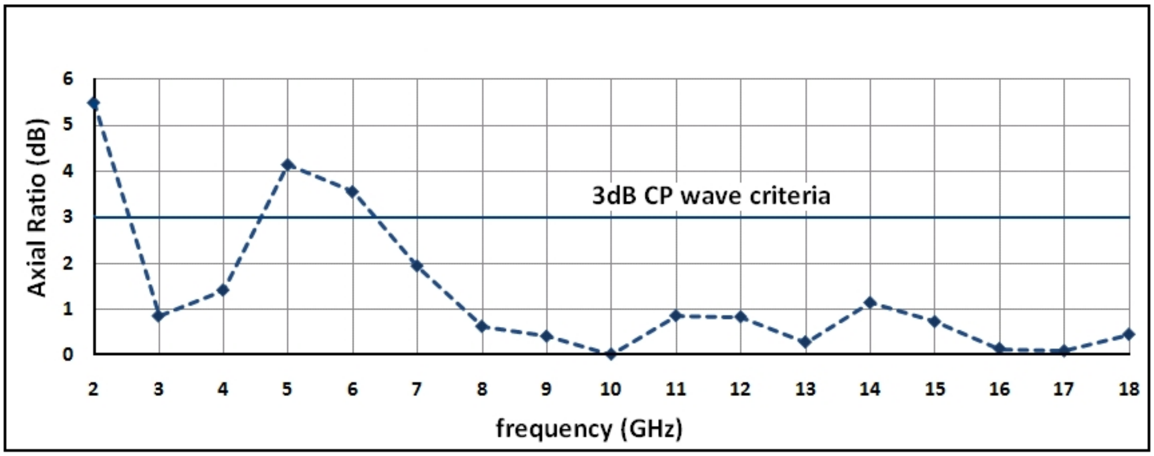

Figure 6-58: Measured axial ratio for polygonal spiral antenna with 12th interpolated turns

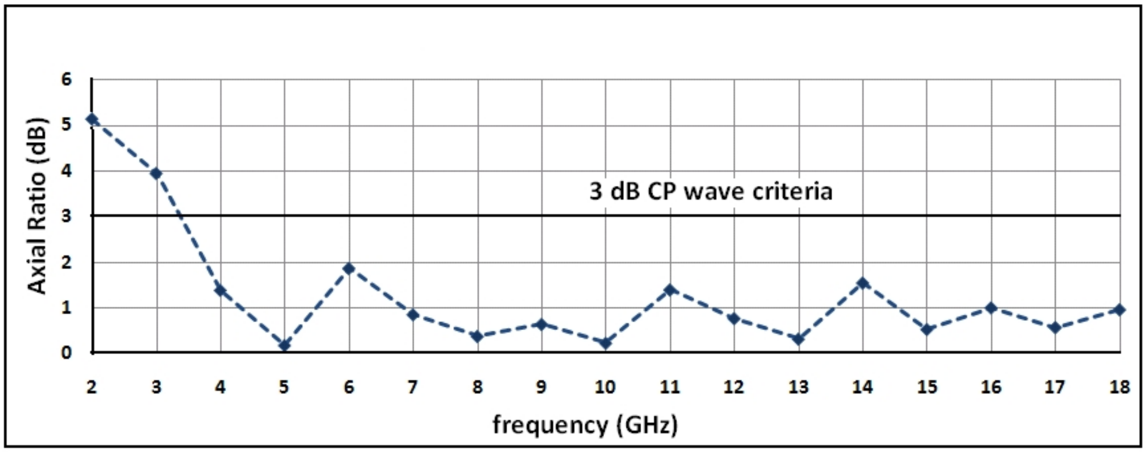

Figure 6-59: Measured axial ratio for polygonal spiral antenna with interpolated last turns

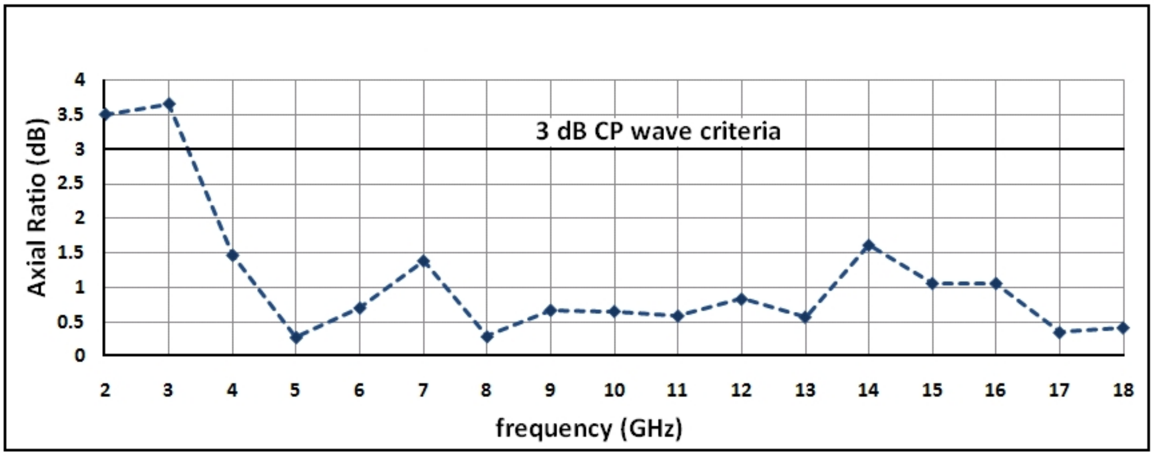

Figure 6-60: Measured axial ratio for polygonal spiral antenna with gradually transitioning arms

Chapter 7

Conlusion

In this dissertation, we have discussed methods for developing low-profile absorptive cavity backed spiral antennas and investigated the radiation characteristics of several low-profile models. A procedure for developing and optimizing hybrid, shallow cavities with dielectric and magnetic materials has been presented. Using the shallow cavity configuration, we have investigated the radiation characteristics of a 2-18 GHz cavity-backed slow-wave zigzag Archimedean spiral antenna. We developed cavity-backed elliptical spiral antennas with capability to control the beam-width in two orthogonal planes of radiation. We also presented studies of rectangular spiral antennas that highlight the problem of high axial ratios associated with square spirals. Finally, we have presented 2-18 GHz polygonal modified Archimedean spiral antennas that approximate a circular Archimedean spiral in their high frequency operating regions and a square spiral in their low-frequency zone. The designs have maintained a $\leq 3dB$ axial ratio for 93.75%-98% of their bandwidths while preserving the advantages of a square spiral antenna. The radiation patterns obtained from the proposed polygonal geometry are compared to that obtained from purely circular and square patterns having the same diameter and a significant improvement in axial ratio is demonstrated in the results. A shallow cavity-backed modified Archimedean spiral antenna developed in this work can prove to be extremely useful for applications where the purity of circularly polarized waves, ultra-wide bandwidths and low-profile geometries for closer array packing are important design criteria.

7.1 Future Work

7.1.1 Cavities with EBG materials

The drawback of using broadband absorbing materials in spiral cavities is that more than 50% of power delivered to the antenna is absorbed, or in other words, lost. However, abosorbers are used instead of an empty cavity or a ground plane, because the antenna response becomes narrowband in the latter case. To address the problem of power loss associated with lossy cavities, electromagnetic bandgap (EBG) materials can be used in the cavity. EBG structures are artificial periodic (sometimes non-periodic) objects which prevent or assist the propagation of waves in a specified band of frequency for all incident angles and all polarization states. 2D EBG surfaces have the advantages of low-profile, lightweight and low fabrication cost, and are widely considered in antenna engineering [49]. The material characterization process we have used is equally precise for non-resonant as well as resonant structures, and EBG materials or metamaterials for antenna engineering can be precisely characterized using the methodology described earlier in this work. When a plane wave illuminates an electromagnetic bandgap structure, the reflection phase varies with frequency. At a certain frequency, the reflection phase is zero degrees, which resembles a perfect magnetic conductor that does not exist in nature [49]. If a spiral antenna is placed horizontally over a traditional perfect electric conductor (PEC), due to reverse image current, the reflection from the ground plane changes orientation of radiation. In contrast, when an EBG ground plane is used, and a circularly polarized wave is incident on the plane, the reflection phase changes from 180° to -180° as the frequency changes. Therefore, the reflected wave can be made such that a right hand circularly polarized wave remains right hand circular and a left hand circularly polarized wave remains left hand circular. The reflected wave then reinforces the transmitted wave and power loss is minimized since the reflected wave is being transmitted and not absorbed [49]. EBG surfaces are capable of providing a constructive image current within a certain frequency band, which may limit the operational bandwidth of the antenna. In future, EBG substrates can be designed for wideband, efficient, low-profile wire antennas, especially spiral antennas. The surfaces will also have to be optimized to realize better performance for wideband and multiband designs.

7.1.2 Spiral Antenna Arrays

Polygonal antenna models developed in this work can be further investigated to use in novel configurations of wideband, electronically scanned arrays of broadband antenna elements. The most attractive feature of antenna arrays is their ability to rapidly steer the main beam towards any direction electronically without having to rotate the antenna platform. For decades, phased array technology has been widely used in defense aircrafts for target detection and combat operations. There are, of course, many factors that have to be taken into account when designing for such systems. For instance, the directivity of the antenna is proportional to its aperture size, as evident from a general equation relating the directivity to the effective area of the antenna: Directivity $D = \left(\frac{4\pi A_e}{\lambda^2}\right)$,[$A_e$ is the effective aperture (receiving) area and λ is the operating wavelength]. Usually, a highly directive phased array antenna system with a steerable beam is constructed from a large number of narrowband elements. Hence it remains a matter of further investigation as to whether it is possible to integrate wideband elements into a directive array configuration and whether fewer elements can be used to develop compact beam steering systems. Proper spacing of the antenna elements is another important issue. For instance, if we want to steer the beam all the way to endfire, the elements have to be placed at least $\left(\frac{\lambda}{2}\right)$ distance apart. When the elements are not appropriately spaced, undesired radiation, also known as grating lobes, appear in the antenna pattern and signal direction cannot be accurately resolved in their presence [14, 22]. The frequency bandwidth is also associated with major design issues. The bandwidth of a steerable phased array is limited by the bandwidth of individual elements, element spacing, steering angle of the main beam and the array size, whichever sets the lowest limit on the range of operable frequencies. In future, wideband spiral antenna arrays over EBG substrates can be investigated as well. However, wire-EBG antennas have relatively strong mutual coupling and this issue needs to be thoroughly investigated in order to arrive at solutions which circumvent this problem and extend the bandwidth of operation.

Metamaterials in Spiral Elements of Different Sizes

Metamaterials are engineered materials that enable us to extend our control over matter in seemingly extraordinary ways. Basically, when materials are arranged in certain periodic configurations in a given volume, the effective overall permittivity or permeability of the entire bulk can be engineered to become positive, negative, double positive or double negative. Solely depending on the shape and physical design, the structure can be artificially made to become resonant or provide certain electromagnetic properties in any desired frequency as long as the overall shape remains less than one wavelength. It is possible to develop compact phased arrays of wideband elements with the aid of meta-materialized structures. Polygonal antenna elements of different number of sides or different sized spiral antennas can also be used in an array configuration where smaller spirals are interleaved between larger spirals.

Appendix A

Code for Generating Polygonal Spiral Curves in C

A.1 Function for Drawing Closed-loop Polygons and Determining the Relationship Between the Angles

```
//maximum sides of polygons
#define MAXSIDES 32
// how many turns at each number of sides
#define TURNSPER 4
// how many steps (32, 16, 8, 4) ⟹ 4 steps
#define NUMSTEPS 4
#define PI 3.14159
// numsides – how many sides
// ratio of 1.0 means a regular n-gon, 0.0 makes regular n/2-gon
// buffer is where to put results, r1,theta1,r2,theta2....
void make_poly(int numSides,double ratio,double *buffer){
double shortAngle;
```

```
double longAngle;
int i;
double r;
double theta;

    shortAngle = ratio * 2 * PI/((double)numSides);
longAngle = (2 * PI - (numSides/2) * shortAngle)/((double)numSides/2);
r = 1.0/cos(longAngle/2.0);
theta = longAngle/2.0;

    for(i = 0;i < numSides;i++){
buffer[2 * i] = r;
buffer[2 * i +1] = theta;
if(i %2 == 0){
theta += shortAngle;
}
else{
theta += longAngle;
}
}

return;
}
```

A.2 Main Program for Original Polygonal Spiral Curve

```
int main(int argc, char **argv){
int i;
double ratio;
int j;
double buffer[2*MAXSIDES];
int sides = MAXSIDES;
int k;
double r;
double theta;
double angleSoFar; // 2 * pi * (number of turns completed)
double radiusPerRadian = 2.0/(NUMSTEPS * TURNSPER * 2 * PI);
double x, y;
for(i = 0; i < NUMSTEPS; i++){
for(j =0; j < TURNSPER; j++){
make_poly(sides, 1.0, buffer);
}
//at this point, buffer contains polar coords for vertices of a sides-gon of width 1.
//Need to scale it to the proper width for the spiral, then
//convert to cartesian coords
for(k = 0; k < sides; k++){
// unpack coordinates from the buffer
r = buffer[2 * k];
theta = buffer[2 * k+1];
r *= radiusPerRadian*(angleSoFar + theta);
x = r * cos(theta);
y = r * sin(theta);
```

```
printf("%f %f \n", x, y);
}
angleSoFar += 2 * PI;
}
sides /=2;
}
return 0;
}
```

A.3 Main Program for Polygonal Spiral Curve with 12th Interpolated Turn

```
int main(int argc, char **argv){
int i;
double ratio;
int j;
double buffer[2 * MAXSIDES];
int sides = MAXSIDES;
int k;
double r;
double theta;
double angleSoFar; // 2 * pi * (number of turns completed)
double radiusPerRadian = 2.0/(NUMSTEPS * TURNSPER * 2 * PI);
double x, y;
int flag = 0;
for(i = 0; i < NUMSTEPS; i++){
for(j =0; j < TURNSPER; j++){
if((sides == 4) && (j == 0)){
```

```
sides = 8;
flag = 1;
make_poly(sides, 0.5, buffer);
}
else{
make_poly(sides, 1.0, buffer);
}
//at this point, buffer contains polar coords for
// vertices of a sides-gon of width 1. Need to scale it
// to the proper width for the spiral, then convert to
// cartesian coords
for(k = 0; k < sides; k++){
// unpack coordinates from the buffer
r = buffer[2 * k];
theta = buffer[2 * k+1];
r *= radiusPerRadian * (angleSoFar + theta);
x = r * cos(theta);
y = r * sin(theta);
printf(”%f %f \n”, x, y);
}
if(flag){
sides = 4;
}
angleSoFar += 2 * PI;
}
sides /=2;
}
return 0;
}
```

A.4 Main Program for Polygonal Spiral Curve with Last Interpolated Turns

```
int main(int argc, char **argv){
int i;
double ratio;
int j;
double buffer[2 * MAXSIDES];
int sides = MAXSIDES;
int k;
double r;
double theta;
double angleSoFar; // 2 * pi * (number of turns completed)
double radiusPerRadian = 2.0/(NUMSTEPS * TURNSPER * 2 * PI);
double x, y;
for(i = 0; i < NUMSTEPS; i++){
for(j =0; j < TURNSPER; j++){
if((sides > 4) && (j == (TURNSPER - 1))){
make_poly(sides, 0.5, buffer);
}
else{
make_poly(sides, 1.0, buffer);
}
//at this point, buffer contains polar coords for
// vertices of a sides-gon of width 1. Need to scale it
// to the proper width for the spiral, then convert to
// cartesian coords
for(k = 0; k < sides; k++){
// unpack coordinates from the buffer
```

```
r = buffer[2 * k];
theta = buffer[2 * k+1];
r *= radiusPerRadian*(angleSoFar + theta);
x = r * cos(theta);
y = r * sin(theta);
printf(”%f %f \n”, x, y);
}
angleSoFar += 2*PI;
}
sides /=2;
}
return 0;
}
```

A.5 Main Program for Polygonal Spiral Curve with Gradually Transitioning Arms

```
int main(int argc, char **argv){
int i;
double ratio;
int j;
double buffer[2 * MAXSIDES];
int sides = MAXSIDES;
int k;
double r;
double theta;
double angleSoFar; // 2 * pi *(number of turns completed)
double radiusPerRadian = 2.0/(NUMSTEPS * TURNSPER * 2 * PI);
```

```
double x, y;
for(i = 0; i < NUMSTEPS; i++){
for(j =0; j < TURNSPER; j++){
if(sides > 4){
make_poly(sides, ((double)(4-j))/4.0, buffer);
}
else{
make_poly(sides, 1.0, buffer);
}
//at this point, buffer contains polar coords for
// vertices of a sides-gon of width 1. Need to scale it
// to the proper width for the spiral, then convert to
// cartesian coords
for(k = 0; k < sides; k++){
// unpack coordinates from the buffer
r = buffer[2 * k];
theta = buffer[2 * k+1];
r *= radiusPerRadian*(angleSoFar + theta);
x = r * cos(theta);
y = r * sin(theta);
printf(”%f %f \n”, x, y);
}
angleSoFar += 2 * PI;
}
sides /=2;
}
return 0;
}
```

Bibliography

[1] M.N. Afsar, Yong Wang, and R. Cheung. Analysis and measurement of a broadband spiral antenna. *Antennas and Propagation Magazine, IEEE*, 46(1):59 – 64, feb 2004.

[2] Mohammed Afsar, Nahid Rahman, and Rudolph Cheung. Design, characterization, and optimization of ultrawideband cavity-backed spiral antennas at microwave frequencies. In *Radar Conference (EuRAD), 2011 European*, pages 261 –264, oct. 2011.

[3] N.N. Al-Moayed, M.N. Afsar, U.A. Khan, S. McCooey, and M. Obol. Nano ferrites microwave complex permeability and permittivity measurements by t/r technique in waveguide. *Magnetics, IEEE Transactions on*, 44(7):1768 –1772, july 2008.

[4] Antenna-Theory.com. `http://www.antenna-theory.com/definitions/axial.php`. [Online; accessed 30-December-2011].

[5] J. Baker-Jarvis, E.J. Vanzura, and W.A. Kissick. Improved technique for determining complex permittivity with the transmission/reflection method. *Microwave Theory and Techniques, IEEE Transactions on*, 38(8):1096 –1103, aug. 1990.

[6] C. A. Balanis. *Antenna Theory Analysis and Design.* Wiley-Interscience, third edition, April 2005.

[7] J.M. Bell and M.F. Iskander. A low-profile archimedean spiral antenna using an ebg ground plane. *Antennas and Wireless Propagation Letters, IEEE*, 3(1):223 –226, dec. 2004.

[8] A.-H. Boughriet, C. Legrand, and A. Chapoton. Noniterative stable transmission/reflection method for low-loss material complex permittivity determination. *Microwave Theory and Techniques, IEEE Transactions on*, 45(1):52 –57, jan 1997.

[9] B. H. Burdine. The spiral antenna. *Massachusetts Institute of Technology, Research Laboratory Technical Report*, apr 1955.

[10] T. P. Cencich and D. S. Filipovic. Spiral antennas. *Encyclopedia of RF and Microwave Engineering*, 2005.

[11] McGraw-Hill Companies. `http://www.mhprofessional.com/downloads/products/0071612882/0071612882_chap01.pdf`. [Online; accessed 12-January-2012].

[12] P. Markos C..M. Soukoulis D. R. Smith, S. Schultz. Determination of effective permittivity and permeability of metamaterials from reflection and transmission coefficients. *Phys. Rev*, B 65 (2002) 195104.

[13] FRC Group. Why Circular Polarized Antennas. `http://www.frccorp.com/pdf/Why%20Circular%20Polorized%20Antenna.pdf`. [Online; accessed 30-December-2011].

[14] R. L. Haupt. *Antenna Arrays A computational Approach.* Wiley, IEEE Press, 2010.

[15] H.Nakano. Helical and spiral antennas. *Encyclopedia of Telecommunications*, 2003.

[16] Chengdu AINFO Inc. Cavity Backed Spiral Antenna. `http://www.ainfoinc.com/en/p_ant_s_cavs.asp`. [Online; accessed 30-December-2011].

[17] R. H. Jin J. Lao and J. P. Geng. Uwb spiral antenna with parabolic reflector. In *XXIX URSI General Assembly*, 2008.

[18] J. Kaiser. The archimedean two-wire spiral antenna. *Antennas and Propagation, IRE Transactions on*, 8(3):312 –323, may 1960.

[19] B.A. Kramer, Ming Lee, Chi-Chih Chen, and J.L. Volakis. Design and performance of an ultrawide-band ceramic-loaded slot spiral. *Antennas and Propagation, IEEE Transactions on*, 53(7):2193 – 2199, july 2005.

[20] Randtron Antenna Systems L-3 Communications. Multi-octave Spiral Antennas. `http://www.l-3com.com/randtron/f15ant.htm`. [Online; accessed 30-December-2011].

[21] S. E. Lipsky. *Microwave Passive Direction Finding*, pages 39–47. SciTech Publishing, January 2004.

[22] R. J. Mailloux. *Electronically Scanned Arrays.* Morgan & Claypool Publishers, 2007.

[23] P. E. Mayes. *Spiral Antennas.* Wiley Encyclopedia of Electrical and Electronics Engineering, 1999.

[24] T. Milligan. *Modern Antenna Design*, pages 372–373. Wiley-IEEE Press, 1985.

[25] Jr. Musal, H.M. and D.C. Smith. Universal design chart for specular absorbers. *Magnetics, IEEE Transactions on*, 26(5):1462 –1464, sep 1990.

[26] Y. Mushiake. *Self-Complementary Antennas*, page 25. Springer-Verlag London Limited, 1996.

[27] H. Zhao N. Jing and Lihao Huang. A novel design of planar spiral antenna with metamaterial. In *PIERS Proceedings*, pages 725–728, mar 2010.

[28] H Nakano. *Helical and spiral antennas - a numerical approach.* Wiley and Sons, 1987.

[29] H. Nakano, R. Satake, and J. Yamauchi. Extremely low-profile, single-arm, wideband spiral antenna radiating a circularly polarized wave. *Antennas and Propagation, IEEE Transactions on*, 58(5):1511 –1520, may 2010.

[30] H. Nakano and J. Yamauchi. Characteristics of modified spiral and helical antennas. *Microwaves, Optics and Antennas, IEE Proceedings H*, 129(5):232 –237, october 1982.

[31] Antenna Magus Newsletter. `http://www.antennamagus.com/newsletter-1-4.php`. [Online; accessed 30-December-2011].

[32] A. M. Nicolson and G. F. Ross. Measurement of the intrinsic properties of materials by time-domain techniques. *Instrumentation and Measurement, IEEE Transactions on*, 19(4):377 –382, nov. 1970.

[33] M. Obol. Microwave technologies - determination of magnetic and dielectric materials microwave properties. `http://arxiv.org/abs/0906.2928`. [Online; accessed 30-December-2011].

[34] M. Obol, D. Tilton, and M.N. Afsar. The cauchy-riemann equations in determining the refractive index of microwave isolator of ferrite-metal strips in a waveguide. In *Microwave Conference, 2009. EuMC 2009. European*, pages 1156 –1158, 29 2009-oct. 1 2009.

[35] J. Wolfe R. Bawer. The spiral antenna. *IRE International Convention Record*, 8:84–95, mar 1960.

[36] N. Rahman, M. Obol, A. Sharma, and M. N. Afsar. Determination of negative permeability and permittivity of metal strip coated ferrite disks using the transmission and reflection technique. *Journal of Applied Physics*, 107(9):09A513 –09A513–3, may 2010.

[37] N. Rahman, Junhui Qiu, A. Sharma, Vu Anh Tran, M.N. Afsar, and R. Cheung. Beam-width control using a cavity-backed elliptical archimedean spiral antenna. In *Aerospace Conference, 2011 IEEE*, pages 1 –9, march 2011.

[38] Nahid Rahman, Anjali Sharma, Mohammed Afsar, Sandeep Palreddy, and Rudolf Cheung. Design and analysis of an optimized cavity-backed zigzag archimedean spiral antenna. In *Antennas and Propagation (EuCAP), 2010 Proceedings of the Fourth European Conference on*, pages 1 –4, april 2010.

[39] Nahid. Rahman, Anjali Sharma, Mohammed Afsar, Sandeep Palreddy, and Rudolph Cheung. Dielectric characterization and optimization of wide-band, cavity-backed spiral antennas. *Journal of Applied Computational Electromagnetics*, 26(2):09A513 –09A513–3, feb 2011.

[40] B. A. Sapna and H. R. Patnam. Slow wave-modified low profile planar spiral antenna on ebg. *Microwave and Optical Technology Letters*, 51(5), may 2009.

[41] U. Saynak and A. Kustepeli. Novel square spiral antennas for broadband applications. In *FREQUENZ*, volume 63, pages 14–19, jan-feb 2009.

[42] A. Sharma, N. Rahman, M. Obol, and M. Afsar. Precise characterization and design of composite absorbers for wideband microwave applications. In *Microwave Conference (EuMC), 2010 European*, pages 160 –163, sept. 2010.

[43] Anjali Sharma. Design of broadband microwave absorbers for application in wideband antennas. Master's thesis, Tufts University, 2009.

[44] W. L. Stutzman. *Polarization in electromagnetic systems.* Artech House, Inc.:Boston, 1993.

[45] J. Thaysen, K.B. Jakobsen, and H.-R. Lenler-Eriksen. Wideband cavity backed spiral antenna for stepped frequency ground penetrating radar. In *Antennas and Propagation Society International Symposium, 2005 IEEE*, volume 1B, pages 418 –421 vol. 1B, 2005.

[46] J.L. Volakis, M.W. Nurnberger, and D.S. Filipovic. Slot spiral antenna. *Antennas and Propagation Magazine, IEEE*, 43(6):15 –26, dec 2001.

[47] J.L. Wallace. Broadband magnetic microwave absorbers: fundamental limitations. *Magnetics, IEEE Transactions on*, 29(6):4209 –4214, nov 1993.

[48] W.B. Weir. Automatic measurement of complex dielectric constant and permeability at microwave frequencies. *Proceedings of the IEEE*, 62(1):33 – 36, jan. 1974.

[49] F. Yang and Y. Rahmat-Sami. *Electromagnetic Band Gap Structures in Antenna Engineering*. Cambridge University Press, 2009.